Order Number 9029950

Synthesis and analysis of Sm-Fe-Ti sputtered films with intrinsic coercive force greater than 30 KOe

Kamprath, Narayanan, Ph.D.

City University of New York, 1990

U·M·I
300 N. Zeeb Rd.
Ann Arbor, MI 48106

A

SYNTHESIS AND ANALYSIS OF Sm-Fe-Ti SPUTTERED FILMS WITH INTRINSIC COERCIVE FORCE GREATER THAN 30 KOe

by

NARAYANAN KAMPRATH

A dissertation submitted to the Graduate Faculty in Physics in partial fulfillment of the requirements for the degree of Doctor of Philosophy, The City University of New York.

1990

This manuscript has been read and accepted for the Graduate Faculty in Physics in satisfaction of the dissertation requirement for the degree of Doctor of Philosophy.

April 19, 1990
Date

Fred J. Cadieu
Chair of Examining Committee

April 19, 1990
Date

Executive Officer

Professor F. J. Cadieu

Professor C. R. Fischer

Professor V. Sahni

Dr. T. D. Cheung

Dr. M. A. Russak
Supervisory Committee

The City University of New York

ABSTRACT

SYNTHESIS AND ANALYSIS OF Sm-Fe-Ti SPUTTERED FILMS WITH INTRINSIC COERCIVE FORCE GREATER THAN 30 KOe

by

Narayanan Kamprath

Adviser: Professor Fred J. Cadieu

Rare-earth transition metal film magnets of several new phases in the Sm-Fe-Ti system have been prepared by special sputtering methods. Film samples have been directly crystallized onto heated substrates as well as first deposited amorphous and then subsequently crystallized. Magnetic fields have been applied during the sputter deposition and during the crystallization to induce in-the-film-plane anisotropies into the growing films. For the Sm-Fe-Ti system, a hard magnetic phase has been observed in subsequently crystallized amorphous deposits. As a function of composition, the high $_iH_c$ Sm-Fe-Ti phase has been shown to exhibit a maximum room temperature intrinsic coercivity of 38.5 KOe at a nominal composition of $Sm_{20}Fe_{70}Ti_{10}$. This high $_iH_c$ phase we report to be a $SmCo_5$ related hexagonal structure with a nominal formula of $Sm_7(Fe,Ti)_{30}$. For the high $_iH_c$ Sm-Fe-Ti films it has been possible to synthesize films that exhibit extreme in-the-film-plane anisotropy for fields of ±20 KOe. Fields of ±20 KOe applied in the film plane, but

perpendicular to the H_s direction were not sufficient to measurably magnetize the film in that direction. This corresponds to an effective energy of at least 10^7 erg/cm^3 for magnetizing the film in the film plane parallel versus perpendicular to the H_s direction. In addition the magnetic properties of the high $_iH_c$ Sm-Fe-Ti system containing small amounts of Al, V, and Zr have been studied. Films that have been directly crystallized onto heated substrates have exhibited several crystal phases such as 2-17, 1-5 as a function of composition and temperature. The Sm-Fe-Ti system also exhibited a soft magnetic phase of the $ThMn_{12}$-type at a nominal composition of $Sm(TiFe_{11})$. A systematic experimental research has been conducted by varying the sputtering parameters such as substrate temperature, sputtering gas pressure, deposition rate, and the distance between the target and the substrate. A model is also presented based upon the crystallite grain sizes and magnetic alignment energy that correlates the differences in the degree of in-the-film-plane anisotropy induced in these systems.

ACKNOWLEDGEMENTS

I am extremely grateful to my mentor, Professor Fred J. Cadieu, for his continuous support and encouragement throughout this work. I am thankful to former research associates Dr. T.D. Cheung, Dr. L. Wickramasekara, Dr. N.C. Liu, and Dr. X.R. Qian for several contributions in one way or another. Thanks are also extended to my fellow researchers H. Hegde and K. Chen.

I would also like to thank the members of my Supervisory Committee. It is my pleasure to extend my sincere thanks to all members of the Faculty and Staff, colleagues, and friends at the Department of Physics, Queens College.

I would also like to thank my parents and family, to whom this thesis is dedicated, for their continuous emotional support and encouragement during the many long years I was separated from them while conducting this research. The completion of this enormous task would not have been possible without their endless love and faith in me. I take this opportunity to thank my lovely wife Soumini for her continuous moral support and for bearing with me throughout the period of this research. I am thankful for my wonderful little son Sagar who makes me forget the strain and weariness of the day's work. I would also like to thank my friend Dr. George Isaac for his encouragement at difficult times.

My thesis is part of the research program, studying rare-earth transition metal permanent magnet systems, principally supported by grants from the Department of Energy to Professor Cadieu (Grant #: DE-FG02-86ER45265).

CONTENTS

LIST OF TABLES

LIST OF FIGURES

CHAPTER 1

INTRODUCTION

For a good permanent magnet we need high saturation magnetization, high Curie temperature, and large easy axis anisotropy energy. Even though transition metals Fe, Co, and Ni have high Curie temperature and saturation magnetization they have low coercivity (resistance to demagnetization). On the other hand rare-earth metals have high magnetic moment per atom, strong single ion magneto-crystalline anisotropy but low ordering temperature. In rare-earth transition metal compounds we can use the intrinsic properties of both partners, namely, high single ion anisotropy of the rare-earth and high magneto-coupling of the 3d transition metal partners.

Within the past few years a new class of materials for making permanent magnets has been developed based on Co, Fe, and some of the rare-earth elements. High performance permanent magnetic material based on light rare-earth (atomic number < Gd) transition metal compounds are Co based alloys of $SmCo_5$, Sm_2Co_{17} with added trace elements, and Fe based $Nd_2Fe_{14}B$. The highest known energy products have been obtained in Fe based $Nd_2Fe_{14}B$ ($(BH)_{max}$ = 45 MG-Oe), but its Curie temperature is low (T_c of $Nd_2Fe_{14}B$ = 573 K).

Cobalt based permanent magnet materials are characterized by their high magnetic ordering temperature (T_c of $SmCo_5$ = 1020 K, T_c of Sm_2Co_{17} = 1223 K).

The rare-earths form many compounds with the transition metals. There has been rapidly increasing interest in the development of Co-RE (RE = rare-earth) compounds as permanent magnets after the discovery of high magneto-crystalline anisotropy of YCo_5. Even though $RECo_5$ compounds (RE = Y, La, Pr, Sm or mischmetal) seem to have favorable properties to be good permanent magnet materials,[1] the potential has been realized only in the case of $SmCo_5$ because of its powerful anisotropy field. $SmCo_5$ has an anisotropy field of 400 KOe which is the highest among all known materials. The significance of $SmCo_5$ does not lie with its saturation magnetization. On a per atom basis the magnetization is only about 60% of that of elemental iron and only about 80% of elemental cobalt. The utility of $SmCo_5$ is derived from its powerful anisotropy. For a material to be a good permanent magnet there must be something to clamp the moment in place after the aligning field is removed. In the case of $SmCo_5$ this is the crystal field interaction. $SmCo_5$ is hexagonal, its atomic moment lies along the hexagonal axis, which is the easy direction of magnetization. The anisotropy field is that field required to twist the moment to 90°. In order to fully utilize the high anisotropy of RE-TM compounds, the material must be prepared in defect free fine particle form (single domain) such that the

magnetization reversal takes place by coherent rotation against the anisotropy field. Then the material's intrinsic coercivity is limited only by the anisotropy field ($_iH_c = 2K/M_s$, where K is the anisotropy constant and M_s is the saturation magnetization). In the case of $RECo_5$ compounds magnetization reversal takes place mainly by nucleation and domain wall rotation. This is because it is difficult to prepare fine particles without defects. Even with a very large anisotropy field of 400 KOe for $SmCo_5$, the measured room temperature intrinsic coercive force is no more than 10 to 15% of this value.

Even though RE_2Co_{17} compounds have higher saturation magnetization and Curie temperature compared to 1:5 compounds, their coercivities are limited by low magneto-crystalline anisotropy. Among all the RE_2Co_{17} compounds only those with Sm, Er, Th, and Yb exhibits the easy axis anisotropy. Among these Sm_2Co_{17} is the most anisotropic (anisotropy field = 65 KOe). Pure Sm_2Co_{17} cannot be fabricated into permanent magnets because of its low coercivity (≈ 2 KOe). Preferential substitution of Mn, Cr or Zr into the so called "dumb-bell" Co sites increases the anisotropy and coercivity[3-4] of Sm_2Co_{17}. High energy product (>25 MG-Oe) permanent magnets have been made with $Sm_2(Co,Fe,Cu)_{17}$ systems and energy products have been improved with small addition of Zr, Hf, Ti, and Nb.

Since Co is comparatively scarce and expensive research is carried out on Co free permanent magnet materials. This research was carried out in rare-earth iron rich compounds because Fe is more abundant and has an ionic radius which is very close to the value for Co. In consideration of the similarity of chemical properties between Fe and Co, we could expect that TM_5Sm and $TM_{17}Sm_2$ type compounds, which are stable in the Co-Sm system and exhibit hard magnetic properties, might appear in the Fe-Sm compound system. Pure Sm-Fe systems exhibits $SmFe_2$, $SmFe_3$, and Sm_2Fe_{17} in both film[5] and bulk[6] form. In contrast to the binary $SmCo_5$ phase, $SmFe_5$ does not exist and other Fe rich binary phases do not exhibit hard magnetic properties. The close proximity of Fe and Co in the periodic table (very close ionic radii) suggests an interesting basic research problem involving the non-existence of the $SmFe_5$ phase and a new question as to whether it is possible to synthesize a 1:5 phase with a third element addition. This thesis will be directed to the investigation of the ternary phase of Sm-Fe-M (M = non-magnetic element). Sm-Fe-M exhibited several additional soft and hard magnetic phases[7] in the Fe rich region with M = Ti or O.

Earlier we have observed three different magnetic phases in the Fe rich Sm-Fe-Ti sputtered films under different sets of sputtering conditions. They were: $Sm_2(Fe,Ti)_{17}$, $(Sm+Ti)Fe_5$, and $Sm(Fe,Ti)_3$. $Sm_2(Fe,Ti)_{17}$ shows planar anisotropy. The Curie temperature of

$Sm_2(Fe,Ti)_{17}$ is 385 K which is very low. For the (Sm+Ti)Fe_8 phase,[8] a $(BH)_{max}$ of 12 MG-Oe with $_iH_c$ of 10 KOe was reached at -100° C for fields up to 90 KOe. The $Sm(Fe,Ti)_2$ system[9] exhibits a large perpendicular anisotropy of $4*10^6$ erg/cm^3.

We have discovered a new magnetic phase that contained only Sm, Fe, and Ti in film form that exhibited an in-plane intrinsic coercive force, $_iH_c$, of 38.5 KOe[10,11] at room temperature and 58 KOe at 5 K. This high $_iH_c$ Sm-Fe-Ti phase is important because it has the highest coercive force among all the Co free light rare-earth film magnets that exhibit ferromagnetic coupling between the rare-earth and the transition metal sublattice. This opens a new possibility of Co free permanent magnetic material. This high $_iH_c$ phase has been made in a two step process. First the material has been deposited in an amorphous state with a magnetic field applied in the substrate plane and across its width and then the deposit has been crystallized *in situ* with the same magnetic field which we call H_s. In the film plane magnetic fields have been applied during the sputter deposition and during the crystallization to induce in-the-film-plane anisotropies into the growing films. Due to the magnetic field applied during crystallization the films were magnetized as they were removed from the sputtering system. Low field magnetometer measurements up to ±20 KOe were insufficient to change the magnetization state of such films. Consequently for applied field less than 20 KOe these films exhibited an extreme in-the-film-plane anisotropy. Sm-Fe-Ti samples

were synthesized that exhibited an effective in-the-film-plane anisotropy constant of at least 10^7 erg/cm^3. This value was obtained by magnetizing the film in the film plane parallel, and then perpendicular to the magnetic field applied during the sputter deposition and crystallization. This induced anisotropy of 10^7 erg/cm^3 within the film plane is the largest ever reported as far as we know. As a function of composition, the high $_iH_c$ Sm-Fe-Ti phase has been shown to exhibit a maximum room temperature intrinsic coercivity of 38.5 KOe at a nominal composition of $Sm_{20}Fe_{70}Ti_{10}$. This high $_iH_c$ Sm-Fe-Ti phase we report as a hexagonal 1-5 related phase with a = 8.76±0.01 A°, and c = 25.62±0.01 A°. The 1-5 derived composition for this structure via the 2-7 phase corresponds to $Sm_7(Fe,Ti)_{30}$. In addition the magnetic properties of the high $_iH_c$ Sm-Fe-Ti systems containing small amounts of Al, V, and Zr have been studied.

Films that have been directly crystallized onto heated substrates have exhibited several crystal phases such as 2-17, 1-5 as a function of composition and temperature. In addition we have discovered another new magnetic phase in the Fe rich region in Sm-Fe-Ti systems which exhibited a soft magnetic phase of the $ThMn_{12}$-type at a nominal composition of $Sm(TiFe_{11})$. The x-ray pattern of this phase has been fitted to a tetragonal $ThMn_{12}$-type structure[12] with lattice parameters a = 8.589±0.002 A°, and c = 4.798±0.002 A°. We also

synthesized Sm-Fe-Ti magnetic films that exhibited (300) and (220) textures of the 2-17 phase.

A systematic experimental research has been conducted by varying the sputtering parameters such as substrate temperature, sputtering gas pressure, deposition rate, and the distance between the target and the substrate. A qualitative model relating the H_a effect with grain size was developed. The model is applied to the films prepared both ways: by crystallizing the amorphous deposits, and as directly crystallized onto heated substrates. In this thesis synthesis of magnetic films with special anisotropy as well as magnetic properties in relation to sputtering parameters will be discussed.

CHAPTER 2

INTERMETALLIC COMPOUNDS OF Fe, Co or Ni WITH RARE-EARTH ELEMENTS

2.1 INTRODUCTION

Out of the 104 elements in nature only three transition metals Fe, Co, and Ni and one rare-earth element Gd are ferromagnetic near room temperature. Their magnetic properties are listed in Table 1. Atoms contain many electrons, each spinning about its own axis and moving in its own orbit. The magnetic moment associated with each kind of motion is a vector quantity, parallel to the axis of spin and normal to the plane of the orbit. The magnetic moment of the atom is the vector sum of all electronic moments. There are two possibilities: (1) The magnetic moment of all the electrons are so oriented such that they cancel one another, and the atom as a whole has no net magnetic moment. This condition leads to diamagnetism, i.e, the moments of all the electrons in an atom cancel one another in zero magnetic field, but each orbit reacts to an applied field by producing a moment antiparallel to that field. Therefore each atom acquires a negative moment when the external field is on. (2) The cancellation of electronic moment is only partial and the atom is left

with a net magnetic moment. Such atoms are called magnetic atoms. Material consisting of magnetic atoms are para, ferro, antiferro or ferrimagnetic. In the case of paramagnets the atomic moments point at random and cancel one another, so that the magnetization of the material is zero in the absence of an external field. When a field is applied only partial alignment results because of thermal agitation.

Elements that are ferromagnetic such as Fe, Co, and Ni have atoms in which one electron shell contain fewer than the maximum number of electrons which are required to form a closed shell. Their electronic structures are listed in Table 2. In such unfilled shells there are one or more unbalanced electron spins, giving rise to small magnetic moments and making the atom itself a tiny magnet. Ordinarily in a large collection of such atoms the atomic moments point in various directions and cancel one another. If a sample of ferromagnetic material is placed in an external magnetic field, the individual atomic magnets tend to line up so that when the sample is removed from the field, it retains a net residual magnetism with an observable north and south pole. The total magnetization of a material is the sum of the contributions of all the elementary atomic magnets. If all the atomic magnets are parallel and pointing in the same direction, the magnetization in that direction reaches saturation, the maximum value.

Rare-earth elements such as Sm, Nd are antiferromagnetic near absolute zero and paramagnetic near room temperature. Antiferromagnetic materials at 0 K consist of two interpenetrating and identical sublattices of magnetic ions, each spontaneously magnetized to saturation in zero field, but in opposite directions. So an antiferromagnet has no net spontaneous moment and can acquire a moment only when a strong field is applied. In ferrimagnets there are two sublattices each being spontaneously magnetized in opposite directions. The magnitude of the sublattice magnetizations are not equal, thus resulting in a net spontaneous magnetization.

The transition metals Fe, Co, and Ni are characterized by high values of ordering temperature (Curie temperature). Since they have low coercivity (resistance to demagnetization) they are not suitable for permanent magnets. Rare-earth elements possess high magnetic moment per atom, strong single ion magneto-crystalline anisotropy (due to highly localized 4f electrons) but low ordering temperature. Hence in the elemental form neither transition metals nor rare-earth elements are suitable for permanent magnetic material. Rare-earth and transition metal compounds benefit from intrinsic properties of both partners, namely, high magneto-coupling strength (high ordering temperature) of 3d transition metal and high single ion anisotropy of the rare-earth. The high value of magnetic moment measured for rare-earth atoms at low temperature and the ferromagnetic behavior observed for the transition metals serves as

the principal driving force behind the investigation of RE-TM compositions. The probability of forming new ductile alloys between rare-earth and Fe, Co, and Ni is very small because of the difference in atomic radii. Atomic radii of Sm^{+3} = 1.00, Nd^{+3} = 1.04, Fe^{+3} = 0.64, Co = 0.63 A°, respectively. Hence for practical purposes we must study intermetallic compounds. Due to the limited solubility of rare-earth elements into transition metals the thermodynamic equilibrium crystal structure exists only as a delicate balance between the attractive ionic energy and repulsive electronic energy. This delicate requirement is readily demonstrated by the fact that $SmCo_5$ exists whereas $SmFe_5$ does not exist in bulk form. Intermetallic compounds of light rare-earths and transition metals form higher performance magnetic materials than any other systems. Notable examples are $SmCo_5$ which have anisotropy fields of 400 KOe near room temperature and $Nd_2Fe_{14}B$ which have a maximum energy product of 45 MG-Oe.

2.2 THE CRYSTAL STRUCTURE OF RE-TM COMPOUNDS

A general survey of the various structures observed in binary RE-TM[13-15] compounds are listed in Table 3. The structure of compounds $RE-TM_2$, $RE-TM_3$, $RE-TM_5$, and RE_2-TM_{17} are related and originated from the hexagonal lattice of $CaCu_5$ type[16] through simple substitution accompanied by layer shifts. Therefore this series of compounds serves as the base for the study of different magnetic interactions operating in RE-TM compounds.

2.3 AMORPHOUS RE-TM COMPOUNDS

From the theoretical point of view an amorphous magnetic compound is the most highly disordered system where the atom position, spin direction, and spin magnitude are all random.[17] A simple case is spin glass which consists of a dilute solution of magnetic element in non-magnetic host. In this case atom positions are fixed but spin direction is random.

The structure of amorphous compounds can be described by two principle models: 1) dense random packing and 2) microcrystallites.[18] System like $HoCo_5$ are described by microcrystallite models whereas system like Gd-Co, TbFe are described by dense random packing. In general RE-TM amorphous compounds still contain major features of the d band and give rise to long range magnetic order.

Amorphous RE-TM compounds are found to retain relatively high T_c (often above room temperature) and magnetic moments comparable with those of their crystalline counterparts. Amorphous RE-TM compounds are of great technical interest due to their potential application in thermomagnetic information storage,[19] bubble devices,[20] and as precursor material for preparation of permanent magnets.[21] Amorphous RE-TM compounds can be prepared by the sputter deposition method using high sputtering rate and low substrate

temperature. In fact sputtering at liquid helium temperature with sputtering rate of a few A°/s always produce amorphous films.

2.4 MAGNETISM IN RE-TM COMPOUNDS

The 4f electron shell of the RE and the 3d electron shell of the TM (Fe, Co, and Ni) are only partially full. The unpaired electrons in these shells give rise to observed magnetism. The 4f electron in the RE atoms are shielded by other electrons in the 5s and 5p shells. The observed moment in the case of RE is a composite of both orbital and spin contributions. In the case of iron group ions the 3d shell is the outermost shell. The 3d shell experiences the intense inhomogeneous electric field produced by neighboring ions. This inhomogeneous electric field is called the crystal field. The orbital angular momentum is essentially quenched due to the crystal field and the contributions to the total magnetic moment is essentially from the spin of the unpaired electrons. The high value of magnetic moment measured for RE atoms at low temperature and the ferromagnetic behavior observed for the transition metals served as the principal driving force behind the investigation of RE-TM compositions.

2.4.1 MAGNETIC INTERACTIONS

The magnetism of RE-TM compounds is determined by the following three types of magnetic interactions.

(1) the TM-TM interaction

(2) the RE-RE interaction

(3) the RE-TM interaction

We will discuss these three interactions separately.

2.4.2 TM-TM INTERACTION

In the 3d transition metals the valence electrons are of two types: 4sp conduction electrons - also known as 'itinerant' electrons or just s electrons - and the 3d electrons. It is well known from quantum mechanics that the valence electrons have no separate identities, but only probability densities of being in the various states. Reference to s or d electrons are meant in terms of probability densities. The orbital angular momentum of the 3d electrons are essentially quenched by the crystal field because the 3d electrons are on the outer edges of the atom. Thus the 3d transition metal elements, in contrast with the rare-earths, have magnetic moments that are essentially due only to their electronic spins.

The first approach to explain ferromagnetism is based on the model of Heisenberg and Bethe. In this model it is assumed that the d electrons are all localized (d_1), i.e., strongly attached to individual atoms and the spins are aligned because the energy of the system is lowered by the direct exchange interaction between the adjacent atoms with parallel spins. This simplistic approach conflicted with experimental facts such as (1) The moments of Fe, Co, and Ni are not integers: they are 2.2, 1.7, and 0.6 Bohr magneton respectively and (2) The values of low temperature specific heats of Fe, Co, and Ni are too high to be caused by the number of s like electrons known to be present, suggesting the presence of other conduction electrons.

The second approach pursued by Bloch, Frenkel, and Stoner assumed that all the valence electrons, both 4sp and 3d are itinerant, that is they are able to move freely through the lattice. This model is so intractable that no practical solution has resulted from it. The experimental evidence also appeared to conflict with the all itinerant model. The entropy associated with the transition through the Curie temperature (i.e., from the magnetic to the non-magnetic state) indicates that Fe and Ni have degrees of freedom due to local moments.

In the early 1950's Zener proposed a somewhat different model incorporating both local and itinerant features. According to this model the d electrons were localized and they polarized the s-like

conduction electrons, which then aligned the atomic spins. The s-d_1 exchange polarization would give rise to an oscillatory spatial polarization of the conduction electrons which falls off rapidly with distance from the localized moment. These conduction electron polarizations are referred to as the RKKY[22] (Ruderman-Kittel-Kasuya-Yosida) oscillations or Friedel oscillations. In the case of iron it was shown that the s electron polarization was negative[23] at the first two neighbors. Thus, the polarization of s electrons at the distance of the first nearest neighbor from an iron atom is in the opposite direction of that of the atom itself. This tends to align the Fe atoms antiferromagnetically.

Since both direct interactions between localized d_1 electrons and the coupling through s-like conduction electrons had been ruled out as causing ferromagnetism, it was then proposed[23] that the coupling of the localized d_1 electrons was through a small number of itinerant d_1 electrons. RKKY theory shows that the negative polarization of s-like conduction electrons at first neighbor distance occurs because there are too many 4s electrons in Fe, about one per atom. The form of conduction electron polarization around a local moment is a function of $Cos2k_Fr$ and $Sin2k_Fr$ where k_F is the wave vector at the Fermi surface. The first node occurs at k_Fr = some constant. Since k_F depends on the number of conduction electrons, if k_F and hence the number of conduction electrons is large, r is small, and the first node occurs at a distance closer than the nearest neighbor atom.

Properly modified RKKY theory is also applicable to the d_t conduction electrons. Now the condition for ferromagnetism is that the first node be beyond the first neighbor distance. An upper limit to the number of d_t electrons obtained from RKKY theory is about 0.4 d_t electrons per atom. Thus at most about 5% (0.4/8*100) of the d electrons can be itinerant in Fe, Co, and Ni. Because d_t electrons have an orbital symmetry very similar to that of d_t electrons, the d_t-d_t Coulomb exchange interaction is considerably stronger than the s-d_t interaction causing Fe, Co, and Ni to be ferromagnetic.

The TM-TM interaction is the strongest one operative in the RE-TM compounds as compared to RE-RE and RE-TM. This is due to the much larger spatial extension of the 3d wave functions of TM compared to 4f wave functions of RE. The TM-TM interaction in RE-TM compounds is studied in which the component RE is non-magnetic such as La or Lu. The observed high ordering temperature of these compounds is the experimental evidence for the stronger TM-TM interactions.

2.4.3 RE-RE INTERACTION

The interaction between the magnetic moment of the rare-earths atoms is the weakest compared to TM-TM and RE-TM interactions. Due to the small spatial extension of the 4f wave functions there is virtually no overlap between them. Hence the magnetic coupling has

to proceed indirectly. One possible path of interaction is the spin polarization of the s conduction electrons. The 4f moments located elsewhere in the crystal feel this polarization and orient themselves accordingly. The conduction electron polarization due to the 4f moment is not uniform in space. The interaction between the localized 4f moment and the free conduction electrons is of the oscillatory type that decreases with distance from the rare-earth ion. The interaction between the localized 4f moment and the conduction electron is known as RKKY[24] interaction. This interaction leads to parallel as well as antiparallel coupling between moments. The strength of this coupling depends on structure type and the number of conduction electrons. The stronger TM-TM interaction usually obscures the RE-RE interaction in RE-TM compounds. Experimental evidence that RE-RE interaction in RE-TM compounds is indeed weak can be obtained through the low values of ordering temperature measured in the case where the TM atoms do not carry a magnetic moment.[25]

2.4.4 RE-TM INTERACTION

The spin of the RE and the TM atoms are always aligned antiparallel in the RE-TM compounds.[26,27,28] A positive RKKY interaction between the conduction electrons and the 4f electrons of the REs causes the spin of the 4f electrons to be antiparallel to that of TM atoms. The RKKY interaction between the localized 4f and free conduction electrons is of oscillatory type that decreases with

distance from the RE ion. While phenomenologically the antiparallel coupling between the RE and the Co spins can be explained by invoking the RKKY interaction, the theory provides little insight into the sign of the coupling.[29] Buschow[30,31] has, therefore, argued that the 4f-3d interaction proceeding through a direct exchange between 5d(RE)-3d(TM) electrons, proposed by Campbell,[32] more appropriately describes the observed coupling. This scheme treats the 5d electrons as localized, their positive spins arising from an ordinary 4f-5d exchange. By treating the REs as belonging to the first half of a d-transition metal series (in regard to 5d electronic behavior) and Fe and Co belonging to the second half of such a series, Campbell was able to explain the antiferromagnetic coupling between the RE and TM spins.

According to Hund's rules the total angular momentum J = L - S when the shell is half full and J = L + S when the shell is more than half full. S is the maximum value of the total spin allowed by the Pauli exclusion principle and L is the maximum value of the orbital angular momentum consistent with the value of S. When the shell is just half full, L = 0, J = S. For the REs with atomic number smaller than Gd, the spin and the orbital angular momentum oppose each other and the total angular momentum J = L - S. For REs with higher atomic number the total angular momentum J = L + S. Because the RE and TM spins are antiparallel, only RE-TM compounds which consist of light rare-earth metals, for which J = L - S show ferromagnetic behavior.[33,34] For Gd and RE's with higher atomic

numbers, RE moments couple antiferromagnetically with the TM moments; these compounds are ferrimagnetic.

2.5 MAGNETIC ANISOTROPIES

The shape of the hysteresis loop strongly depends on the magnetic anisotropy which controls most of the magnetic properties of the material. The term magnetic anisotropy means that the magnetic properties depend on the direction in which they are measured. The anisotropy manifests itself as a preferred direction in the material along which the magnetic moments align themselves. When an external magnetic field is applied along the preferred axis of magnetization the material saturates easily compared to when the field direction is normal to it. The preferred axis of magnetization is called the easy axis and the direction normal to it is called the hard axis. The easy axis is characterized by minimum free energy. The energy involve in the anisotropy is much smaller than the exchange energy. Anisotropies can be classified as magneto-crystalline, shape, stress, and anisotropy induced by magnetic annealing. Of these only crystal anisotropy (magneto-crystalline) is intrinsic to the material.

2.5.1 MAGNETO-CRYSTALLINE ANISOTROPY

Magneto-crystalline anisotropy is due mainly to spin-orbit coupling. The exchange energy associated with spin-spin coupling is given by $E_{ex} = -2J_{ex}S_i.S_j = -2J_{ex}S_iS_jCos\theta$, where J_{ex} is called the

exchange integral and is related to the overlap of the charge distribution of the atoms i and j. J_{ex} occurs in the calculation of the exchange effect and θ is the angle between the spins. The exchange energy depends only on the angle between the spins, and not at all on the direction of spin relative to the crystal lattice. Therefore spin-spin coupling cannot contribute to the crystal anisotropy. When an external field is used to reorient the spin of an electron, the orbit of that electron also tends to be oriented because of spin-orbit coupling. The orbit is coupled to the lattice and therefore resists the attempt to rotate the spin axis. The energy required to rotate the spin system of the domain away from the easy direction, called the anisotropy energy is the energy required to overcome the spin-orbit coupling. Although there is no doubt that crystal anisotropy is due to spin-orbit coupling, the details are not clear.

In the case of a hexagonal crystal the magneto-crystalline anisotropy energy is given by $E = K_1 Sin^2\theta + K_2 Sin^4\theta$, where θ is the angle between the magnetization and the c-axis and K_1 and K_2 are anisotropy constants of the material. For strongly uniaxial materials, K_2 is much smaller than K_1 and can usually be ignored. A positive value for the coefficients corresponds to preference of magnetization along the c-axis and negative one for preference within the basal plane. $K_1 + K_2$ is the energy required to force the direction of magnetization from the easy to the hard direction.[35] It corresponds to the difference in the area between the initial magnetization curves

obtained along the easy and hard directions and the applied magnetic field axis. When one coefficient is negative and the other is positive intermediate situations such as easy cone anisotropy arise.

2.5.2 SHAPE ANISOTROPY

If the specimen is spherical in shape, the same applied field will magnetize it to the same extent in any direction if there is no crystal anisotropy. If the specimen is non-spherical, it will be easier to magnetize it along a longer axis than along a short axis because of the demagnetizing field. The demagnetizing field along a shorter axis is stronger than along a long axis. Thus the shape alone can be a source of magnetic anisotropy. The energy associated with the demagnetizing field of the specimen, called the magnetostatic energy, $E_{ms} = (1/2)N_dM^2$, where N_d is the demagnetizing coefficient and M is the magnetization. For a prolate spheroid, $E_{ms} = (1/2)M^2N_c + (1/2)(N_a-N_c)M^2\mathrm{Sin}^2\theta$, where N_c and N_a are demagnetizing coefficients along c (semi major axis) and along a (semi minor axis) and θ is the angle between M and the long axis. In this case the shape anisotropy constant is given by, $K_s = (1/2)(N_a-N_c)M^2$. The energy due to shape anisotropy is written as $E = K_s\mathrm{Sin}^2\theta$. The strength of the shape anisotropy depends both on the axial ratio c/a of the specimen, which determines N_a-N_c, and the extent of magnetization.

2.5.3 STRESS ANISOTROPY

Stress alone can create an easy axis of magnetization. Stress anisotropy is a uniaxial anisotropy. We therefore write the stress anisotropy energy, which is a magnetoelastic energy, $E_{me} = K_\sigma \mathrm{Sin}^2\theta$. The stress anisotropy constant is given by, $K_\sigma = (3/2)\delta_{si}\sigma$, where δ_{si} is the saturation magnetostriction, σ is the stress, and θ is the angle between σ and M. The axis of stress is an easy axis if $\delta_{si}\sigma$ is positive. If this quantity is negative, the stress axis is a hard axis and the plane normal to the stress axis is an easy plane of magnetization.

2.5.4 ANISOTROPY INDUCED BY MAGNETIC ANNEALING

When certain compounds are heat treated in a magnetic field and then cooled to room temperature, they develop a permanent uniaxial anisotropy with the easy axis parallel to the direction of the field during heat treatment. They are then magnetically softer along this axis than they were before treatment. The annealing temperature must be below the Curie point of the material and yet high enough, so that substantial atomic diffusion can occur. The field must be large enough to saturate the specimen during the magnetic anneal, if the resulting anisotropy is to develop its maximum extent. In this case the anisotropy energy is given by, $E = K_u \mathrm{Sin}^2\theta$, where K_u is the anisotropy constant and θ is the angle between M_s and the direction of the annealing field.

2.6 COERCIVITY MECHANISMS

A ferromagnet in the demagnetized state is divided into a number of small regions called domains. Each domain is spontaneously magnetized to the saturation value M_s, but the direction of magnetization of the various domains are such that the specimen as a whole has no net magnetization. The process of magnetization is then one of converting the specimen from a multi-domain state into one in which it is a single domain magnetized in the same direction of the applied field. Domain walls are interfaces between regions in which the spontaneous magnetization has different directions. At or within the wall the magnetization must change direction. Exchange energy in a ferromagnet is a minimum when the spins are parallel. Hence the wall would have large exchange energy associated with it. This can be decreased if we allow the 180° change in spin direction to take place gradually over a number of atoms. Spins within the wall are pointing in non-easy directions, so crystal anisotropy energy within the wall is higher than it is in the adjoining domains. Exchange energy tends to increase the wall thickness whereas anisotropy energy tends to decrease it. This gives rise to a finite width and structure for domain walls.

In particles below a certain size it is energetically unfavorable to internally support domain walls. Below the critical size the

particle will prefer to remain in the single domain state. For $SmCo_5$ the single domain particle size for bulk arc-cast samples has been measured to be 1.6μm. For the subsequently crystallized $SmCo_5$ films, the grain size was shown to be no more than 600±60 A°. The grain size for the subsequently crystallized high $_iH_c$ Sm-Fe-Ti films which we are going to discuss in chapter four is 500 to 600 A°. According to the Stoner-Wohlfarth model,[36] when the field is reversed the single domain particles reverse their magnetization through coherent rotation of the magnetic moments. For domain reversal by coherent rotation in strongly uniaxial anisotropic materials, the intrinsic coercive force, $_iH_c$, will be equal to the anisotropy field $H_A = 2K/Ms$. The maximum observed intrinsic coercive force for $SmCo_5$ ranges from 40 to 60 KOe. This corresponds only to 10 to 15% of the theoretical upper limit. For the high $_iH_c$ Sm-Fe-Ti system we observed maximum intrinsic coercive force, $_iH_c$, of 38.5 KOe. Using rigorous micromagnetic arguments, Brown[37] has shown that for perfect ellipsoidal particles no specific size determines single domain behavior and that domain reversal should always proceed through the coherent rotation process with $_iH_c$ of the order of the anisotropy field. This is contradictory to experiment, which shows that in actual fine particle magnets, $_iH_c$ increases as the particle size is reduced; this inconsistency with the experiment has been attributed to departure from perfect ellipsoidal shape and homogeneity and is referred to as Brown's paradox.[38]

Due to the inability to obtain the largest theoretically obtainable value for $_iH_c$ in the $RECo_5$ powders, Becker concluded that the reversal process in these compounds was determined by mechanisms other than coherent rotation of the domains. The lower than expected value for $_iH_c$ was explained by a model which included nucleation of reversed domains (with the field reversal) and their rapid growth to completely reverse the magnetization of the particle.[39,40-43] The domain nucleation process can be visualized as the formation of small reversed domains assisted by local demagnetizing fields, through coherent reversal of the magnetic moments at low anisotropy sites.[44] Domain nucleation occurs at various defects in the material, such as inclusions, stacking faults, and compositionally inhomogeneous regions. Since the probability that a given particle will contain a defect decreases with decreasing particle size, nucleation dominated magnetization reversal mechanism require the synthesis of small particle (and grain) size materials. However, the interparticle and intergranular magnetostatic interaction should be sufficiently low that each particle or grain functions magnetically independent of its neighbors.[45]

In the refinement of the domain nucleation and growth reversal model, Becker[43] identified two types of nuclei. Type 1 nuclei were identified as those that trapped segments of the domain wall as they traversed the defects; what remained were small regions of reversed

domains bounded by locally pinned fragments of the domain wall as they swept past these defects. Type 2 nuclei were identified as those that were characterized by large local demagnetizing fields and provided sites for reverse domain nucleation. The effect of type 1 nuclei can be minimized by the application of magnetizing fields sufficiently large to remove the reversed domains from the material. This type of nuclei can therefore be deactivated by the application of a large field. With fields smaller than those required to drive the domain wall out of the material, the region of reversed domain remains and leads to quick reversal of the samples during subsequent demagnetization. Consequently type 1 defects will not provide the same nucleating effects for both senses of magnetization, being active primarily only in one direction. Type 2 nuclei, on the other hand, are symmetrical in both senses of magnetization reversal and have a characteristic nucleating event at the same field in either case. At sufficiently large field strengths, the type 1 site is deactivated and the reversal is primarily determined by nucleation at a type 2 site. It is perhaps more appropriate to discuss reversal in terms of nucleation of domain wall movement as opposed to nucleation of the wall itself.[46] Nucleation of small reversed domains will lead to reversal only if the nucleation field exceeds the pinning field required for the domain wall displacement.

CHAPTER 3

EXPERIMENTAL PROCEDURE

3.1 MAGNETIC FILM SYNTHESIS

The film magnets were fabricated by rf diode sputtering from sets of three targets in a stainless steel ultra high vacuum chamber with base pressure in the 10^{-7} to 10^{-9} torr range. Glow discharge sputtering is a widely used technique for the deposition of semiconductor, metallic, magnetic, and insulating films and is well documented in the literature.[47,48,49] Special methods have been developed for the deposition of rare-earth transition metal permanent magnet films that exhibit high intrinsic coercive forces, large remanent values, and special anisotropies. By special anisotropies we mean that the easy direction of magnetization can be aligned perpendicular to the film plane, or in a specific direction within the plane of the film. The sputtering conditions employed differ from normal rf diode sputtering in two main respects. Relatively high sputtering gas pressures have been used to thermalize the sputtered atoms by collision with the sputtering gas atoms before their arrival at the substrates. This selective thermalization method originally was used by Cadieu[50] in synthesizing superconducting films with high T_c : Nb_3Ge (T_c = 22 K). In addition, during the sputter deposition a magnetic field, H_s = 1.75 KOe was applied in the plane of the

substrate and across the width to introduce anisotropies into the growing films. The sputtering gas used was usually Ar at pressure ranging from 75 to 150 micron. In some cases a two component sputtering gas of Ar and Xe in the ratio of 3:1 has been used. The sputtering gas pressures were measured and monitored by capacitance manometers which allowed the pressure measurements to be independent of the particular gas in use. During the deposition the polished, polycrystalline, Al_2O_3 substrate could be either water cooled or heated to temperatures up to 700° C. Films deposited onto heated substrates were crystalline upon deposition. Such films we term directly crystallized. Films that were deposited onto water cooled substrates were amorphous, as confirmed by x-ray diffraction and hysteresis loop of low coercivities. Certain of the amorphous films were crystallized *in situ* right after sputtering by heating the substrates to a suitable temperature for sufficient time to promote complete crystallization. Film samples that were made first amorphous, and then subsequently crystallized, corresponded most closely to bulk samples. Such samples were highly dense and free of voids. Their surfaces were specular reflecting and mirror like. Samples that were directly crystallized onto heated substrates exhibited a distinct columnar growth morphology and void structure from the sputtering process. Such films usually exhibit a dark appearance due to crystal facets at the surface diffusing scattered light.

For sputtering there were basically two types of targets we used, namely, uniform composition targets and gradient composition targets. These alloy targets were button shape ingots that we arc-melted in our specially designed arc-melter with dynamic flush-cleaning action with Ar. This action was especially necessary for reactive rare-earth elements. The details of the specially designed arc-melter were reported earlier by Cadieu *et al.*[51] A custom sputtering electrode was used so that sputtering occurred from three targets simultaneously, which we term trisputtering. The sputtering target arrangement was such that a range of compositions was deposited along the length of the 5 cm long Al_2O_3 substrate. Samples with slightly different atomic compositions but identical preparation condition could then be analyzed by observing small subregions. By varying the target composition individually, a range of compositions could then be created in the deposited film so that a systematic gradient occurred in one or more component in the deposited film.

3.2 SELECTIVE THERMALIZATION

In the sputtering process high energy ions bombard the surface of a sputtering target and eject surface atoms by momentum transfer as opposed to boiling. The ejected surface atoms called sputtered atoms were predominantly neutral atoms with an asymmetric energy distribution centered at approximately 5 to 10 ev and extending up to 100 ev. These high energy particles have to be slowed down or

thermalized before they strike the substrate. Thermalization means simply the removal of excess momentum and kinetic energy of the sputtered atoms to lower their temperature to that of the substrate by collisions with the sputtering gas atoms before they arrive at the substrate. The use of selective thermalized sputtering allows the newly arriving sputtered atoms to replicate and add to any crystallites that had started to grow as seeded crystallites. The mean free path is proportional to 1/p, where p is the sputtering gas pressure. The higher the pressure of the sputtering gas, the shorter the mean free path and the more energy transferring collisions are encountered between the target and the substrate. Increasing the distance from the target to substrate also has the effect of increasing the number of collisions between the target and the substrate. Therefore, relative distance from the target to substrate is important. The atomic mass of the sputtering gas is important in the thermalization process. If the mass of the sputtering gas is approximately equal to the mass of the sputtered atoms, then there is a large average transfer of energy during a collision. If the sputtering gas is much lighter or heavier than the sputtered atoms, on the average less energy is transferred during the collision and it takes more collisions to reach the same final energy. The model used for such calculations treats the collisions between the sputtered atoms and the sputtering gas atoms as elastic collisions between spheres having Maxwellian velocity distribution corresponding to temperatures T_1 and T_2 respectively.

The average energy loss of the sputtered atoms per collision normalized to the average energy of the sputtered atoms is given by, $f = 8m_1m_2(1-T_2/T_1)/[3(m_1+m_2)^2]$.[52] The fractional energy remaining is given by $b = 1 - f$. The energy in Kelvins of sputtered atoms after n collision is given by, $E = (E_0-T_2)b^n + T_2$,[50] where E_0 = initial energy in Kelvin, $n = psl/T_2$ is the number of collisions suffered over a distance l, p is the sputtering gas pressure in millitorr, and s is the scattering cross section. This model can be extended to a mixture of sputtering gases and the equation becomes $E = (E_0-T_2)b_1^n b_2^q + T_2$ where n and q are the number of collisions suffered by gases 1 and 2 respectively.

The calculated change in the sputtered atoms energy as the sputtered atoms progress from the target to the substrate using the above model is shown in Fig. 3.1. As indicated in Fig. 3.2, the pressure of 5 millitorr or less which is the most commonly used value in sputtering work is not large enough to thermalize the sputtered atoms for a target substrate distance of a few centimeters. Sputtering gas partial pressures are adjusted so that the sputtered atoms are thermalized as they arrive at the substrate. We term this special case selective thermalization. The sputtering gas used was usually Ar at pressures ranging from 75 to 150 micron. In some cases a two component sputtering gas of Ar and Xe has been used. The purpose of this dual sputtering gas is to more effectively thermalize the relatively lighter Fe atoms by collisions with Ar atoms and to simultaneously thermalize the more massive Sm atom by

collisions with the Xe atoms. Collisions of energetic Sm (150.4 amu) atoms with Xe (131.30 amu) atoms results in larger energy transfer than for Ar, due to the closer matching of atomic masses.

3.3 EFFECT OF THE APPLIED MAGNETIC FIELD DURING THE SPUTTER DEPOSITION AND CRYSTALLIZATION

During the sputter deposition a magnetic field, H_s = 1.75 KOe was applied in the plane of the substrate and across its width. The magnetic field H_s has been applied with the anticipation that it will break the symmetry in the film plane and induce an in-the-film-plane anisotropy into the growing film samples. If the deposition temperature is below the magnetic ordering temperature, the sputtered film would have an induced magnetic anisotropy after the sputtering. The application of a magnetic field during magnetic film synthesis has been used previously by several other groups either to promote perpendicular texturing for crystalline Sm-Co films[53] or to promote uniaxial in-plane anisotropy for flash evaporated amorphous Sm-Co films.[54]

When amorphous films are made and then crystallized subsequently with a magnetic field H_s applied in the substrate plane the effect of the magnetic alignment energy can be a more dominant factor in determining the crystal texturing and hence easy axis alignment for the films. Another attribute of films that are first deposited amorphous is that the specular reflecting mirror like

surface of the amorphous film can be maintained during the subsequent crystallization of the films. The crystallization has usually been performed by heating the film *in situ* in the sputtering system for a suitable time and at a sufficiently high temperature to cause complete crystallization. Normally films that have been directly crystallized by thermalized sputtering so as to exhibit optimum magnetic properties exhibit angle dependent reflective properties. This is due to the large preferentially textured grains that comprise the surface. The grains that result from crystallizing amorphous films are generally less than the single domain particle size. The high $_iH_c$ property of the $SmCo_5$ and high $_iH_c$ Sm-Fe-Ti system films is due to the single domain grain size resulting from the crystallization process. For the subsequently crystallized $SmCo_5$ films,[55] the grain size was shown to be no more than 600±60 A°. Such grain size for $SmCo_5$ is well below the single domain particle size as measured by Livingston and Mc Connel,[56] so that grain of this size would constitute single domain particles. The grain size for the subsequently crystallized high $_iH_c$ Sm-Fe-Ti films which we are going to discuss in chapter four has a measured grain size of 500 to 600 A° diameter. This values were determined by Scanning Electron Microscope measurements.

The small roughly spherical shaped grains functions magnetically independent of each other with the field H_s to induce the in-the-film-plane anisotropy during the crystallization process. The magnetic alignment energy of a magnetic domain in an external

magnetic field is proportional to the magnetic moment. Hence the magnetic alignment energy is proportional to the grain size provided the grain size does not exceed the single domain particle size. For uniaxial ferromagnetic systems the easy direction of magnetization would be coincident with the uniaxial direction or c-axis for single crystals of hexagonal or tetragonal systems. The magnetic alignment energy favors the aligning of the easy axis of the material because the easy axis is characterized by minimum energy. When the films were deposited in an amorphous state, the field H_s was effective in inducing in-the-film-plane anisotropy due to short-range order. This order is due to the formation of microcrystallites within the amorphous media, which is necessary to account for how the observed in-the-film-plane anisotropy was incorporated into the films. During the crystallization process crystallites of sufficiently small size so as to be single domain particle size are formed. For the single domain regions to effectively interact with the magnetic field H_s, it must be possible to crystallize the material at temperatures which are less than the Curie point. In addition the scalar product of the field H_s and the total magnetization over the number of formula units in a domain must be at least as large as the thermal energy encountered during the crystallization process. For the $SmCo_5$ films and the high $_iH_c$ Sm-Fe-Ti films the magnetic alignment energy can be greater than k_BT so that in-the-film plane anisotropy can be induced.

A spherical grain of diameter D would contain $N = (\pi/6)*D^3/V_{f.u}$, where N is the number of formula units in the grain and $V_{f.u}$ is the average volume of a formula unit. The corresponding maximum magnetic alignment energy $E_m = N*\mu(T)\mu_B H_s$, where $\mu(T)$ is a temperature dependent number giving the number of Bohr magnetons per formula unit for the saturation magnetization and μ_B is the Bohr magneton.

At 300 K, the temperature at which the deposition of amorphous film takes place, equating the magnetic alignment energy and the thermal energy yields, $E_m = N*\mu(T)\mu_B H_s = k_B T$. This gives an average grain diameter of 35 A° for $\mu(T) = 8.5$ and $H_s = 2$ KOe in the case of $SmCo_5$.[55] Microcrystallites embedded in amorphous film of at least this size range, which would be too few to be readily observed by the x-ray diffractometer, are needed to agree with the observed in-the-film-plane anisotropy.

For T = 700° C, for the magnetic alignment energy of a domain to equal $k_B T$ requires $D = (\mu(T))^{-1/3}(1.1*10^2)$ A°. This requires a sufficiently large number of $SmCo_5$ formula units in the grains to satisfy $N*\mu(T)\mu_B H_s = k_B T$. At the temperature required for crystallization to occur, the saturation moment per formula unit has fallen to a low, but non zero value since the Curie point of $SmCo_5$ is 724° C. A value of $\mu = 0.1$ yields D = 240 A°, which is less than the SEM grain size of 600 A°. On the basis of this model, grains of at least 240 A° are needed to yield any observable in-the-film-plane

anisotropy. Such a grain size for $SmCo_5$ is well below the single domain particle size as measured by Livingston and Mc Connel,[56] so that grains of this size would constitute single domain particles. An in-the-film-plane magnetic field is needed during the high temperature crystallization, since heating $SmCo_5$[55] composition films without any applied field has been shown to destroy the original in-the-film-plane anisotropy.

When the crystallites are formed by crystallizing the initial amorphous deposit, we assumed that the energy considerations concerning H_s acted over a certain volume region of the forming crystallites. For directly crystallized films, only the new surface region is able to interact with the field H_s so that correspondingly larger grains would be needed to yield a magnetic alignment energy for the grains that would be larger than k_BT. In addition, the newly arriving surface region is growing onto the seeded crystal provided by the columnar growth pattern. This crystal seeding effect is generally stronger than the magnetic alignment energy provided by the field H_s and the newly growing surface region. In this case the magnetic alignment energy $E_{Mlayer} = (\pi/4)(V_{f.u})^{-2/3}L^2\mu(T)\mu_BH_s$, where L is the diameter of a surface region. For equivalent T and energies, $(\pi/6)D^3(V_{f.u})^{-1}\mu(T)\mu_BH_s = (\pi/4)(V_{f.u})^{-2/3}L^2\mu(T)\mu_BH_s$ will give $L^2 = (2/3)D^3(V_{f.u})^{-1/3}$. For T = 700° C as before a surface domain diameter of L = 1400 A° would be required to give an equivalent magnetic energy to induce magnetic anisotropy into the growing films. This grain size is larger than that normally

encountered as measured by x-ray line broadening. Generally it has not been possible to directly crystallize films onto heated substrates that exhibit an appreciable degree of in-the-film-plane anisotropy. The fact that the newly interacting layer is replicating an already seeded columnar crystal imposes an additional constraint. The preferential growth of columns having easy axis aligned with the applied field would be favored. This would be expected to be a small effect since the magnetic alignment energy is generally small compared to the crystal energy. The directly crystallized films have columnar and void structures that do not correspond to bulk arc-cast samples. The amorphous films which are subsequently crystallized do not exhibit any columnar or void structure.

In the above discussion, the presence of a spontaneous magnetization within the magnetic domain was used to estimate the magnetic alignment energy available for inducing an in-the-film-plane anisotropy. This requires that it be possible to have the system crystallize at temperatures less than the Curie point. If the substrate temperature is above the Curie point, the exchange energy would be very small and the magnetic correlation length would then be much smaller than the grain size. In fact, that is why we did not observe any noticeable H_s induced anisotropy effect resulting from crystallizing the low Curie temperature $Nd_2Fe_{14}B$ phase. It should be noted that the H_s did induce in-the-film-plane anisotropy when corresponding samples were measured after being deposited in an amorphous state, but before crystallization. The water cooled

substrate temperatures used were below the Curie temperature so that microcrystallite domain orientations could be affected by H_s. Previously amorphous films of Sm-Co based systems and Sm-Fe-Ti systems were shown to exhibit large in-the-film-plane anisotropy when deposited under thermalized sputtering conditions with an in-plane field H_s applied during the deposition.[57] Amorphous samples of the Sm-Fe-Ti composition were sputtered with H_s and then heated to temperatures of 450 to 510° C without any applied magnetic field. The original as-sputtered amorphous film exhibited large in-the-film-plane anisotropy. After heating these samples in the absence of any applied field, the original in-the-film-plane anisotropy was destroyed. This shows that it was necessary for a field to be applied during the crystallization for the in-the-film-plane anisotropy to be observed, even if the original amorphous film exhibited in-the-film-plane anisotropy.

3.4 FILM THICKNESS

The film thickness can be determined by the relation m = t*A*d, where m is the mass of the film, t is the thickness, A is the area, and d is the density of the film. The major source of error in estimating the thickness is in the uncertainty in the density of the deposited material. The density of the bulk could be different from that of the film by a few percent due to slightly different lattice parameters and the presence of voids. The necessary corrections for the lattice parameter difference were obtained from our x-ray

diffraction results. Investigation using SEM reveals dense packing, suggesting that the error in using x-ray density as the actual over all density was at most few percent. The thickness measured using the SEM is also consistent with the thickness estimated from the x-ray density. Another method that we could use for thickness measurement was by measuring the reflection of β electrons from the film using various β decay sources that give different β electron energies. Since we were measuring reactive rare-earth transition metal compounds, calibration standards were difficult to prepare. The film thickness for samples which we are going to discuss is fairly uniform and ranges from 1 to 12 micron. Little substrate specific effects are expected for films of these relatively large thickness. Deposition rate of 1.5 to 4 A°/s were used to deposit these relatively thick films.

3.5 FILM COMPOSITION

The composition of the film was determined on the substrate by examining small regions of the deposited material by either x-ray fluorescence or by using electron excited x-ray analysis in the SEM. The x-ray fluorescence measurements were calibrated by comparison to results on pseudofilms prepared by drying solutions of known concentration of elements onto filter papers.[58] The electron excited x-ray analysis was performed by using a Si(Li) detector and a Princeton Gamma-Tech 4 plus analysis system. Calibration was performed by spectra runs with pure elements and programs

provided by Princeton Gamma-Tech. The oxygen content of the film was checked by Auger Electron Spectroscopy with ion gun depth profiling.

3.6 LATTICE PARAMETERS

Traditionally either the graphical or analytical methods are used to index x-ray powder patterns of non-cubic crystals.[59] Our films are mostly hexagonal or tetragonal in structure. Since non-cubic crystals have two or more parameters to be determined, both methods require extensive calculations. It is very difficult and sometimes even impossible to index low-symmetry crystal structures. Even when the structure is known, the best values of the lattice parameters requires a nonlinear fitting procedure to take advantage of the increased accuracy of high angle diffraction lines.

A schematic illustration of the x-ray diffractometer is shown in Fig. 3.3. Our data count versus angle is collected by Multi Channel Analyzer and then stored in a microcomputer for later data processing. Our basic procedure involves the determination of the weighted root mean square angular deviations between the observed and calculated Bragg angle 2θ based on a given structure and lattice parameters. The weighted root mean square deviation F(a,c) is calculated for each of a and c sets. $F(a,c)=\{\Sigma[(2\theta_{iexp}-2\theta_{cal})^2\sin^2(\theta_{iexp})*\tan^2(\theta_{iexp})]^{1/2}\}/N$,

$N = [\Sigma\sin^2(\theta_{iexp})*\tan^2(\theta_{iexp})]^{1/2}$.

The sum is over the number of observed diffraction peaks at the Bragg angles 2θ. The lattice parameter was calculated by minimizing F(a,c) for various a and c pairs. Essentially we are looking for the vertex point in the F(a,c) versus a and c 3-dimensional graph. The optimum lattice parameters were chosen to be the minimum point on the surface F(a,c) by cross-sectional projection for the a and c parameters.

3.7 MAGNETIC MEASUREMENTS

The magnetic measurements were performed at room temperature using a Princeton Applied Research Model 155 vibrating sample magnetometer. The magnetic field was supplied by a conventional water cooled electromagnet up to 20 KOe. The films were cut into different regions approximately 0.2 cm by 0.2 cm for magnetic measurements. The Al_2O_3 substrate is diamagnetic with an isotropic magnetic susceptibility at room temperature of $-0.4*10^{-6}$ emu/g/Oe. The total moment of a typical size region of 0.04 cm^2 was measured to be $-5*10^{-4}$ emu at a magnetic field of 20 KOe. This was about 1% of the magnetization of our sample and hence the substrate contribution to the moment at low field has been neglected. High field measurements were made using a Janis Varitemp superconducting magnetometer system with fields up to 90 KOe. For the high field measurements the diamagnetic contribution of the holder and substrate has been taken into account and the necessary correction has been applieed. The Curie temperature was measured in the high temperature oven supplied by PAR.

CHAPTER 4

HIGH $_iH_c$ Sm-Fe-Ti PHASE BY SUBSEQUENT CRYSTALLIZATION FROM ORIGINALLY SPUTTERED AMORPHOUS DEPOSITS

4.1 INTRODUCTION

The pure Sm-Fe systems exhibits only 1-2, 1-3 and 2-17 phases in both film[5] and bulk[6] form. The crystallographic and magnetic data are listed in Table 4. In contrast to the Sm-Co system the important 1:5 phase is not known to exist in pure Sm-Fe system. The Sm_2Fe_{17} phase does not posses hard magnetic properties to qualify as a permanent magnetic material. The Sm_2Fe_{17} phase has a low coercivity of only 0.1 KOe[60] at 4.2 K and fairly low Curie temperature of 385 K.

Earlier our group reported the successful synthesis of a metastable $SmFe_3$ phase[8] with Ti additions by selectively thermalized sputtering and an $Sm(Fe,Ti)_2$ system[9] which exhibits a large perpendicular anisotropy of $4*10^6$ erg/cm^3. Also our group reported the synthesis of a phase which contains only Sm, Fe, and Ti in film form which exhibits an in-plane intrinsic coercive force, $_iH_c$, of 24 KOe at room temperature.[61]

Recently we have reported the synthesis of a new high intrinsic coercive force, $_iH_c$, of 38.5 KOe at room temperature Sm-Fe-Ti phase that was prepared by crystallizing originally amorphous sputtered deposits.[10,11] By this method the material was originally deposited from a set of targets onto water cooled Al_2O_3 substrate. Then the deposits have been crystallized *in situ* right after sputtering by heating the substrate to a suitable temperature for sufficient time to promote complete crystallization. Films that were deposited onto water cooled substrate were amorphous as confirmed by x-ray diffraction and hysteresis loop of low coercivities. A number of experiments showed that the atomic percentage of Sm incorporated into the film is a strong function of the substrate temperature used during the sputter deposition and crystallization whereas the Ti/Fe ratio is comparatively fixable. As a function of composition, the high $_iH_c$ Sm-Fe-Ti phase has been shown to exhibit a maximum room temperature intrinsic coercivity of 38.5 KOe at a nominal composition of $Sm_{20}Fe_{70}Ti_{10}$. This high $_iH_c$ Sm-Fe-Ti phase is found to be a $SmCo_5$ related hexagonal structure with a nominal formula of $Sm_7(Fe,Ti)_{20}$. A magnetic field H_s has been applied during the sputter deposition and crystallization to induce in-the-film-plane anisotropies into the growing films. For the uniaxial system to exhibit in-the-film-plane anisotropy, there must be a preferential alignment of the c-axes within the film plane. It has been possible to synthesize Sm-Fe-Ti films that have exhibited in-the-film-plane

anisotropy for fields of ±20 KOe. This corresponds to an effective anisotropy constants of 10^7 erg/cm^3 for magnetizing the film in-plane parallel versus perpendicular to the direction of the field H_s applied during sputtering and subsequent crystallization. This is larger than the previously known highest value of in-the-film-plane anisotropy achieved in amorphous rare-earth transition metal films.[57]

4.2 MAGNETIC PROPERTIES

The high $_iH_c$ Sm-Fe-Ti films have been made in a two step process. First the material was deposited in an amorphous state and then the deposits were crystallized *in situ* with an in-the-film-plane magnetic field H_s. Due to the magnetic field applied during the sputter deposition and crystallization the film was magnetized as it was removed from the sputtering system.

In Fig. 4.1 the high field hysteresis loop measured at room temperature in-plane and parallel to H_s for a Sm-Fe-Ti film is shown. This film was sputtered amorphous in an in-plane field of 1.75 KOe and then crystallized in the same field. The in-plane $_iH_c$ was 31 KOe. At 90 KOe magnetizing field in the film plane, $4\pi M$ was 5.4 KG. The magnetization has not been fully saturated by the available field of 90 KOe. Arc-melted buttons with compositions 14.54 at.% Sm, 80.12 at.% Fe, and 5.34 at.% Ti were used as targets for sputtering this film. The target x-ray pattern shows both 1-12 and 1-2 phases.

This particular film has a composition 20.92 at.% Sm, 73.33 at.% Fe, and 5.75 at.% Ti respectively. During the sputtering the Sm concentration in the film is enhanced over that of the target by the conditions used. In Fig. 4.2 the second quadrant behavior of the same sample as in Fig. 4.1 is shown measured at 5 K. The measured coercivity was 58 KOe. The x-ray diffraction pattern for Cu K_α radiation for the same sample is shown in Fig. 4.3. The high $_iH_c$ Sm-Fe-Ti sample hysteresis loops exhibited a gradual drop in magnetization at the beginning of the second quadrant. This drop in magnetization and the diffraction pattern supported the hypothesis that the sample contained an admixture of a semi-soft phase in addition to the high $_iH_c$ phase.

The maximum coercive force observed at room temperature was 38.5 KOe for a composition of $Sm_{19}Fe_{73}Ti_8$. For this composition the maximum coercive force observed at 168 K was 45 KOe. In Fig. 4.4 we show the hysteresis loop for a $Sm_{19}Fe_{73}Ti_8$ sample as measured in the film plane parallel to the H_s direction. The x-ray diffraction pattern for Cu K_α radiation for the same sample is shown in Fig. 4.5. This sample had a semi-soft second phase with a saturation flux of 0.4 KG, which is less than 10% of the saturation flux of the hard phase. A flux of 0.4 KG was subtracted for fields >6 KOe and added for fields of <-6 KOe. It was estimated from magnetic data that 80 to 85% by volume was that of the hard magnetic phase.

The in the film plane squareness ratios, $M_r/M_{(90KOe)}$, remanent moment to moment at 90 KOe when originally magnetized in the film plane parallel to H_s are summarized in Table 5. The maximum squareness ratio 0.887 is for the sample having the maximum intrinsic coercive force, $_iH_c$, of 38.5 KOe. The available field of 90 KOe was not able to saturate our film samples. An important aspect of the hysteresis loop is the gradual drop in moment as the second quadrant is entered. This indicates that a semi-soft phase is present in addition to the high $_iH_c$ phase. The semi-soft phase present in the samples has a coercivity of about 6 KOe. We list the ratio $M_{(-6KOe)}/M_r$, the moment at -6 KOe to remanent moment in Table 5. We can see from the Table 5 that as the coercive force increases, the ratio $M_{(-6KOe)}/M_r$ decreases indicating that the amount of semi-soft magnetic phase in the admixture decreases.

The room temperature intrinsic coercive force of the hard Sm-Fe-Ti phase observed in film samples has been measured as a function of composition. The maximum coercivity observed at room temperature was 38.5 KOe for a composition of $Sm_{19}Fe_{73}Ti_8$. In Table 6 we list the intrinsic coercive force at room temperature for various Sm-Fe-Ti films. In Fig. 4.6 we show the $_iH_c$ value versus (Ti+Fe) at.%. High $_iH_c$ values, >20 KOe, were only observed for a several percent range in (Ti+Fe) at.%. In Fig. 4.7 we show the coercivity at room temperature versus Ti/Fe atomic ratio for amorphous Sm-Fe-Ti films which were subsequently crystallized. For

the high coercive force sample the Sm concentration ranges from 17 to 22 at.%. These samples showed some traces of semi-soft second phase which helps to explain the Ti/Fe width for which the high $_iH_c$ samples could be formed.

In Fig. 4.8 we show the $_iH_c$ and $4\pi M$ values as a function of temperature from 5 K to 273 K at approximately 70 K intervals. This particular film has an intrinsic coercive force, $_iH_c$, of 34 KOe at room temperature. A linear decrease from 46 KOe at low temperature to 35.25 KOe at 273 K was observed. The $4\pi M_{max}$ observed at 5 K was 7.62 KG and the maximum energy product was 4.50 MG-Oe.

Since these high coercivie force samples have been made by crystallizing films originally deposited in an amorphous state, it is not expected that the films will be strongly textured. It is thus not possible to directly saturate the samples even with fields of 90 KOe. The expected saturation magnetization for the high $_iH_c$ Sm-Fe-Ti phase based on the fitted hexagonal cell is 11.8 KG for $4\pi M_s$. It is estimated that the anisotropy field based on magnetization measurements up to 90 KOe in-plane and out of plane is 230 to 300 KOe.

4.3 EFFECT OF SUBSEQUENT CRYSTALLIZATION TEMPERATURE AND TIME ON COMPOSITION OF Sm-Fe-Ti FILMS

In section 4.2 we described the magnetic properties of high $_iH_c$ Sm-Fe-Ti films. Such films are first sputtered onto a water cooled Al_2O_3 substrate in an in-plane magnetic field and subsequently crystallized *in situ* for sufficient temperature and time to promote complete crystallization. Films that were deposited onto water cooled substrates were amorphous as confirmed by x-ray diffraction pattern and hysteresis loop of low coercivities. An x-ray diffraction pattern of such an amorphous film is shown in Fig. 4.9. This particular amorphous film has composition 29.36 at.% Sm, 63.96 at.% Fe, and 6.75 at.% Ti. In Fig. 4.10 we show the x-ray diffraction pattern of Sm-Fe-Ti film sputtered onto water cooled substrate and crystallized at 410° C *in situ* for 135 minutes. The x-ray pattern shows only a broad hump which indicates that the sputtered film was amorphous and the temperature 410° C was not enough to cause any significant crystallization. The amorphous deposit had crystallized at 450° C as shown by the x-ray diffraction pattern in Fig. 4.11.

To obtain the hard magnetic phase in the Sm-Fe-Ti systems a certain range of Sm at.% and Ti/Fe ratio in the film are required. The proper crystallization temperature is also very important. A number of experiments were carried out to investigate the occurrence of this hard magnetic phase in the Sm-Fe-Ti systems. They showed that the film composition corresponding to the hard magnetic phase

should contain 17 to 22 at.% Sm and 0.07 to 0.15 of Ti/Fe ratio. In addition to the composition of the target sputtered, the experiment indicated that the substrate temperature used during the subsequent crystallization has a critical effect on film composition. In particular the Sm at.% incorporated into the film was found to be a strong function of the substrate temperature used during the subsequent crystallization. This function is shown in Fig. 4.12. The composition of the subsequently crystallized Sm-Fe-Ti films in the temperature range 440° to 600° C is shown in Table 7(a) and 7(b). The target configurations for the sputtered film in Table 7(a) and 7(b) were different. It is shown that the fractional value of Sm decreases with increasing temperature whereas the Ti/Fe ratio is comparatively fixable. It should also be noted that to obtain the hard magnetic phase and thus good magnetic properties, the composition of the film is an essential but not sole factor. As shown in Table 7(b), although the film F510 contains the right composition for the hard magnetic phase, it doesn't show good magnetic properties. This resulted from the fact that the substrate temperature of 450° C was not high enough to complete the hard phase crystallization. Even though this sample exhibits a room temperature intrinsic coercive force, $_iH_c$, of 9 KOe, it contains more of the softer magnetic phase as confirmed by the hysteresis loop. The films F504 and F505 in Table 7(b) exhibited inferior properties since the corresponding crystallization temperature was too high to have enough Sm in the film and thus no hard magnetic phase could be formed. Such films show a

predominant (110) peak of the αFe phase (2θ = 44.2°) as shown by the x-ray diffraction pattern in Fig. 4.13.

The effect of crystallization time on composition is also investigated. The experiments showed that the Sm at.% incorporated into the film seems not to be very dependent on the subsequent crystallization time. This was indicated in Table 8(a) and 8(b) in which the Sm at.% doesn't change much as the subsequent crystallization time is varied. In Fig. 4.14 we show the x-ray diffraction pattern of a Sm-Fe-Ti film subsequently crystallized at 470° C for 24 hours. This particular film has composition 18.45 at.% Sm, 72.49 at.% Fe, and 9.06 at.% Ti. Prolonged crystallization results in rapid deterioration in coercivity and second quadrant behavior as confirmed by a hysteresis loop of low coercivity.

The high $_{i}H_{c}$ Sm-Fe-Ti phase is formed during a short diffusion heat treatment at temperatures between 450° and 510° C. Above this temperature the at.% Sm in the film drops drastically. We etched the surface of some of the high $_{i}H_{c}$ sample with dilute nitric acid. We checked the composition of these samples before and after etching to see whether there is any enhancement of Sm at.% below the surface. For the high $_{i}H_{c}$ phase samples there is no noticeable change in at.% of Sm. This is indicated in Table 8(c). Sample F504 shows enhancement of Sm below the surface. Before etching this sample show a predominant α-Fe phase as confirmed by x-ray diffraction.

This enhancement in Sm is thought to be due to preferential etching of Fe.

It is shown that for optimum magnetic properties in the high $_iH_c$ Sm-Fe-Ti system, the best subsequent crystallization temperature ranges from 470° to 510° C and the best crystallization time is approximately 135 minutes. In this temperature range the at.% of Sm doesn't change much indicating a plateau region. Above this temperature the subsequently crystallized Sm-Fe-Ti film shows a predominant αFe phase whereas the prolonged *in situ* crystallization at the temperature to form the hard magnetic phase results in the increase of the softer phase. In conclusion, for the occurrence of the high $_iH_c$ Sm-Fe-Ti system, the film should have a nominal composition of $Sm_{20}Fe_{70}Ti_{10}$ after sputtering and subsequent crystallization. The hard magnetic phase is formed during a short diffusion heat treatment at temperature between 450° and 510° C.

4.4 IN-THE-FILM-PLANE ANISOTROPY

In Fig. 4.15 is shown the in-plane variation in the magnetization when a high $_iH_c$ Sm-Fe-Ti compound sample was rotated in a constant magnetometer field of 18 KOe. This sample was sputtered amorphous and subsequently crystallized in the presence of an in-plane magnetic field of 1.75 KOe at zero degree reference angle in the Fig. 4.15. The magnetic field H_s has been applied with the anticipation

that it will break the symmetry in the film plane and induce anisotropy into the growing film samples. Due to the magnetic field applied during the sputter deposition and subsequent crystallization the film was magnetized as removed from the sputtering system. The maximum in-plane moment was observed when the magnetometer field was applied parallel to the original magnetic field direction during sputtering and subsequent crystallization. It is clear that the applied external measuring field of 18 KOe is not large enough to rotate the magnetization by any significant amount away from the induced easy axis, which is the direction of H_s during synthesis.

In Fig. 4.16 hysteresis loops measured at room temperature in-plane parallel and perpendicular to H_s for a Sm-Fe-Ti film are shown. The coercive force measured in the film plane was >21 KOe as deduced from the minor loop. At 16 KOe magnetizing field in the film plane, $4\pi M$ was 3.9 KG. High field measurements made at room temperature for the same sample yielded a room temperature $_iH_c$ value of 31 KOe as shown in Fig. 4.1. Low field magnetic measurements up to ±20 KOe were insufficient to demagnetize or appreciably change the magnetization state of such films. Consequently for applied field less than 20 KOe the film exhibited extreme in-the-film-plane anisotropy. The in-the-film-plane anisotropy was exhibited in this sample because of the in-plane field that had been applied during the synthesis and crystallization. Amorphous samples of Sm-Fe-Ti compositions that were sputtered with

H_s applied were later heated without any field to temperatures of 450° to 510° C. The original as-sputtered film exhibited large in-the-film-plane anisotropy. After heating these samples in the absence of any applied field, the original in-the-film-plane anisotropy was destroyed. This showed that it was necessary for a field to be applied during the crystallization for in-the-film-plane anisotropy to be observed, even if the original amorphous film had exhibited in-the-film-plane anisotropy. It has been possible to synthesize Sm-Fe-Ti films that have exhibited in-the-film-plane anisotropy for fields of ±20 KOe. This corresponds to an effective anisotropy constants of 10^7 erg/cm^3 for magnetizing the film in-plane parallel versus perpendicular to the direction of field H_s. This is larger than the previously known highest value of in-the-film-plane anisotropy achieved in rare-earth transition metal films.[57]

The high $_{\perp}H_c$ values observed for Sm-Fe-Ti films resulted from the small single domain grains created during the crystallization of the amorphous films. The high anisotropy energy prevents the rotation of magnetization within these single particle domains for fields of the order of 20 KOe. For uniaxial systems to exhibit in-the-film-plane anisotropy, there must be a preferential alignment of the c-axes within the film plane. A preferential alignment of the easy axes and hence c-axes of these fine independently acting grains then results from the application of the field H_s during crystallization. A preferential fanning of the c-axes about the H_s direction would be sufficient to explain the observed in-the-film-plane anisotropy.

Fields such as 20 KOe, which are small compared to the anisotropy field, would not be sufficient to rotate the magnetization vectors of non-aligned grains. This accounts for less than expected magnetic moment for full alignment. Thus the magnetic alignment energy tends to align the easy axes and hence the c-axes of the grains. We have previously reported that when amorphous films are crystallized with a magnetic field H_s during crystallization, several conditions are necessary for in-the-film-plane anisotropy to be introduced into the growing films.[55] The conditions were that the crystallization needs to be accomplished below the Curie temperature, that the grains be in the single domain size range, and that the magnetic alignment energy of the moment within a grain M.H be greater than K_BT at the crystallization temperature. It has been difficult to directly measure the grain sizes for some of the subsequently crystallized Sm-Fe-Ti films. Such films present a mirror like surface that needs to be etched lightly before any structure can be seen in the SEM. After lightly etching the surface we were able to measure the grain size of 500 to 600 A° diameter.

4.5 INITIAL MAGNETIZATION BEHAVIOR

As we mentioned in section 4.4 normal low field magnetometer measurements up to ±20 KOe were insufficient to demagnetize or appreciably change the magnetization state of high $_iH_c$ Sm-Fe-Ti films. Consequently for low applied fields less than 20 KOe the film

exhibited extreme in-the-film-plane anisotropy. High field values have been used to demagnetize samples of this type. The film then has been magnetized in the film plane parallel and perpendicular to the field H_s that had been applied during the sputter deposition and subsequent crystallization. In Fig. 4.17 we show the initial magnetization and hysteresis loop measured in-plane parallel to H_s. In Fig. 4.18 we show the initial magnetization and hysteresis loop measured in-plane perpendicular to H_s. There is a repeatable difference in the initial magnetization behavior in these samples when magnetized in-plane parallel and perpendicular to the H_s direction. This shows that the magnetic field that had been applied during the sputter deposition and subsequent crystallization introduced anisotropy into the films in addition to establishing the initial state of magnetization. The initial magnetization for magnetizing parallel to H_s shown in Fig. 4.17 exhibits a well defined activation energy in that the film becomes magnetized between 20 and 40 KOe. In contrast to this, when films were magnetized perpendicular to the original H_s direction the magnetization rose smoothly from near zero to 70 KOe before joining onto the hysteresis loop. The initial magnetization behavior observed in this sample has been observed in about four other samples of this type that have been measured and is believed characteristic of the growth and crystallization process, rather than resulting from the demagnetization process.

4.6 CRYSTAL STRUCTURE OF HIGH $_iH_c$ Sm-Fe-Ti PHASE

The high $_iH_c$ Sm-Fe-Ti samples we report to be composed of two intermixed Ti substituted phases. The two phase nature of these samples is indicated by the gradual drop of moment over about 10 KOe as the second quadrant is entered. The second phase is thus indicated to be soft only when compared to the actual high $_iH_c$ phase. The high $_iH_c$ Sm-Fe-Ti phase we report[63] as a hexagonal 1-5 related phase with a = 8.76±0.01 A°, and c = 25.62±0.01 A°. The 1-5 derived composition for this structure via the 2-7 phase corresponds to $Sm_7(Fe,Ti)_{30}$.[63] The other semi-soft phase can be accounted for as cubic $Sm(Fe,Ti)_2$. The hard phase has been made with room temperature $_iH_c$ values of 30 to 38.5 KOe, while the semi-soft phase has a room temperature $_iH_c$ value of about 6 KOe. It is doubtful that strictly cubic $Sm(Fe,Ti)_2$ can exhibit the observed coercivities of 3 to 4 KOe.[9] Some distortion has probably occurred to account for the anisotropy observed here and previously.[9]

The high coercive force compositions are between the coercivity maxima we have reported for $Sm(Fe,Ti)_2$ subsequently crystallized films and that for hexagonal $(Sm+Ti)Fe_5$ directly crystallized films.[9] An important aspect of the high coercivie force sample hysteresis loop is the gradual drop in moment as the second quadrant is entered. This indicates a semi-soft phase is present in addition to the high $_iH_c$ phase. The semi-soft phase present in the samples has

a coercivity of about 6 KOe. Without Ti substitutions, it is expected that $SmFe_2$ will be cubic with a_o = 7.382 A°. To account for the fairly high anisotropy, it must be assumed that the Ti addition distorts the cubic cell. The smallest distortion can be accomplished by transforming to a tetragonal system with slightly shifted a and c to fit the observed lines. The d-spacings and the intensities for the distorted cell should roughly match those for the lines present from the original undisorted cell. Some additional lines not found for the cubic phase should also be present. The lines assigned to the $Sm(Fe,Ti)_2$ cubic phase can also be fitted to a tetragonal cell distorted from the cubic with a = 7.09±0.01 A°, and c = 7.81±0.01 A°.

The high $_iH_c$ Sm-Fe-Ti phase we take to be a dumbbell substituted 1-5 related structure. The normal Gd_2Co_7 structure has a rhombohedral structure with a = 5 A° as for $SmCo_5$, but c = 9*(c for $SmCo_5$). The hexagonal form has a = 5 A°, and c = 24 A°. The change to the 2-7 from the 1-5 base occurs by a Sm occupying two of the transition metal sites making (6+2):(30-2) = 8:28 = 2:7 for the Sm to Co ratio. If then a transition metal dumbbell pair replaces one of the rare-earths the a parameter goes to $(3^{1/2})a$. The normal hexagonal cell would have c = (2/3)c = 24 A° in this case. The resulting composition would then be 8 RE + 28 TM goes to (7 + 1) RE + 28 TM goes to 7 RE + (28 + 2) TM = 7 RE : 30 TM. The expected concentration for the one dumbbell substitution per 24 A° cell is then 7/37 = 18.9 at.%. The expected density in this case is

7.98 gm/cm³. Two dumbbell substitution per 24 A° cell, would make the Sm concentration 6/38 = 15.8 at.%. The density in that case would be 7.82 g/cm³. The hard phase cell with a = 8.76 A° and c = 25.62 A° provides a fit to better than 0.1° for 34 of the observed lines from 2θ = 27° to 80° for Cu K_α radiation. Only 15 out of 43 lines can be fitted by the rhombohedral 2-7 cell with a = 5.08 A°, and c = 38.41 A° as shown in Table 9. Such a cell without Ti additions has been reported in Ref. 64. A few lines can also be fitted by the rhombohedral 1-3 cell with a = 5.05 A°, and c = 24-26 A°; that would correspond to the $SmFe_3$ analog of $SmCo_3$. Most of the remaining lines can be ascribed to the $Sm(Fe,Ti)_3$ phase.

For this fitting procedure we tried all the possible phases in the Sm-Fe-Ti system. Only 10 out of 43 observed lines can be fit by the 1-12 tetragonal cell with a = 8.56 A°, and c = 4.79 A° as shown in Table 10. None of the observed strong lines are fitted. The most intense line of the 1-12 phase occurs for (hkl) = (321); the corresponding observed line is weak. Also the second most intense line (202) of 1-12 phase doesn't fit. Even though we can fit 10 out of 43 lines within 0.1°, all the corresponding lines are weak. Hence the possibility of 1-12 phase in the high $_iH_c$ Sm-Fe-Ti system is ruled out.

Thirteen out of 43 observed lines can be fit by the 2-17 rhombohedral cell with a = 8.58 A°, and c = 12.50 A° as shown in Table 11. The most intense lines of the 2-17 rhombohedral phases are (220), (303), and (300). Line (303) fit but the corresponding observed line is weak. There is no fit for (220) and (300) lines. Even though we can fit 13 out of 43 lines, the possibility of 2-17 phase in high $_iH_c$ Sm-Fe-Ti system is ruled out.

Thirteen out of 43 observed lines can be fit by the Gd_2Co_7-type rhombohedral cell with a = 5.09 A°, and c = 36.39 A° as shown in Table 12. Only one intense line in the spectrum fit for (2,0,20). The most intense lines for Gd_2Co_7 phase are (119) and (110). In this case there is no fit for the most intense line (119). The second most intense line (110) fit but the corresponding observed line is weak.

Twenty eight out of 43 observed lines can be fit by the Gd_2Co_7-type hexagonal cell with a = 4.99 A°, and c = 36.40 A° as shown in Table 13. The most intense lines for the 2-7 phase are (119) and (110). In this case there is no fit for the most intense line (119). The second most intense line (110) can be fit, but the corresponding observed line is weak.

Twenty six out of 43 observed lines can be fit by the hexagonal 2-7 cell with a = 5.05 A°, and c = 38.35 A° as shown in Table 14. The most intense lines for the 2-7 type cell are (119) and (110). There is no fit for the corresponding lines.

Seven out of 43 observed lines can be fit by the hexagonal 1-5 cell with a = 4.78 A°, and c = 4.37 A° as shown in Table 15. The most intense lines for the 1-5 hexagonal cell are (111), (101), and (200). Lines (111) and (200) fit very well.

Nine out of 43 observed lines can be fit by the rhombohedral 1-3 cell with a = 5.06 A°, and c = 24.91 A° as shown in Table 16. The most intense lines for the 1-3 phase are (202) or (116), and (220). There is no fit for the corresponding lines. In this case five other lines which are excluded from the fitting for the high $_{i}H_{c}$ Sm-Fe-Ti phase and 1-2 phase can be fitted.

Fifteen out of 43 observed lines can be fit by the hexagonal 1-3 cell with a = 5.059 A°, and c = 24.88 A° as shown in Table 17. There is no fit for the most intense lines (116) or (202), and (220). In this case seven other lines which are excluded from the fitting for the high $_{i}H_{c}$ Sm-Fe-Ti phase and 1-2 phase can be fitted.

Usually Sm high anisotropy structures have hexagonal related unit cells. The hexagonal based indexing has more physical relation to other high anisotropy structures than the tetragonal indexing we have previously ascribed to the high $_iH_c$ Sm-Fe-Ti phase.[11] In this case 26 out of 43 observed lines can be fit by the tetragonal cell with a = 8.39 A°, and c = 12.42 A° as shown in Table 18. The most intense line at d = 2.60 A° is assigned to the (311) line of the tetragonal cell. The (311) reflection shows that the c-axis of the tetragonal film is partially out of the film plane. So the film should exhibit a higher moment perpendicular to the film plane direction than parallel to the plane direction. This is not consistent with the magnetic data.

The intense line at d = 2.60 A° is assigned to the $Sm(Fe,Ti)_2$ phase. The strongest reflection for cubic YFe_2 occurs for d = 2.59 A° in agreement with this. The line at this d cannot be fit to the hard phase. The hard phase as most 1-5 derived structures should have its most intense reflection corresponding to d = 2.1 A°. Intense lines corresponding to this d do occur for the high $_iH_c$ Sm-Fe-Ti phase.

In Table 19(a) we list x-ray diffraction d-spacings that have been obtained from the high $_iH_c$ Sm-Fe-Ti film samples. The d-spacings shown are for Cu $K_{\alpha 1}$ radiation. In Figs. 4.19 and 4.20 we show the x-ray diffraction pattern of a high $_iH_c$ Sm-Fe-Ti phase film sample between 25° and 80° values of 2θ for Cu K_α radiation. Based on these patterns hexagonal lattice parameters have been assigned. The indexing is based on a hexagonal cell with one dumbbell per 25.62 A° c-parameter. The corresponding angles were fit to $\leq$ 0.1° for 2θ by a fitting procedure as described in section 3.6. In Figs. 4.21 and 4.22 we show the deviation factor for the lattice parameters a and c based on the hexagonal cell. Table 19(b) lists the d-spacings and indices for the semi-soft Ti substituted $SmFe_2$ phase. The indexing is based on the usual cubic cell. Some distortion of the cubic cell is probably required to account for the anisotropy of $Sm(Fe,Ti)_2$ observed here and previously.[9] Table 19(c) lists the d-spacings and indices for the semi-soft Ti substituted $SmFe_2$ phase distorted from cubic to tetragonal cell with a = 7.09 A°, and c = 7.81 A°. Table 19(c) provides a better fit compared to Table 19(b).

An important aspect of Ti addition is that the dumbbell pairs can be formed without placing Fe onto those sites. When Fe is placed onto dumbbell sites in 1-5 related structures, the anisotropy is lowered, as has been observed for Sm_2Fe_{17}. The second phase which also contains Ti is thought to buffer the Ti onto dumbbell sites. The expected saturation magnetization for the high $_iH_c$ Sm-Fe-

Ti phase based on the fitted hexagonal cell is 11.8 KG for $4\pi M_s$. This result follows by scaling the volume and number of Fe atoms per cell times the saturation magnetization for "$SmFe_5$".

4.7 ORDERING TEMPERATURE OF HIGH $_iH_c$ Sm-Fe-Ti PHASE

In a separate low field magnetometer, ±20 KOe, an attempt was made to measure the Curie temperature of the high $_iH_c$ Sm-Fe-Ti phase. In Fig. 4.23 we show the magnetization as a function of temperature up to 460° C. It was found that with 5 KOe applied magnetic field the moment began to decrease with an extrapolated Curie temperature in the range 440° to 450° C. In Fig. 4.24 we show the thermomagnetic behavior up to 560° C. It was observed that in the temperature range 450° to 480° C the moment began to rise again indicating that the high $_iH_c$ Sm-Fe-Ti phase began to decompose into an Fe rich phase. It is possible that the film sample had become contaminated in the magnetometer upon heating. In Fig. 4.25 we show the x-ray diffraction of the sample after the Curie temperature measurement. The most intense line can be indexed as (110) of the α-Fe phase. It was shown that prolonged heating of the high $_iH_c$ Sm-Fe-Ti phase in the sputtering chamber results in severe deterioration in coercivity and second quadrant behavior. It was also shown that the high $_iH_c$ Sm-Fe-Ti phase show severe rapid deterioration in coercivity and second quadrant behavior upon a few hours exposure to intermediate temperature. These are thought to be

due to oxygen and other contaminants picked up in the vacuum annealing furnace. No deterioration of the hard phase samples with times of at least two years has been observed for samples stored at room temperature. Samples of high $_iH_c$ Sm-Fe-Ti phase subsequently crystallized in the temperature range of 450° to 510° C in the presence of an in-plane magnetic field exhibit an in-the-film-plane anisotropy, which indicates that the Curie temperature of this phase should be in this temperature range.

4.8 SUBSTITUTION OF Al, V, AND Zr IN HIGH $_iH_c$ Sm-Fe-Ti PHASE

4.8.1 INTRODUCTION

After the development of permanent magnetic materials with excellent magnetic properties based on the intermetallic compounds of $Nd_2Fe_{14}B$, $SmCo_5$, and Sm_2Co_{17}, many attempts have been reported to modify the properties of these compounds by substitution of one of their components. In sections 4.2 and 4.3 we described the synthesis of a new high intrinsic coercive force, $_iH_c$, of 38.5 KOe at room temperature Sm-Fe-Ti phase that was prepared by crystallizing the originally amorphous deposits. In this high $_iH_c$ Sm-Fe-Ti sample small amounts of semi-soft Ti substituted $SmFe_2$ phase is also present. We have investigated the effect of addition of small amount of Al, V, and Zr in the high $_iH_c$ Sm-Fe-Ti phase.

4.8.2 RESULTS AND DISCUSSION

Films with Al, V, and Zr addition in the high $_iH_c$ Sm-Fe-Ti phase have been made. The addition of 2.3 to 4.5 at.% of Al helped to stabilize the samples into a more single phase form. In Fig. 4.26 we show the in-plane hysteresis loop of a subsequently crystallized Sm-Fe-Ti-Al film. The in-plane $_iH_c$ measured was 31 KOe. The composition of this film was 17.79 at.% Sm, 70.40 at.% Fe, 9.05 at.% Ti, and 2.76 at.% Al. In Fig. 4.27 we show the initial magnetization and hysteresis loop measured perpendicular to the film plane. The $_iH_c$ measured perpendicular to the film plane was 29 KOe. The composition of this film was 16.34 at.% Sm, 70.65 at.% Fe, 9.40 at.% Ti, and 3.61 at.% Al. In Fig. 4.28 we show the initial magnetization in-plane parallel to H_s and perpendicular to the film plane.

The magnetic properties as a function of composition have been systematically explored by trisputtering narrow composition ranges from a set of three targets so that a narrow composition gradient was made along the length of a substrate. The magnetic properties of high $_iH_c$ Sm-Fe-Ti-Al film samples as a function of composition are listed in Table 20. The maximum $_iH_c$ observed was 33.34 KOe and the maximum observed flux at 90 KOe applied field was 7.12 KG. In Fig. 4.29 we plot the $_iH_c$ values versus Ti/(Ti+Fe) atomic ratio. The $_iH_c$ values were very sensitive to the Ti/(Ti+Fe) atomic ratio. They rose at a rate of +6KOe/%{Ti/Ti+Fe)} as the nominal composition of 19

at.% Sm was approached and started to decrease for higher atomic ratios. The $_iH_c$ values of Sm-Fe-Ti-Al film samples as a function of Sm are listed in Table 21. For these film samples the amount of Al varies from 2.9 to 3.7 at.% and the Ti/Fe ratio varies from 0.10 to 0.14. The $_iH_c$ values of Sm-Fe-Ti-Al film samples as a function of Al are listed in Table 22. For these film samples the amount of Sm varies from 14 to 18 at.% and the Ti/Fe ratio varies from 0.125 to 0.14. In Fig. 4.30 we show the $_iH_c$ values versus Al at.%. The $_iH_c$ values for Al concentration less than 4 at.% did not fall below 30 KOe for proper preparation conditions. In Fig. 4.31 we show the $_iH_c$ values of Sm-Fe-Ti-Al film samples versus $(Sm_xAl_{1-x})_{20}$. The maximum coercivity observed was 33.34 KOe for 16.34 at.% Sm and 3.60 at.% Al. For these film samples the Ti/Fe ratio varies from 0.09 to 0.14. In Fig. 4.32 we show the $_iH_c$ values versus (Ti+Al) at.%. The maximum coercive force 33.34 KOe was observed for 13 at.% of (Ti+Al). For these film samples the amount of Sm varies from 12.40 to 16.34 at.% and the Ti/Fe ratio varies from 0.09 to 0.14. In Fig. 4.33 we show the various phases observed in the Sm-Fe-Ti systems. In Fig. 4.34 we show the variation of $_iH_c$ with composition of Sm-Fe-Ti films. In Figs. 4.35 and 4.36 we show the variation of $_iH_c$ with composition of Sm-Fe-Ti-Al films. The experiments indicated that addition of 2.3 to 4.5 at.% of Al helped to sharpen the x-ray pattern of the high $_iH_c$ Sm-Fe-Ti samples. In Figs. 4.37 and 4.38 we show the x-ray diffraction pattern between 25° and 80° for Cu K_α radiation for a high $_iH_c$ Sm-Fe-Ti sample containing small amount of Al.

The effect of subsequent crystallization temperature on composition of Sm-Fe-Ti-Al system is studied. The composition of Sm-Fe-Ti-Al film samples as a function of subsequent crystallization temperature are listed in Table 23. The at.% of Sm incorporated into the film is a strong function of the subsequent crystallization temperature and is shown in Fig. 4.39. It is shown that for optimum magnetic properties in this system, the best subsequent crystallization temperature ranges from 470° to 510°C. Above this temperature the subsequently crystallized Sm-Fe-Ti-Al system shows a predominant αFe phase whereas prolonged crystallization results in rapid deterioration in coercivity and second quadrant behavior.

The magnetic properties of high $_iH_c$ Sm-Fe-Ti systems containing small amounts of V and Zr have been studied. In Fig. 4.40 we show the in-plane room temperature demagnetization curve of a Sm-Fe-Ti-V sample first sputtered amorphous and then crystallized. The $_iH_c$ values versus composition of subsequent crystallized Sm-Fe-Ti-V film samples are listed in Table 24. In this system high $_iH_c$ values, >18 KOe, were only observed for film samples containing a higher percentage (>15 at.%) Sm for proper preparation conditions. Film samples which contain lower amounts (<15 at.%) of Sm, exhibit more of the semi-soft phase. The concentration of V in the high $_iH_c$ Sm-Fe-Ti-V varies from 3.4 at.% to 4.48 at.%.

The $_{i}H_{c}$ values versus composition of subsequently crystallized Sm-Fe-Ti-Zr film samples are listed in Table 25. In Fig. 4.41 we show the in-plane room temperature demagnetization curve of a Sm-Fe-Ti-Zr sample first sputtered amorphous and then crystallized. High $_{i}H_{c}$ values, >18 KOe, were only observed for film samples containing a higher percentage (>15 at.%) Sm for proper preparation conditions. Film samples which contain lower amount (<15 at.%) of Sm show a greater drop in the second quadrant of the hysteresis loop which indicates the increase of the semi-soft phase. The concentration of Zr in the high $_{i}H_{c}$ Sm-Fe-Ti-Zr varies from 2.2 at.% to 2.9 at.%. The Ti/Fe ratio in Sm-Fe-Ti film samples containing Zr varies from 0.09 to 0.13.

CHAPTER 5

DIRECTLY CRYSTALLIZED Sm-Fe-Ti FILMS

5.1 INTRODUCTION

In the previous chapter we have described the synthesis of a new high intrinsic coercive force, ${}_iH_c$, of 38.5 KOe at 293 K Sm-Fe-Ti phase that was prepared by crystallizing originally amorphous sputtered deposits[10,11] in an in-plane magnetic field H_s. By this method the material was originally deposited from a set of targets onto room temperature, 25° C, Al_2O_3 substrates. The films as-deposited were amorphous, as confirmed by x-ray diffraction and hysteresis loop of low coercivities. The crystallization was performed *in situ* right after sputtering by heating the substrate to a suitable temperature for sufficient time to promote complete crystallization.

To obtain controlled magnetic properties in the films it is desirable that they be directly crystallized onto heated substrates. This allows films to be synthesized that have well defined crystallographic texturing.[62] The orientation of the easy axes of magnetization of the crystallite is then also controlled.

During the sputter deposition there is not an appreciable shift in the Ti/Fe ratio between that of the target and the deposited films. In contrast to this the Sm at.% incorporated into the film is a strong function of substrate temperature. Various sets of targets have been used to sputter Sm-Fe-Ti films such that the Ti/Fe ratio is held fixed, but the Sm at.% in the films is caused to vary by changes in the substrate temperature, sputtering deposition rates, sputtering gas pressure, and target to substrate distance. The objective is to adjust the Sm at.% and Ti/Fe ratio in directly crystallized films corresponding to the composition of the high $_iH_c$ Sm-Fe-Ti phase observed in subsequently crystallized films. In Fig. 5.1 we show the Sm at.% incorporated into the film as a function of substrate temperature. During the sputtering onto the substrate at room temperature, 25° C, the Sm concentration in the film is enhanced over that of the target by the condition used. But as the substrate temperature is raised, the Sm at.% in the deposited film falls off rapidly. In Figs. 5.2 and 5.3 we show the sputtering deposition rates as a function of substrate temperature and target to substrate distance, respectively. In Figs. 5.4 and 5.5 we show Sm at.% incorporated into the films as a function of sputtering gas pressure and target to substrate distance, respectively. For these sputterings, the Ti/Fe atomic ratio in the target was 0.15 and in the film it varies from 0.13 to 0.17.

Films that have been directly crystallized onto heated substrates in an in-plane magnetic field have exhibited several different crystal phases as a function of composition and substrate temperature. They were $Sm(Fe,Ti)_{12}$, $(Sm+Ti)Fe_5$, and $Sm_2(Fe,Ti)_{17}$.

5.2 RESULTS AND DISCUSSION

A new crystalline magnetic phase near 85 at.% Fe has been observed as the major phase in bulk arc-melted ingots and in the sputtered film samples of Sm-Fe-Ti systems.[12] This new magnetic phase has been identified to be of the $ThMn_{12}$-type structure with a coercivity of 1 to 2 KOe range. The target x-ray powder pattern is shown in Fig. 5.6(a). The x-ray pattern can be indexed as having a major phase which is isostructural with the $ThMn_{12}$ compound. This phase was indexed as $Sm(TiFe_{11})$. In Fig. 5.6(b) we show the calculated pattern based on the $SmFe_{12}$, $ThMn_{12}$-type structure with a = 8.579 A°, and c = 4.799 A°. The tetragonal lattice parameters determined were a = 8.579±0.002 A° and c = 4.799±0.002 A°. In Figs. 5.7 and 5.8 we show the deviation factor F for the lattice parameters a and c of $Sm(Fe,Ti)_{12}$ phase of the $ThMn_{12}$-type structure. Here,

$$F(a,c)=\{\Sigma[(2\theta_{iexp}-2\theta_{cal})^2\sin^2(\theta_{iexp})*\tan^2(\theta_{iexp})]^{1/2}\}/N,$$

$$N = [\Sigma\sin^2(\theta_{iexp})*\tan^2(\theta_{iexp})]^{1/2}.$$

The sum is over the number of observed diffraction peaks at the Bragg angles 2θ. The optimum lattice parameters were chosen to be

the minimum point on the surface F(a,c) by cross-sectional projection for the a and c parameters.

Films that have been directly crystallized onto heated substrates exhibited several crystal phases as a function of deposition temperature and composition. Films that have been directly crystallized onto heated substrates at approximately 350° C have been made. These films exhibit only one dominant diffraction line that is consistent with the (200) line of the hexagonal 1-5 phase, as we have reported earlier.[7] The ratio I(200)/I(100) has been made as large as 18. Such films exhibit no reflections with c-axis component out of the film plane. The composition of such film was 74.89 at.% Fe, 20.00 at.% Sm, and 5.11 at.% Ti. Such films are far easier to magnetize in the film plane than out of the film plane. Such a set of hysteresis loops as measured in the film plane and out of the film plane are shown in Fig. 5.9. These results are consistent with the easy axes of the crystallites being aligned onto the film plane. An x-ray diffraction trace of such a textured film is shown in Fig. 5.10. Films synthesized onto substrates heated to between 350° to 450° C exhibit predominantly a $Sm(Fe,Ti)_{12}$ structure as we have reported recently.[12]

Films that have been directly crystallized onto heated substrates in the temperature range of 450° to 480° C exhibit predominantly the (300) reflection of the 2-17 type structure. As shown in Fig. 5.11

such films are far easier to magnetize out of the film plane than in the film plane. This is expected because $Sm_2(Fe,Ti)_{17}$ is an easy plane material. The x-ray pattern indicates that the c-axes, which are the hard axes in this case, lie in the film plane. An x-ray diffraction trace for such a textured 2-17 type film is shown in Fig. 5.12. The composition of this sample was 85.25 at.% Fe, 9.17 at.% Sm, and 5.57 at.% Ti.

Films that have been directly crystallized onto heated substrates with a higher Ti/Fe ratio show a major phase of $Sm_2(Fe,Ti)_{17}$ and a minor phase of $Sm(Fe,Ti)_{12}$. The film sputtered at substrate temperature of 470° C, the $Sm_2(Fe,Ti)_{17}$ phase was predominantly (300) and (220) textured with the c-axes in the film plane. As shown in Fig. 5.13 such films are easier to magnetize out of the film plane than in the film plane. An x-ray diffraction trace for such a textured 2-17 type film is shown in Fig. 5.14. The composition of this film sample was 79.47 at.% Fe, 7.97 at.% Sm, and 12.55 at.% Ti. For the film sputtered at substrate temperature of 440° C, the $Sm_2(Fe,Ti)_{17}$ phase was predominantly (220) textured with the c-axes in the film plane. As shown in Fig. 5.15 such films are easier to magnetize out of the film plane than in the film plane. The x-ray diffraction pattern indicates that the c-axes, which are the hard axes in this case, lie in the film plane. An x-ray diffraction pattern for such a textured 2-17 type film is shown in Fig. 5.16. The composition of this film sample was 79.21 at.% Fe, 8.03 at.% Sm, and

12.76 at.% Ti. In Table 26 we list the coercive force of various directly crystallized Sm-Fe-Ti films sputtered at different substrate temperature.

As mentioned earlier the Sm at.% incorporated into the film is a strong function of the substrate temperature and is shown in Fig. 5.1. By decreasing the Ti/Fe ratio in the target to 0.1 we were able to lock more Sm into the films. Thus we were able to get the composition corresponding to the subsequently crystallized high $_iH_c$ Sm-Fe-Ti phase in directly crystallized films. The high $_iH_c$ Sm-Fe-Ti phase only formed in the film first deposited amorphous and then subsequently crystallized within a temperature range of 450° to 510° C. Even though we got the composition close to the high $_iH_c$ phase composition at the desired temperature range, the high $_iH_c$ phase has not been observed in films made directly crystalline onto heated substrates. The composition of the directly crystallized film sample was 23.76 at.% Sm, 69.54 at.% Fe, and 6.71 at.% Ti. The x-ray diffraction pattern of this sample is shown in Fig. 5.17. The major peaks at 2θ = 43.03° and 30.05° corresponds to (220) and (112) of the 2-17 phase. This particular film exhibit an in-plane $_iH_c$ value of 3.2 KOe.

There is a basic difference between films that are directly crystallized onto heated substrate versus film that are first made amorphous and crystallized subsequently. When films are directly

crystallized onto heated substrates the growing crystallites are bombarded by a flux of sputtering gas atoms, electrons, and incoming sputtered atoms. If there were no competing process, normally the newly arriving sputtered atoms would tend to replicate and add to any crystallites that had started to grow as seed crystallites. Normally this ordered growth is opposed by the momentum of the incoming sputtered atoms being sufficient to disrupt the growth of previously deposited atomic layers. For a collection of randomly arranged crystallites it is expected that certain growth modes would grow faster and crowd out the growth of competing textures. Consequently, particularly for non cubic systems considered here, the growth of films with a preferential texturing can be expected. For uniaxial ferromagnetic systems the easy direction of magnetization would be coincident with the uniaxial direction or c-axis for single crystals of hexagonal or tetragonal system. The demagnetization energy, as well as small c/a ratio both favor films that tend to align the c-axes onto the film plane. In order to minimize the demagnetization energy the growth of crystallites with the easy direction of magnetization in the film plane is favored. But any disruptive atom flux bombarding the substrate during the growth would tend to disrupt preferential growth of crystallites that had the relatively longer c axes aligned onto the film plane. For systems with $c/a > 1$, in order to minimize the demagnetization energy the growth of crystallites with the easy direction of magnetization in the film plane is favored. This would correspond to crystallites that

would have long repeat distance c-axes aligned onto the film plane. But any disruptive flux bombarding the substrate during the growth would tend to disrupt preferentially the growth of crystallites that had relatively longer c-axes aligned onto the film plane. Hence this would favor creation of films with c-axes splayed out of the film plane. Such films would be easier to magnetize perpendicular to the film plane.

Films that have been directly crystallized onto heated substrates by thermalized sputtering in an in-plane magnetic field H_s exhibit angle-dependent reflective properties. Such films exhibit a distinct columnar growth morphology and void structure due to the sputtering process. Such films usually exhibit a dark appearance due to crystal facets at the surface diffusing scattered light. This is due to large preferentially textured grains that comprise the surface. In contrast to this, film samples that were first made amorphous, and then subsequently crystallized, corresponded most closely to bulk samples. Such samples were highly dense and free of voids. A distinguishing feature of the latter films is that the film surfaces were specular reflecting and mirror like.

The grains that result from crystallizing the originally amorphous deposits are generally less than single-domain particle size. The scalar product of the field H_s and the magnetization of the grains at the crystallization temperature yield a magnetic alignment

energy that acts over the three dimensional volume. For the subsequently crystallized Sm-Fe-Ti films the magnetic alignment energy can be greater than K_BT so that in-the-film-plane anisotropy can be induced. For directly crystallized films, only the new surface region is able to interact with the field H_s so that correspondingly larger grains would be needed to yield a magnetic alignment energy for the grains that would be larger than K_BT. In addition, the newly arriving surface region is growing onto the seed crystal provided by the columnar growth pattern. This crystal seeding effect is generally stronger than the magnetic alignment energy provided by the field H_s and the newly growing surface region. The columnar growth pattern of the directly crystallized film imposes an additional constraint that prevents the magnetic alignment energy from being able to rotate the c-axes from the initially growing seeded crystallites. The replicating layer which can interact with the field H_s is constrained from rotating the layer easy axis into alignment with the field H_s by the crystal growth pattern of the columns. Generally, it has not been possible to crystallize films directly onto heated substrates that exhibit an appreciable degree of in-the-film-plane anisotropy. Thus the use of H_s in inducing magnetic anisotropy was highly effective in the diffusion process in the amorphous and subsequent crystallization process and less effective in the stacking process during the crystallization onto heated substrates. The diffusion process within a medium has usually less energy when compared to the stacking process of the formation of

that medium. Thus H_s can influence the diffusion process readily. In the direct crystallization onto heated substrates the layers are replicating themselves according to already deposited layers. Because of this stacking procedure the effective cluster would be more like a two dimensional area rather than three dimensional volume as in the subsequent crystallization process where the films were already deposited.

CHAPTER 6

CONCLUSION

A series of Sm-Fe-Ti film samples have been synthesized by rf diode sputtering for Fe rich compositions. Samples have been directly crystallized onto heated Al_2O_3 substrates as well as first deposited amorphous and then subsequently crystallized. An in-plane magnetic field has been applied during the sputter deposition and during crystallization to induce in-the-film-plane anisotropies into the growing films. By employing, what we term, selectively thermalized sputtering, desired phases were directly synthesized onto heated substrates, so that samples were highly textured and stable on the Al_2O_3 substrate surfaces. The in-the-film-plane magnetic field has been used to achieve a partial preferential alignment of the c-axes within the film plane for crystalline films and also was used to induce large in-the-film-plane anisotropy in subsequently crystallized films. The composition of the film was determined by examining small regions of the deposited material by either x-ray fluorescence or by using electron excited x-ray analysis in the SEM. The oxygen content of the film was checked by AES with ion gun depth profiling. It was about 2.5 at.% for the high $_iH_c$ Sm-Fe-Ti phase. The film thickness studied ranged from 2 to 12 micron. Little substrate specific effects are expected for films of these relatively large thickness. The crystal phase determination was studied by x-ray

diffraction. It was observed that relative intensities of the x-ray peaks, i.e., the texturing could be controlled by varying the sputtering parameters such as deposition rate, H_s, sputtering gas pressure, provided that the sputtering gas pressure was high enough to thermalize the sputtered atoms. It has been found that the direction of easy axis of magnetization with respect to the film plane can be controlled and correlated with a preferential texturing of the crystal structure of the films. The explanation of this observation was based on considerations of the relative flux of disruptive sputtering gas atoms arriving at the substrate compared to metal atoms which were being sputter deposited. It was argued that the relatively large rate of sputtering gas atoms arriving at the substrate would tend to disrupt the growth of relatively long repeat distance growing parallel to the film plane. A model is presented based upon the crystallite grain sizes and magnetic alignment energy that correlates the differences in the degree of in-the-film-plane anisotropy induced into the growing films. The in-the-film-plane anisotropy exhibited in films that had first been made amorphous and then crystallized with a field H_s applied was attributed to the magnetic alignment energy of the single domain particles with the field H_s.

Films that were crystallized directly onto heated substrates generally exhibit columnar crystallites and void structure which were replicated by newly arriving layers of atoms. Film samples that were

first made amorphous and subsequently crystallized were highly dense and free of voids. Such film surfaces were specular reflecting and mirror like. In contrast to this, films that have been directly crystallized onto heated substrates usually exhibit a dark appearance due to crystal facets at the surface diffusing scattered light.

We discovered a new ternary high intrinsic coercive force magnetic phase in the Sm-Fe-Ti system at about 70 at.% of Fe, 20 at.% of Sm, and 10 at.% of Ti. This high $_iH_c$ phase has been prepared by a two-stage process in which the material was first deposited in an amorphous state with a magnetic field in the substrate plane, and then subsequently crystallized *in situ* in the same magnetic field. The room temperature intrinsic coercive force, $_iH_c$, of this hard phase is observed to be 38.5 KOe which is the highest known value in this system where the moments of rare-earth sublattice and transition metal sublattice couple ferromagnetically. The maximum value observed at 168 K was 45 KOe. The high $_iH_c$ values observed resulted from the single domain grains created during the crystallization of the amorphous films. This high $_iH_c$ Sm-Fe-Ti phase is important because it has the highest coercive force among all the Co free light rare-earth film magnets that exhibit ferromagnetic coupling between the rare-earth and the transition metal sublattice. As a function of composition, the high $_iH_c$ Sm-Fe-Ti phase has been shown to exhibit a maximum intrinsic coercivity of 38.5 KOe for a nominal composition of $Sm_{20}Fe_{70}Ti_{10}$. Sm-Fe-Ti film

samples were synthesized that exhibited extreme in-the-film-plane anisotropy for fields of ±20 KOe. This corresponds to effective anisotropy constants of at least 10^7 erg/cm^3. This is the difference in energy when magnetizing the film in the film plane parallel versus perpendicular to the field applied during the sputter deposition and subsequent crystallization. This is the highest reported value of in-the-film-plane anisotropy of which we are aware. Initial magnetization studies have been used to show the influence of the magnetic field during the sputter deposition and crystallization. The high anisotropy energy prevents the rotation of magnetization within the single particle domain for fields of the order of 20 KOe. So far the high $_iH_c$ Sm-Fe-Ti phase has only been observed in samples that were first deposited in an amorphous form and subsequently crystallized within a temperature range of 450° to 510° C. Samples of the high $_iH_c$ Sm-Fe-Ti phase subsequently crystallized in the temperature range of 450° to 510° C in the presence of an in-plane magnetic field exhibit an in-the-film-plane anisotropy which indicates that the Curie temperature of this phase should be in this temperature range.

The high $_iH_c$ samples we report to be composed of two Ti substituted phases. The high $_iH_c$ Sm-Fe-Ti phase we report as a hexagonal 1-5 related phase with a = 8.76±0.01 A°, and c = 25.62±0.01 A°. The 1-5 derived composition for this struture via the 2-7 phase

corresponds to $Sm_7(Fe,Ti)_{30}$. The semi-soft phase component is reported as $Sm(Fe,Ti)_2$ tetragonal phase distorted from cubic phase.

To obtain this high $_iH_c$ Sm-Fe-Ti phase a certain range of Sm at.% and Ti/Fe ratio in the film are required and also a proper crystallization temperature is very important. It was shown that the film composition corresponding to the high $_iH_c$ Sm-Fe-Ti phase should contain 17 to 22 at.% of Sm and a Ti/Fe ratio of 0.07 to 0.14. In addition to the composition of the target sputtered, the experiment indicated that the substrate temperature used during the subsequent crystallization is critical for obtaining the required film composition. It was shown that the Sm at.% incorporated into the films is a strong function of the substrate temperature used during the sputter deposition and subsequent crystallization whereas the Ti/Fe ratio is comparatively fixable.

In addition the magnetic properties of the high $_iH_c$ Sm-Fe-Ti system containing small amounts of Al, V, and Zr have been studied. The addition of 2.3 to 4.5 at.% Al helped to stabilize the samples into a more nearly single phase form. The high $_iH_c$ values for Al concentration less than 4 at.% did not fall below 30 KOe for proper preparation conditions.

Since these high coercive force samples have been made by crystallizing films originally deposited in an amorphous state, it is not expected that the films will be strongly textured. It is thus not possible to directly saturate the samples even with fields of 90 KOe. The expected saturation magnetization $4\pi M_s$ for the high $_iH_c$ Sm-Fe-Ti phase based on the fitted hexagonal cell is 11.8 KG. It is estimated that the anisotropy field based on magnetization measurement up to 90 KOe in-plane and out of plane is 230 to 300 KOe.

Films that have been directly crystallized onto heated substrates exhibited several different crystal phases as a function of temperature and composition. Films that were directly crystallized onto heated substrate at approximately 350° C have been made which exhibit only one dominant diffraction line (200) of the hexagonal 1-5 phase. Such films exhibit no reflection with the c-axis components out of the film plane. These films are far easier to magnetize in the film plane than out of the film plane. These results are consistent with the easy axes of the crystallites being aligned onto the film plane. Film synthesized onto substrates heated to between 350° and 450° C exhibit predominantly a $Sm(Fe,Ti)_{12}$ structure. Films made at substrate temperature of 450° C exhibit predominantly the (300) reflection of the $Sm_2(Fe,Ti)_{17}$ structure. Such films are far easier to magnetize out of the film plane than in the film plane. This is expected because $Sm_2(Fe,Ti)_{17}$ is an easy plane material. The x-ray

pattern indicates that the c-axes, which are hard axes in this case, lie in the film plane. The higher substrate temperature used for samples of the 2-17 type acted to deplete the film in Sm and shift the structure from a 1-5 to a 2-17 type. The possible occurrence of the high $_iH_c$ Sm-Fe-Ti phase in directly crystallized film is also investigated. So far the high $_iH_c$ Sm-Fe-Ti phase has only been observed in samples that were first deposited in an amorphous form and then subsequently crystallized within a temperature range of 450° to 510° C.

We reported[10,11] for the first time the occurrence of the high $_iH_c$ Sm-Fe-Ti phase in sputtered film deposited in an amorphous state and then crystallized. This high $_iH_c$ Sm-Fe-Ti phase forms at a nominal composition of $Sm_{20}Fe_{70}Ti_{10}$. Following our results, Schnitzke *et al.*[65] reported the same high $_iH_c$ Sm-Fe-Ti phase in the bulk form for the same composition range as we reported. Their material preperation involves mechanical alloying and additional annealing. They reported room temperature intrinsic coercivities up to 50.3 KOe for the mechanically alloyed sample. Crystallization of rapidly quenched and partially amorphous ribbons leads to a two-phase material with a considerable amount of high $_iH_c$ phase but with $SmFe_2$ as a majority phase. This new phase has a Curie temperature of 380° C and an estimated saturation flux of 6 to 7 KG.

In conclusion, we observed five different magnetic phases in the Fe rich Sm-Fe-Ti sputtered films prepared under different sets of sputtering conditions. They were: $Sm_2(Fe,Ti)_{17}$, $(Sm+Ti)Fe_5$, $Sm(Fe,Ti)_{12}$, $Sm(Fe,Ti)_2$, and the high ${}_iH_c$ Sm-Fe-Ti phase. We have demonstrated the means of fabricating film magnets with special anisotropies in the Sm-Fe-Ti systems. All these films were chemically stable and have not shown any degradation for several years.

TABLE 1

Substance	Magnetization M_s (emu/cm^3) 0°K	Room temperature	$4\pi M_s$ (KG) 0°K	Curie Temperature (Kelvin)
Fe	1740	1707	21.854	1043
Co	1446	1400	18.162	1388
Ni	510	485	6.406	627
Gd	2060	---	25.874	292

TABLE 2

Substance	Electronic structure	Number of Bohr magnetons per Formula Unit (0°K)
Fe	$(Ar)3d^6 4s^2$	2.219
Co	$(Ar)3d^7 4s^2$	1.715
Ni	$(Ar)3d^8 4s^2$	0.604
Gd	$(Xe)4f^7 5d6s^2$	7.630
Nd	$(Xe)4f^4 6s^2$	$3.5(Nd^{+3})$
Sm	$(Xe)4f^6 6s^2$	$1.5(Sm^{+3})$

TABLE 3

Compound	Structure type	Symmetry	Space Group	TM
$RE-TM_2$	$MgCu_2$	Cubic	Fd3m	Ni,Co,Fe
	$MgZn_2$	Hexagonal	$P6_3/mmc$	Mn
$RE-TM_3$	$PuNi_3$	Rhombohedral	R_3m	Ni,Co,Fe
	$CeNi_3$	Hexagonal	$P6_3/mmc$	Ni,Co
RE_2-TM_7	Ce_2Ni_7	Hexagonal	$P6_3/mmc$	Ni,Co
	$GdCo_7$	Rhombohedral	R_3m	Ni,Co
RE_6-TM_{23}	Th_6Mn_{23}	Tetragonal	Fm3m	Fe,Mn
$RE-TM_5$	$CaCu_5$	Hexagonal	$P6_3/mmc$	Co,Ni Zn,Cu
RE_2-TM_{17}	Th_2Ni_{17}	Hexagonal	$P6_3/mmc$	Ni,Fe
	Th_2Zn_{17}	Rhombohedral	R_3m	Ni,Co,Fe
$RE-TM_{12}$	$ThMn_{12}$	Tetragonal	I_4/mmc	Mn

TABLE 4

Compound	Crystal symmetry	Structure type	Lattice constants(A°)	T_c (°K)
$SmFe_2$	Cubic	$MgCu_2$	a = 7.417	675
$SmFe_3$	Rhombohedral	$PuNi_3$	a = 5.187 c =24.910	650
Sm_2Fe_{17}	Rhombohedral	Th_2Zn_{17}	a = 8.570 c =12.440	385
(Sm+Ti)Fe_8	Hexagonal	$CaCu_5$	a = 4.84 c = 4.34	630
$Sm(Ti,Fe)_{12}$	Tetragonal	$ThMn_{12}$	a = 8.579 c = 4.799	573

TABLE 5

Sample#	Composition at. %			$_i H_c$ (KOe) 293°K	$M_r/M_{(\ldots)}$	$M_{-\ldots}/M_r$
	Sm	Ti	Fe			
F572-9	21.10	8.40	70.50	9		0.08
F573-42	12.32	9.14	78.54	11		0.18
F556-12	19.29	8.67	72.04	18		0.49
F556-2	17.96	9.42	72.62	23	0.769	0.50
F572-31	20.71	7.38	71.91	30	0.833	0.61
F572-62	17.78	11.31	70.91	31.75	0.851	0.64
F572-32	18.90	8.43	72.68	37.75	0.887	0.78

TABLE 6

Sample#	$_i H_c$ (KOe) 293°K	Composition at. % Sm	Ti	Fe	Ti/Fe
F571-2	0.7	13.32	7.66	79.02	0.097
F551-12	2.5	20.67	8.85	70.48	0.126
F551-14	3.5	22.93	8.19	68.88	0.119
F551-11	6.0	21.74	8.50	69.76	0.122
F572-9	9.0	21.10	8.40	70.50	0.119
F573-42	11.0	12.32	9.14	78.54	0.116
F574-63	16.0	16.41	7.79	75.80	0.103
F556-12	18.0	19.29	8.67	72.04	0.120
F556-2	23.0	17.96	9.42	72.62	0.130
F572-31	30.0	20.71	7.38	71.91	0.103
F572-62	31.75	17.78	11.31	70.91	0.159
F554-3	32.5	18.68	8.52	72.80	0.117
F573-32	37.75	18.90	8.43	72.68	0.116

TABLE 7

Sample#	Temp.	Time	(a) Composition(at.%) Sm	Fe	Ti	Ti/Fe	4πM	⊥ Hc
F648	440°C	135M	16.89	75.82	7.29	0.096	6.7KG	1KOe
F641	475	135	17.94	73.31	8.75	0.119	7.2	>18
F647	510	135	14.97	77.17	7.85	0.102	5.3	>18
				(b)				
F510	450	60	22.49	72.42	5.09	0.070	7.3	9
F503	510	60	20.49	74.32	5.18	0.069	6.5	>18
F504	560	60	4.30	88.38	7.32	0.083	7.6	1.5
F505	600	60	4.08	89.28	6.64	0.074	8.2	0.5

TABLE 8

(a)								
Sample#	Temp.	Time	Composition(at.%) Sm	Fe	Ti	Ti/Fe	4πM	$_iH_c$
F644	475°C	90M	20.77	71.74	7.49	0.104	6.4KG	>18KOe
F642	475	135	19.94	71.74	8.06	0.112	6.2	>18
F645	475	180	19.17	72.99	7.84	0.102	5.7	>18
(b)								
F503	510	60	20.49	74.32	5.18	0.067	6.5	>18
F507	510	210	20.73	73.92	5.35	0.072	6.3	>18

(c)	Before etching			After etching		
	Sm	Fe	Ti	Sm	Fe	Ti
F507	20.73	72.42	5.09	22.91	67.38	9.71
F508	19.98	74.32	5.18	18.98	70.04	10.98
F510	21.75	69.95	8.30	21.42	72.03	6.54
F504	3.91	89.01	7.08	9.17	81.89	8.94

TABLE 9

2-7 RHOMBOHEDRAL
a = 5.08 A°, c = 38.41 A°

$(2\theta)_{obs.}$	$(2\theta)_{cal.}$	$(2\theta)_{cal.}-(2\theta)_{obs.}$	h	k	l	I
27.94	27.849	-0.090	0	0	12	25
35.26	35.307	0.047	1	1	0	29
35.98	36.018	0.039	1	1	3	26
36.70	36.606	-0.094	1	0	13	34
41.32	41.330	0.001	1	1	9	32
41.32	41.276	-0.044	2	0	2	32
42.40	42.320	-0.080	0	0	18	30
45.04	45.071	0.030	0	1	17	20
47.65	47.599	-0.051	0	2	10	16
55.40	55.417	0.017	1	2	2	18
56.00	56.086	0.086	2	1	4	33
56.78	56.712	-0.067	0	2	16	28
57.62	57.541	-0.079	0	0	24	37
59.03	59.123	0.093	0	1	23	24
61.73	61.739	0.009	1	2	11	29
65.21	65.213	0.003	0	3	6	32
65.21	65.213	0.003	3	0	6	32
66.65	66.737	0.087	0	1	26	39

TABLE 10

1-12 TETRAGONAL

a = 8.56 A°, c = 4.79 A°

$(2\theta)_{obs.}$	$(2\theta)_{cal.}$	$(2\theta)_{cal.}-(2\theta)_{obs.}$	h	k	l	I
27.94	27.933	-0.07488	2	0	1	25
36.70	36.628	-0.0719	3	0	1	34
42.40	42.460	0.0634	3	2	1	30
47.65	47.704	0.0537	4	1	1	16
57.62	57.689	0.0686	0	0	3	37
62.96	63.028	0.0686	2	1	3	34
66.65	66.569	-0.0813	5	3	1	39
68.21	68.158	-0.0521	5	1	2	22
72.44	72.514	0.0736	6	2	1	22
77.24	77.320	0.0800	6	3	1	30

TABLE11

2-17 RHOMBOHEDRAL

a = 8.58 A°, c = 12.50 A°

$(2\theta)_{obs.}$	$(2\theta)_{cal.}$	$(2\theta)_{cal.}-(2\theta)_{obs.}$	h	k	l	I
27.94	27.914	-0.0259	2	0	2	25
42.40	42.421	0.0206	3	0	3	30
43.66	43.600	0.0592	2	0	5	30
47.65	47.644	-0.0593	2	2	3	16
52.58	52.673	0.0926	1	0	7	8
56.78	56.725	-0.0545	1	4	0	28
57.62	57.683	0.0632	4	0	4	37
62.96	62.930	-0.0304	0	5	1	34
64.76	64.661	-0.0988	2	0	8	21
65.21	65.185	-0.0253	3	3	0	32
72.44	72.341	-0.0986	1	5	2	22
76.94	76.923	-0.0169	0	6	0	30
76.94	76.923	-0.0169	6	0	0	30
77.24	77.321	0.0805	3	2	7	30

TABLE 12

Gd_2Co_7-type RHOMBOHEDRAL

a = 5.09 A°, c = 36.39 A°

$(2\theta)_{obs.}$	$(2\theta)_{cal.}$	$(2\theta)_{cal.}-(2\theta)_{obs.}$	h	k	l	I
26.53	26.489	-0.041	1	0	7	32
31.96	31.862	-0.098	1	0	10	17
35.26	35.235	-0.025	1	1	0	29
35.98	36.028	0.049	1	1	3	26
38.26	38.233	0.063	1	1	6	25
41.32	41.225	-0.095	2	0	2	32
52.10	52.017	-0.083	1	0	19	12
52.10	52.036	-0.064	1	1	15	12
56.00	56.071	0.071	2	1	4	33
60.14	60.215	0.076	2	0	17	25
61.04	61.064	0.024	0	0	24	38
61.04	61.125	0.085	2	1	10	38
65.21	65.285	0.076	3	0	6	32
66.65	66.592	-0.058	2	0	20	39
72.44	72.505	0.065	1	1	24	22

TABLE 13

Gd_2Co_7-type HEXAGONAL

a = 4.99 A°, c = 36.40 A°

$(2\theta)_{obs.}$	$(2\theta)_{cal.}$	$(2\theta)_{cal.}-(2\theta)_{obs.}$	h	k	l	I
30.28	30.241	-0.039	1	0	9	41
31.96	31.936	-0.024	0	0	13	17
32.08	32.125	0.045	1	0	10	9
34.45	34.467	0.017	0	0	14	100
35.98	36.053	0.073	1	1	1	26
35.98	35.965	-0.015	1	1	0	26
36.70	36.745	0.045	1	1	3	34
38.26	38.270	0.010	1	0	13	25
39.64	39.581	-0.059	0	0	16	42
40.00	40.050	0.050	1	1	7	50
41.32	41.231	-0.088	1	1	8	32
42.40	42.458	0.058	2	0	3	30
43.03	42.987	-0.042	2	0	4	45
43.66	43.661	-0.001	2	0	5	30
45.04	44.994	-0.046	1	0	16	20
47.65	47.679	0.029	2	0	9	16
52.10	52.183	0.083	1	0	19	12
52.58	52.565	-0.015	1	1	15	8
55.40	55.492	0.092	0	0	22	18
56.78	56.829	0.049	2	1	3	28
60.14	60.140	0.000	2	1	8	25
61.04	61.045	0.052	0	0	24	38
62.96	62.893	-0.066	2	0	18	34
64.76	64.711	0.011	2	1	12	21
64.76	64.708	-0.051	3	0	1	21
65.21	65.129	-0.081	1	0	24	32
65.21	65.162	-0.050	3	0	3	32
66.65	66.680	0.030	3	0	6	39
68.21	66.235	0.025	3	0	8	22
76.94	76.903	-0.037	3	0	15	30

TABLE 14

2-7 HEXAGONAL
a = 5.05 A°, c = 38.35 A°

$(2\theta)_{obs.}$	$(2\theta)_{cal.}$	$(2\theta)_{cal.}-(2\theta)_{obs.}$	h	k	l	I
25.51	25.529	0.019	0	0	11	22
27.94	27.894	-0.046	0	0	12	25
29.32	29.238	-0.083	1	0	9	33
30.28	30.272	-0.078	0	0	13	41
36.70	36.717	0.017	1	0	13	34
36.70	36.778	0.078	1	1	4	34
38.26	38.295	0.035	1	1	6	25
40.00	39.931	-0.069	0	0	17	50
40.27	40.338	0.068	1	1	8	55
41.32	41.321	0.001	2	0	1	32
41.32	41.251	-0.069	2	0	0	32
42.40	42.390	-0.010	0	0	18	30
42.40	42.360	-0.040	2	0	4	30
43.03	42.996	-0.034	1	0	16	45
43.03	42.974	-0.056	2	0	5	45
43.66	43.715	0.055	2	0	6	30
46.69	46.648	-0.042	2	0	9	20
52.10	52.033	-0.068	1	0	20	12
52.10	52.014	-0.086	2	0	13	12
52.58	52.604	0.024	1	1	16	8
56.00	56.051	0.051	2	1	3	33
56.78	56.809	0.029	1	0	22	28
57.62	57.639	0.019	0	0	24	37
57.62	57.545	-0.076	2	1	6	37
59.03	59.065	0.035	2	1	8	24
59.36	59.261	-0.099	1	0	23	32
61.04	60.986	-0.054	2	1	10	38
61.73	61.757	0.027	1	0	24	29
62.96	62.963	0.003	0	0	26	34
66.65	66.671	0.021	2	0	21	39
69.02	68.952	-0.068	2	1	16	18
76.94	76.912	-0.028	2	2	6	30

TABLE 15

1-5 HEXAGONAL

a = 4.78 A°, c = 4.37 A°

$(2\theta)_{obs.}$	$(2\theta)_{cal.}$	$(2\theta)_{cal.}-(2\theta)_{obs.}$	h	k	l	I
41.32	41.285	-0.036	0	0	2	32
43.03	43.104	0.074	1	1	1	45
43.66	43.697	0.037	2	0	0	30
59.03	58.985	-0.045	2	1	0	24
61.73	61.677	-0.053	2	0	2	29
62.96	63.056	0.096	2	1	1	34
68.21	68.192	-0.018	1	0	3	22

TABLE 16

1-3 RHOMBOHEDRAL

a = 5.06 A°, c = 24.91 A°

$(2\theta)_{obs.}$	$(2\theta)_{cal.}$	$(2\theta)_{cal.}-(2\theta)_{obs.}$	h	k	l	I
35.26	35.342	0.0823	0	1	8	29
41.32	41.332	0.012	0	2	1	32
43.66	43.582	-0.078	0	0	12	30
45.04	45.040	0.000	0	1	11	20
52.10	52.067	-0.033	1	0	13	12
56.00	55.960	-0.040	1	2	2	33
57.62	57.534	-0.086	2	1	4	37
61.73	61.730	0.000	2	1	7	29
64.76	64.745	-0.012	0	3	3	21
64.76	64.748	-0.012	3	0	3	21

TABLE 17

1-3 HEXAGONAL

a = 5.059 A°, c = 24.88 A°

$(2\theta)_{obs.}$	$(2\theta)_{cal.}$	$(2\theta)_{cal.}-(2\theta)_{obs.}$	h	k	l	I
35.26	35.364	0.010	1	0	8	29
35.98	36.070	0.090	0	0	10	26
40.00	39.950	-0.050	1	1	5	50
41.32	41.340	0.021	2	0	1	32
43.66	43.619	-0.041	0	0	12	30
45.04	45.072	0.032	1	0	11	20
52.10	52.106	0.006	1	0	13	12
55.40	55.343	-0.058	2	1	0	18
56.00	55.973	-0.027	2	1	2	33
57.62	57.549	-0.071	2	1	4	37
59.36	59.387	0.027	0	0	16	32
60.14	60.117	-0.024	2	1	6	25
61.730	61.750	0.020	2	1	7	29
64.76	64.764	0.004	3	0	3	21
66.65	66.691	0.042	3	0	5	39

TABLE 18

TETRAGONAL

$a = 8.39\ A^{\circ}$, $c = 12.42\ A^{\circ}$

$(2\theta)_{obs.}$	$(2\theta)_{cal.}$	$(2\theta)_{cal.}-(2\theta)_{obs.}$	h	k	l	I
25.51	25.605	0.095	2	0	2	22
30.28	30.307	0.027	2	0	3	41
31.96	31.975	0.015	3	0	0	17
32.08	32.170	0.090	2	1	3	9
34.45	34.540	0.090	3	1	1	100
35.26	35.164	-0.096	3	0	2	29
35.98	35.955	-0.025	2	0	4	26
40.27	40.343	0.073	3	1	3	55
41.32	41.403	0.083	3	2	2	32
43.03	43.091	0.061	4	0	0	45
43.66	43.692	0.032	0	0	6	30
43.66	43.665	0.005	2	1	5	30
43.66	43.732	0.072	4	0	1	30
45.04	45.073	0.033	1	0	6	20
45.04	45.112	0.072	4	1	1	20
47.65	47.715	0.065	2	2	5	16
52.58	52.614	0.034	4	0	4	8
56.78	56.785	0.005	4	3	2	28
56.78	56.785	0.005	5	0	2	28
59.36	59.382	0.022	4	3	3	32
59.36	59.382	0.022	5	0	3	32
59.36	59.262	-0.098	5	2	0	32
61.73	61.709	-0.021	1	1	8	29
62.96	62.969	0.009	3	1	7	34
62.96	63.042	0.082	4	0	6	34
62.96	62.905	-0.055	4	3	4	34
62.96	62.905	-0.055	5	0	4	34
64.76	64.734	-0.027	5	3	0	21
65.21	65.189	-0.020	3	3	6	32
65.21	65.219	0.009	5	3	1	32
66.65	66.668	0.018	5	3	2	39
68.21	68.112	-0.098	2	2	8	22
69.02	69.048	0.028	5	3	3	18
72.44	72.446	0.002	4	3	6	22
72.44	72.446	0.002	5	0	6	22
72.44	72.475	0.035	5	4	1	22
76.94	76.988	0.048	3	0	9	30
77.24	77.228	-0.012	4	1	8	30

TABLE 19

(a)							(b)		
High H_c phase							semi-soft phase		
d(A°)	d'	d-d'	h	k	l	I	d'	d-d'	h k l
3.191	3.200	-0.009	0	0	8	w			
3.044	3.046	-0.003	2	0	5	w			
2.949	2.948	0.001	1	0	8	s			
2.788	2.796	-0.008	2	1	2	w			
2.632	2.631	0.001	2	0	7	s			
2.601						vs	2.609	-0.008	2 2 0
2.494	2.500	-0.006	2	1	5	wb			
2.447	2.445	0.002	2	0	8	w			
2.351	2.350	0.001	3	0	4	wb			
2.272	2.275	-0.003	2	0	9	s			
2.252	2.255	-0.003	2	1	7	vs			
2.238						vs	2.226	0.012	3 1 1
2.183	2.180	0.003	2	2	1	w			
2.183	2.188	-0.005	2	2	0	w			
2.130	2.133	-0.003	0	0	12	w			
2.130	2.135	-0.004	2	1	8	w			
2.100	2.102	-0.002	3	1	0	vs	2.131	-0.031	2 2 2
2.072	2.071	0.001	2	2	4	s			
2.072	2.075	-0.003	3	1	2	s			
2.011	2.012	-0.001	2	2	5	wb			
1.944	1.947	-0.003	2	2	6	w			
1.944	1.945	-0.001	3	1	5	w			
1.907	1.909	-0.002	2	1	10	w			
1.641	1.641	0.000	4	1	2	w			
1.556	1.556	0.000	2	0	15	w			
1.517	1.516	0.001	5	0	0	w	1.507	0.010	4 2 2
1.475	1.477	-0.002	1	0	17	w			
1.475	1.474	0.001	2	0	16	w			
1.475	1.475	0.000	5	0	4	w			
1.430						w	1.421	0.009	3 3 3
1.402	1.403	-0.001	2	2	14	s			
1.402	1.400	0.002	5	0	7	s			
1.402	1.403	-0.001	3	3	5	s			
1.304	1.303	0.001	3	2	13	s	1.305	-0.001	4 4 0
1.304	1.304	0.000	5	0	10	s			
1.238	1.239	-0.001	3	0	18	w			
1.238	1.239	-0.001	6	0	4	w			
1.234	1.233	0.001	4	3	3	w			
(c)									
2.601						vs	2.605	0.003	0 0 3
2.238						vs	2.241	0.003	3 1 0
2.100						vs	2.099	0.002	2 0 3
1.430						w	1.430	0.000	2 0 5
1.304						vw	1.303	0.001	3 0 5

TABLE 20

Sample#	$_iH_c$ (KOe) 293°K	4πM(KG)	Composition at.%			
			Sm	Fe	Ti	Al
F683-32	18	5.78	12.71	73.91	7.70	5.70
F689-32	18.5	6.22	12.85	75.13	7.85	4.16
F690-12	23.06	5.76	13.16	73.92	8.26	4.51
F690-52	27.31	6.32	13.31	74.32	8.84	3.53
F689-52	20.65	7.10	14.09	74.42	8.51	2.96
F680-32	28.12	6.05	15.72	72.82	9.13	2.31
F680-12	27.35	5.43	15.81	70.49	9.16	4.18
F680-52	33.34	7.12	16.34	70.65	9.40	3.61
F677-21	32.16	6.37	17.42	70.17	9.44	2.96
F678-31	31.00	6.00	17.79	70.40	9.05	2.76
F678-12	30.22	6.24	17.92	69.68	9.23	3.16
F678-11	30.90	5.23	18.11	69.90	9.04	2.95

TABLE 21

Sample#	$_i H_c$ (KOe) 293°K	Composition at.%			
		Sm	Fe	Ti	Al
F691-12	10.55	12.55	75.69	7.98	3.77
F690-52	27.31	13.31	74.32	8.84	3.53
F691-41	>18	13.61	74.26	8.73	3.39
F689-52	22.40	14.09	74.42	8.51	2.96
F692-71	>18	15.17	72.70	9.02	3.11
F677-31	>18	16.27	70.77	10.03	2.93
F680-52	33.34	16.34	70.65	9.40	3.61
F677-21	32.16	17.42	70.17	9.43	2.96
F678-42	>18	17.61	69.59	9.56	3.23
F678-12	30.22	17.92	69.68	9.23	3.16
F678-11	31.00	18.11	69.90	9.04	2.95

TABLE 22

Sample#	$_i H_c$ (KOe) 293°K	Composition at.%			
		Sm	Fe	Ti	Al
F680-32	30.00	15.72	72.82	9.14	2.31
F677-22	>18	16.16	72.16	9.34	2.43
F677-12	>18	15.64	72.72	8.86	2.77
F677-21	32.16	17.42	70.17	9.44	2.96
F678-12	33.00	17.92	69.68	9.23	3.16
F680-52	33.34	16.34	70.65	9.41	3.61
F677-11	>18	17.45	69.42	9.34	3.73
F680-12	27.25	15.81	70.49	9.16	4.18
F698-11	18.50	16.02	69.84	9.29	5.15
F698-31	16.50	14.00	70.63	8.91	6.43

TABLE 23

Sample#	Sub.Cry.Temp(°C)	Composition at.%			
		Sm	Fe	Ti	Al
F682	25	24.81	64.03	7.09	4.06
F707	410	22.57	67.68	7.18	2.55
F688	450	21.26	67.17	6.05	5.52
F680	490	16.34	70.65	9.40	3.61
F684	510	12.06	74.79	7.98	5.16
F685	530	9.06	77.80	7.45	5.64
F686	560	3.53	84.59	8.40	3.82

TABLE 24

Sample#	$_iH_c$ (KOe) 293° K	Composition at.%				
		Sm	Fe	Ti	V	Ti/Fe
F695-31	6.0	9.30	75.79	11.06	3.86	0.146
F694-12	9.0	8.57	74.69	12.26	4.48	0.159
F695-12	12.5	12.75	73.84	9.93	3.48	0.134
F694-51	>18	12.28	73.05	10.16	3.71	0.139
F695-11	>18	15.11	70.39	10.79	3.70	0.153

TABLE 25

Sample#	$_iH_c$ (KOe) 293° K	Composition at.%				
		Sm	Fe	Ti	Zr	Ti/Fe
F710-11	2.50	13.28	76.63	7.83	2.22	0.102
F710-61	6.50	14.77	75.41	7.39	2.44	0.098
F712-11	12.00	13.66	74.84	8.70	2.79	0.116
F712-51	16.00	14.46	74.46	8.35	2.72	0.112
F714-62	18.00	14.22	74.57	8.71	2.50	0.117
F713-52	>18	16.73	72.21	8.42	2.64	0.117
F713-32	>18	16.40	71.52	9.47	2.62	0.132
F714-32	>18	15.18	73.19	8.71	2.92	0.119
F710-31	>18	17.55	71.80	8.07	2.58	0.112

TABLE 26

Substrate Temerature(°C)	Film Composition at.%			Ti/Fe atomic ratio	$_{i}H_{c}$ (KOe)
	Sm	Fe	Ti		
410	11.64	75.96	12.40	0.163	0.5
410	19.01	69.83	11.15	0.159	1.0
440	8.03	79.21	12.76	0.161	4.5
470	7.45	79.80	12.75	0.159	5.2
480	8.02	79.22	12.76	0.161	4.0
480	7.52	80.21	12.28	0.153	5.5
480	7.24	80.44	12.33	0.157	6.2
495	7.36	79.73	12.90	0.162	5.3

Fig. 3.1

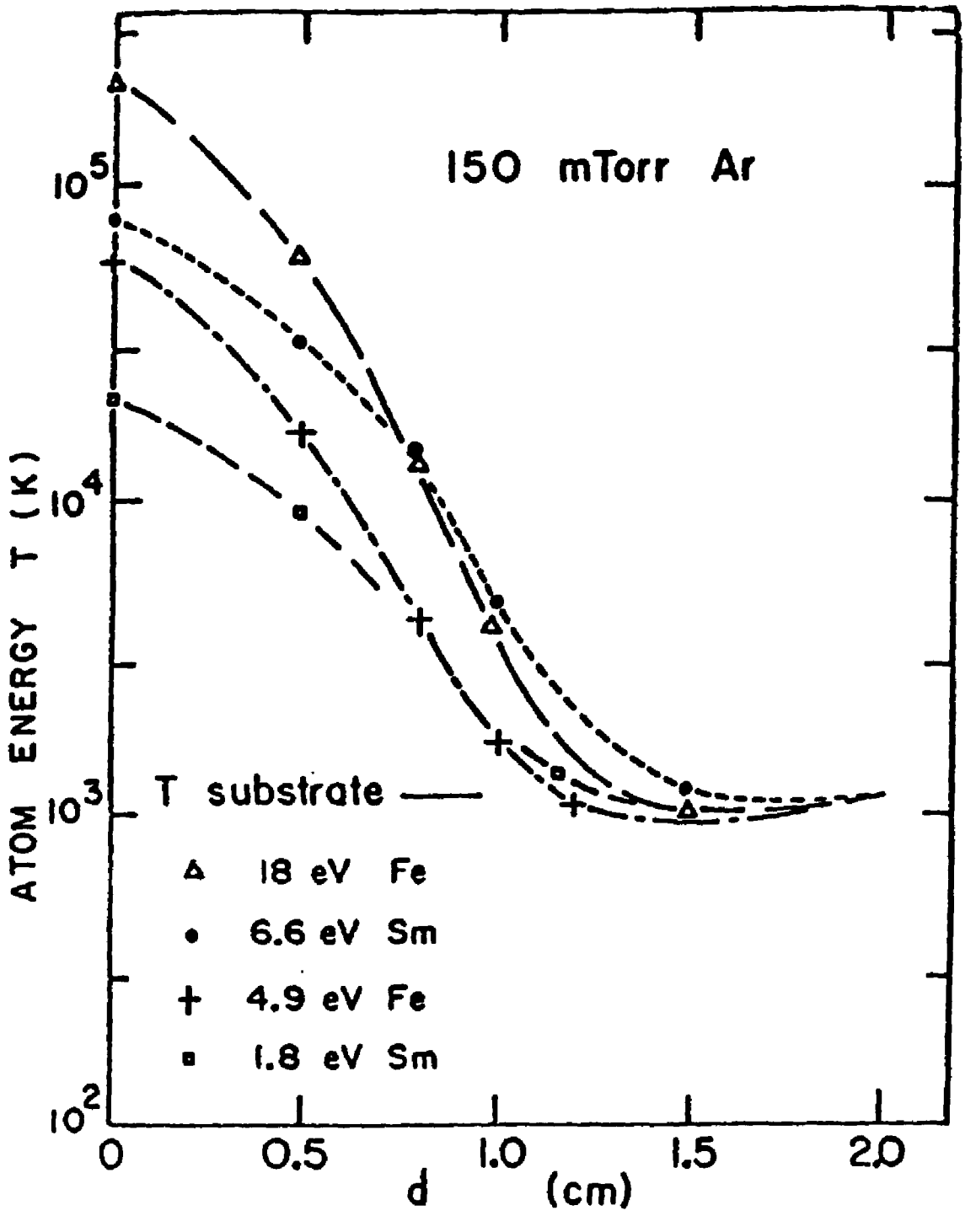
150 mTorr Ar
ATOM ENERGY T (K)
10^5
10^4
10^3
10^2
T substrate
18 eV Fe
6.6 eV Sm
4.9 eV Fe
1.8 eV Sm
0
0.5
1.0
1.5
2.0
d (cm)

Fig. 3.2

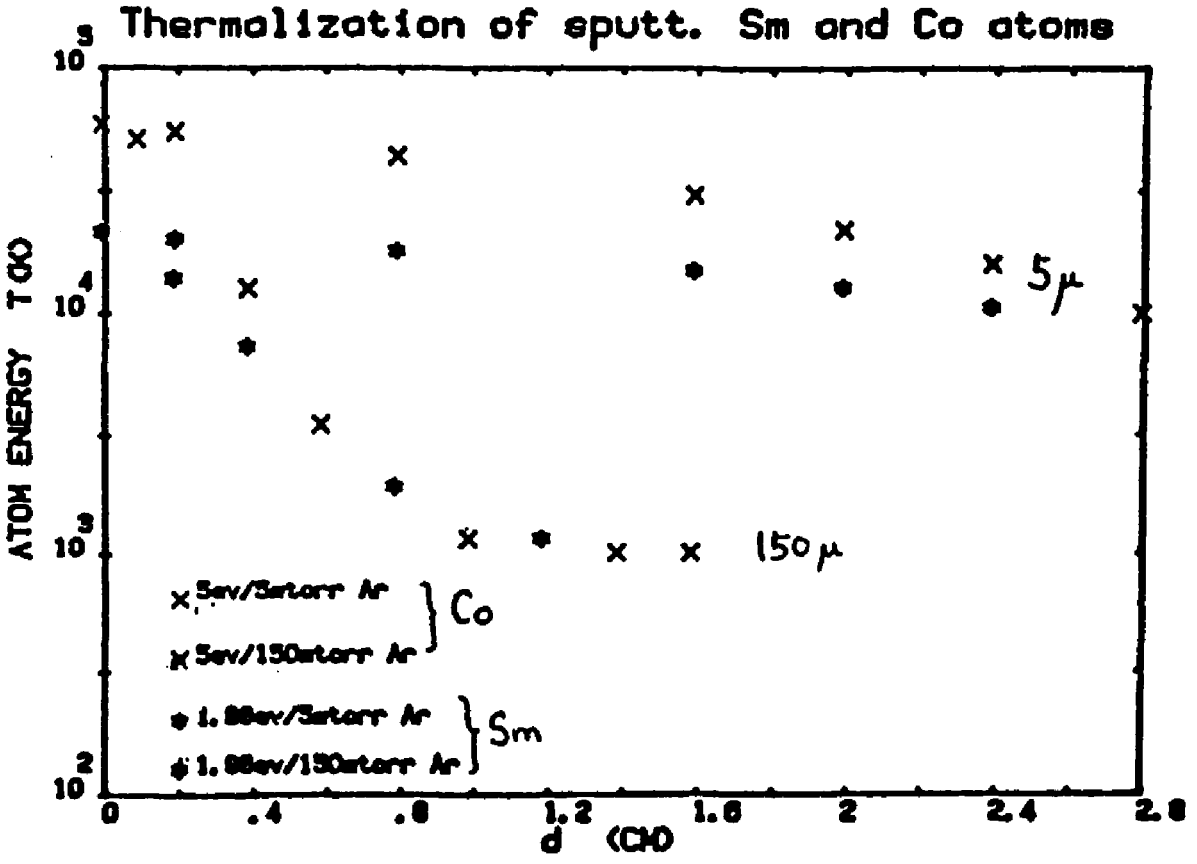
Thermalization of sputt. Sm and Co atoms
ATOM ENERGY T(K)
10^5
10^4
10^3
10^2
0
.4
.8
1.2
1.6
2
2.4
2.8
d (CM)
5μ
150μ
5ev/3xtorr Ar
5ev/150xtorr Ar
Co
1.8ev/3xtorr Ar
1.8ev/150xtorr Ar
Sm

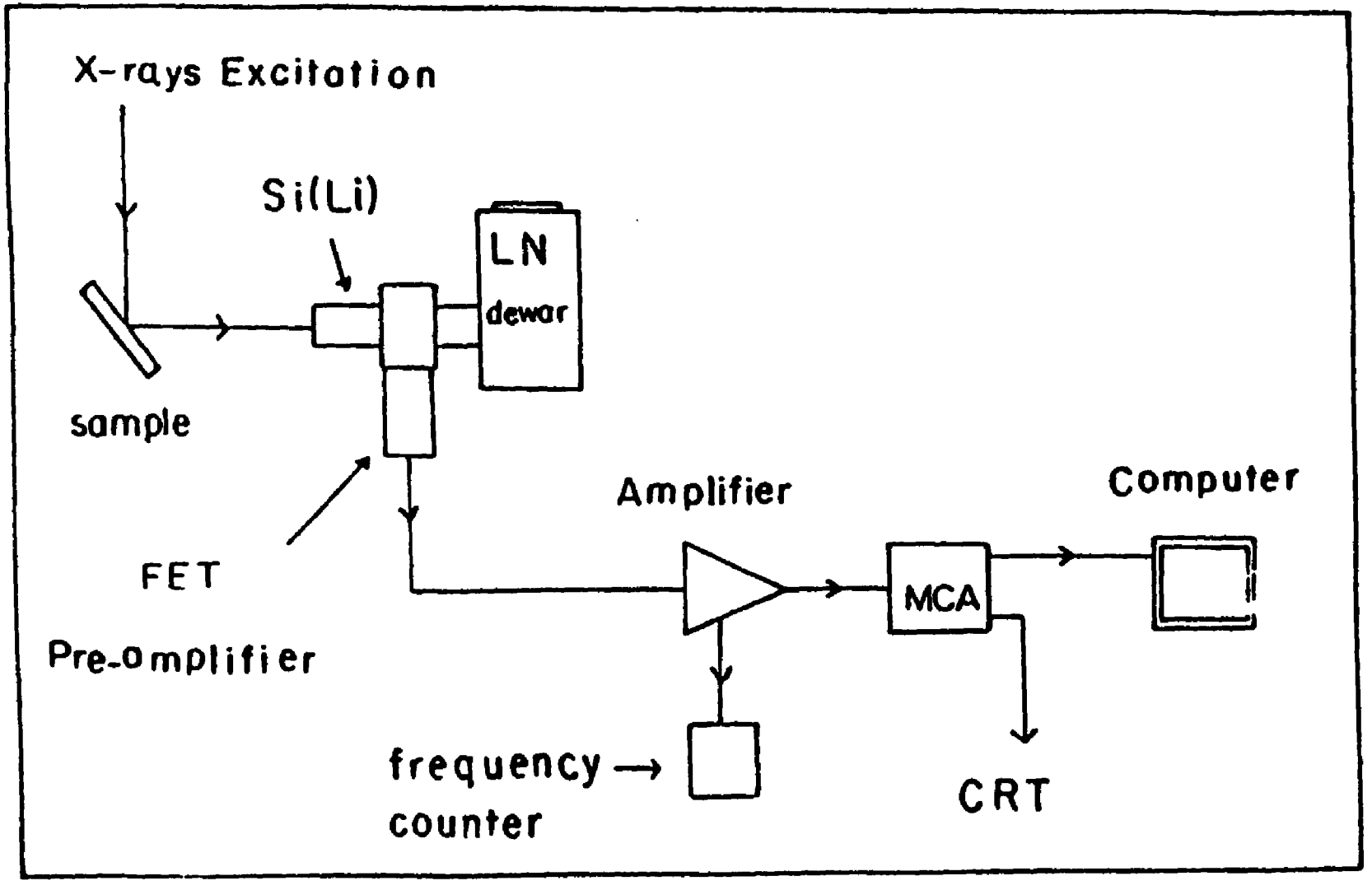
X-rays Excitation
Si(Li)
LN
dewar
sample
FET
Pre-amplifier
Amplifier
Computer
MCA
frequency
counter
CRT

Fig. 3.3

Fig. 4.1

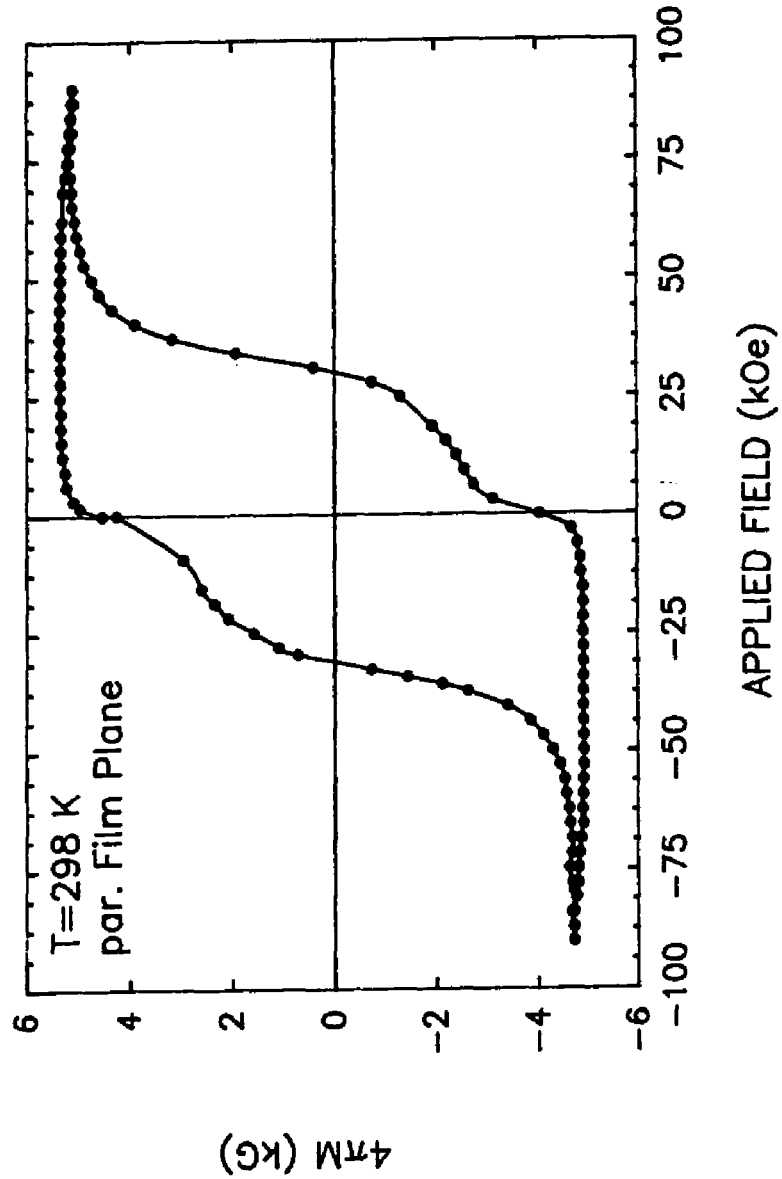
T=298 K
par. Film Plane
4πM (kG)
APPLIED FIELD (kOe)
6
4
2
0
-2
-4
-6
100
75
50
25
0
-25
-50
-75
-100

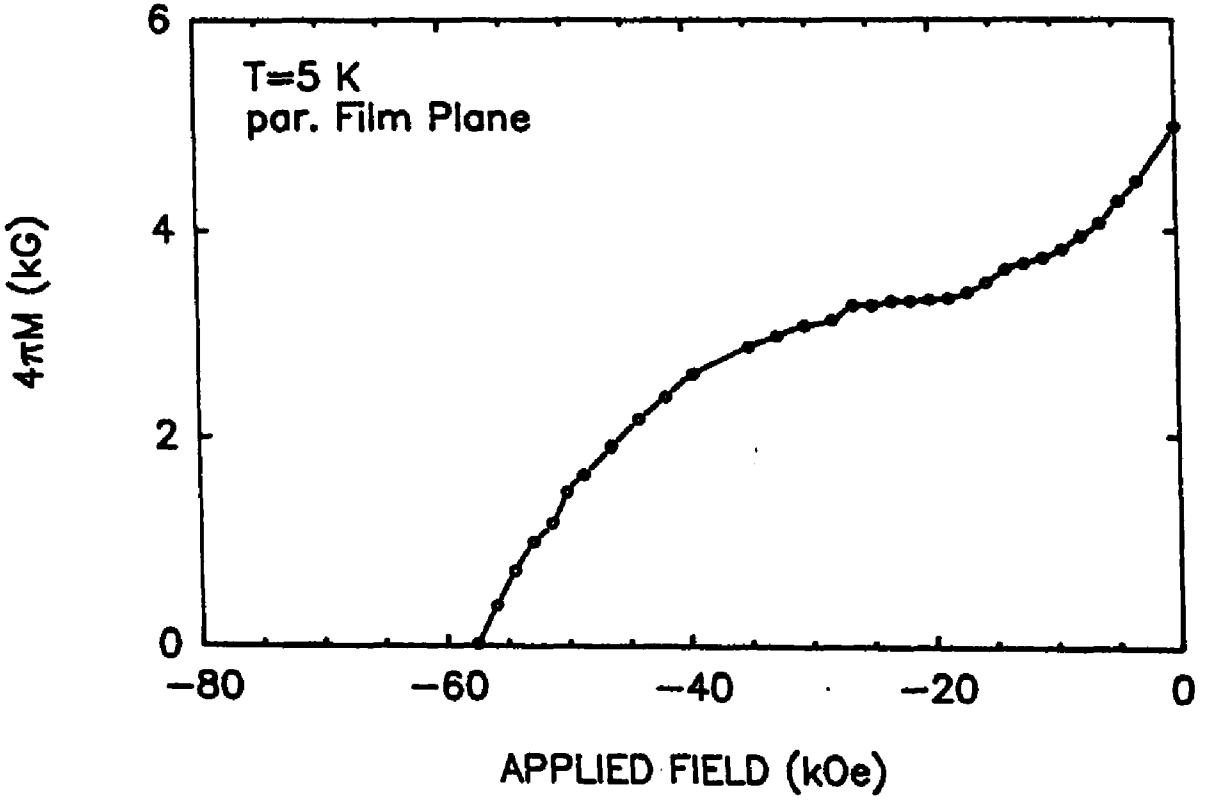

Fig. 4.2

Fig. 4.3

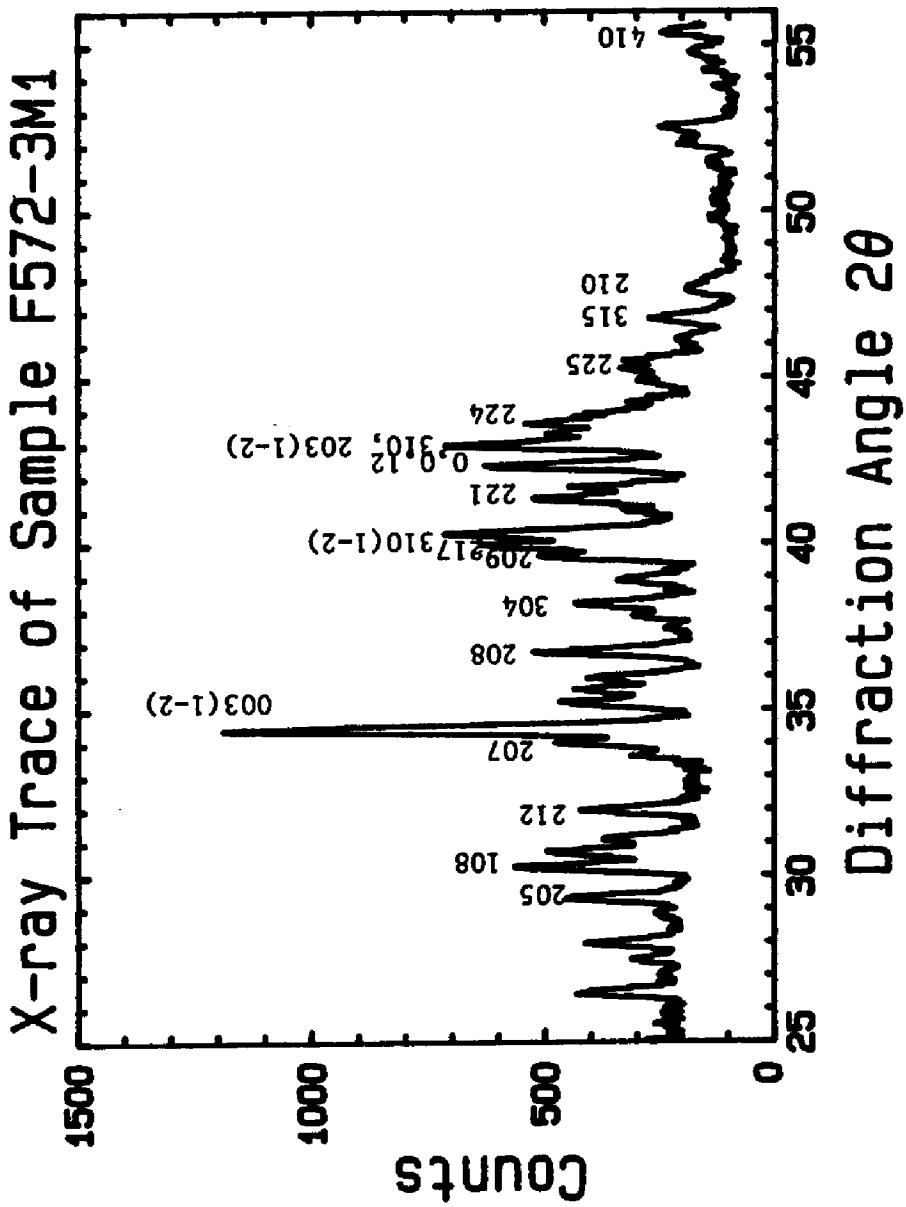
X-ray Trace of Sample F572-3M1
Counts
Diffraction Angle 2θ
1500
1000
500
0
25
30
35
40
45
50
55
410
210
315
225
224
0,9,12; 203(1-2)
221
209,17 310(1-2)
304
208
003(1-2)
207
212
108
205

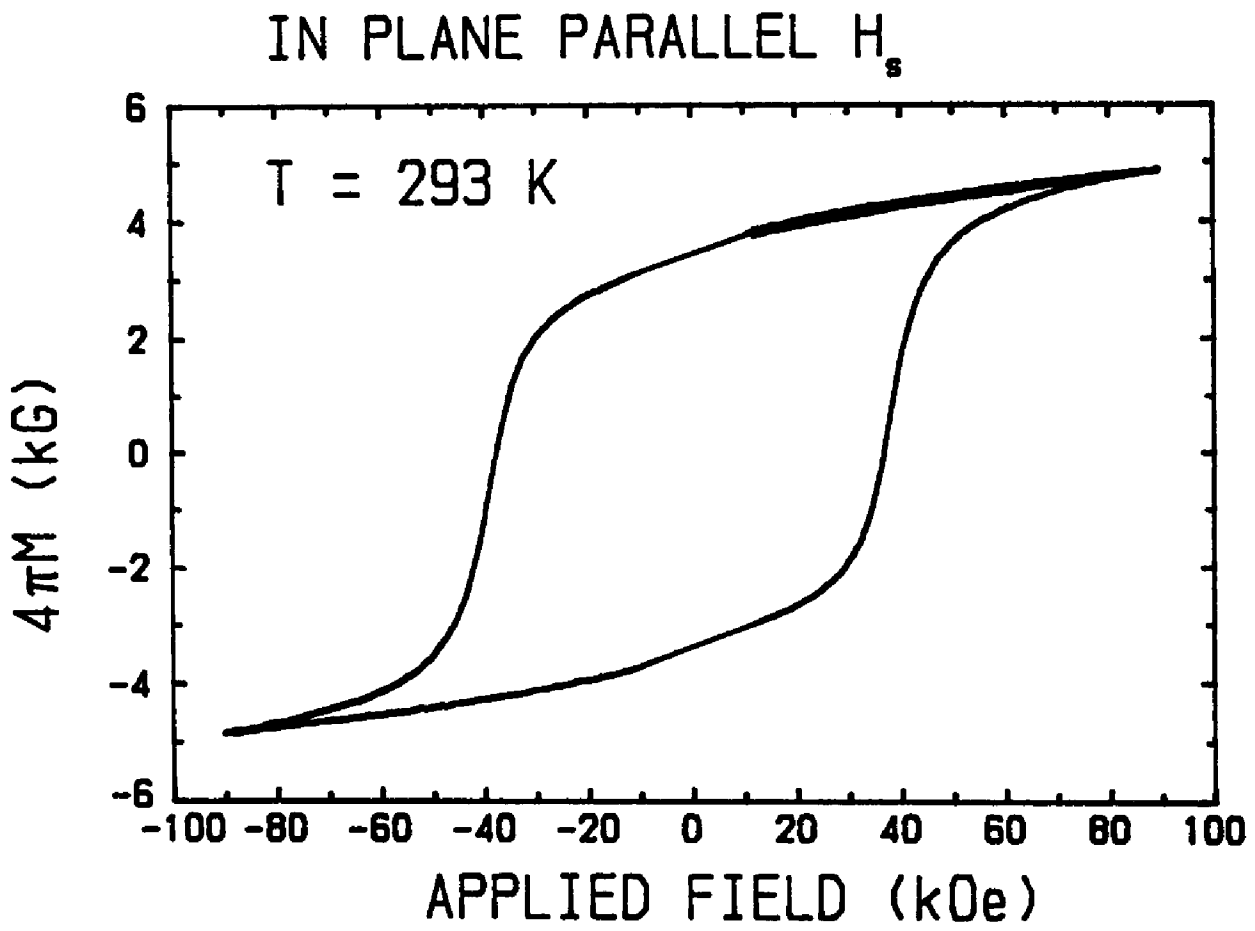
IN PLANE PARALLEL H_s
T = 293 K
$4\pi M$ (kG)
6
4
2
0
-2
-4
-6
-100 -80 -60 -40 -20 0 20 40 60 80 100
APPLIED FIELD (kOe)

Fig. 4.4

Fig. 4.5

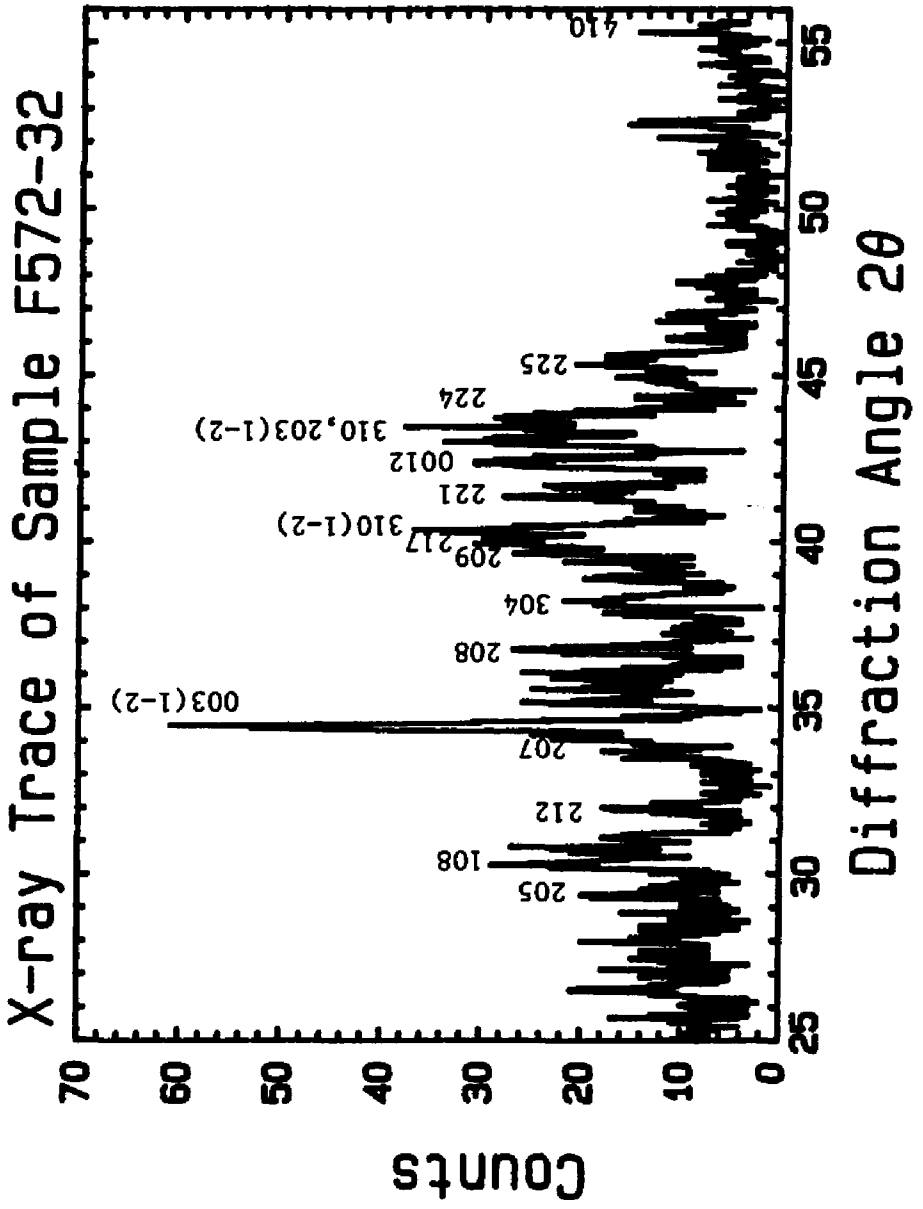
X-ray Trace of Sample F572-32
Counts
Diffraction Angle 2θ
0
10
20
30
40
50
60
70
25
30
35
40
45
50
55
205
108
212
207
003(1-2)
208
304
209
217
310(1-2)
221
0012
310,203(1-2)
224
225
410

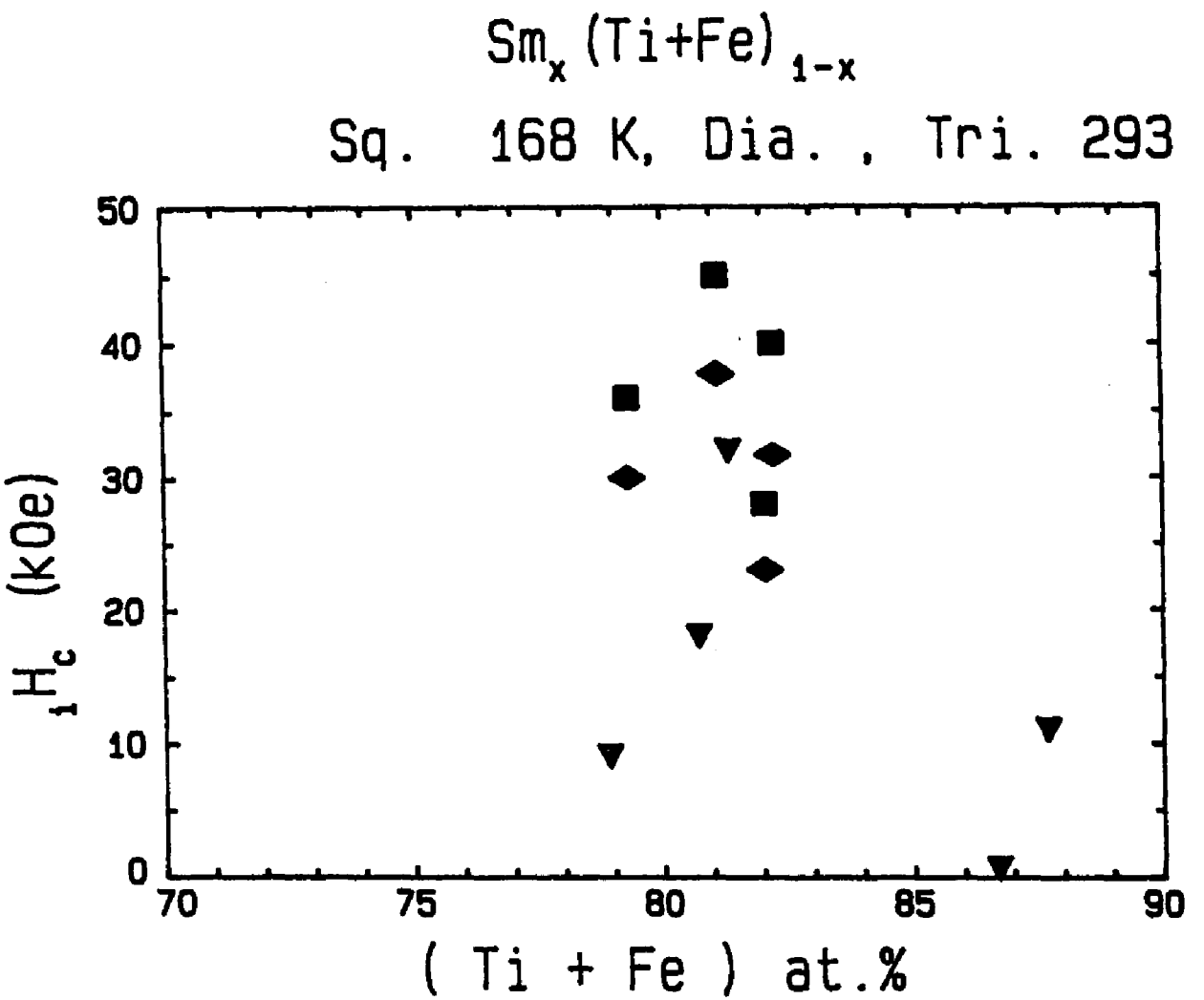
$Sm_x (Ti+Fe)_{1-x}$
Sq. 168 K, Dia. , Tri. 293 K
$_iH_c$ (kOe)
50
40
30
20
10
0
70
75
80
85
90
(Ti + Fe) at.%

Fig. 4.6

Fig. 4.7

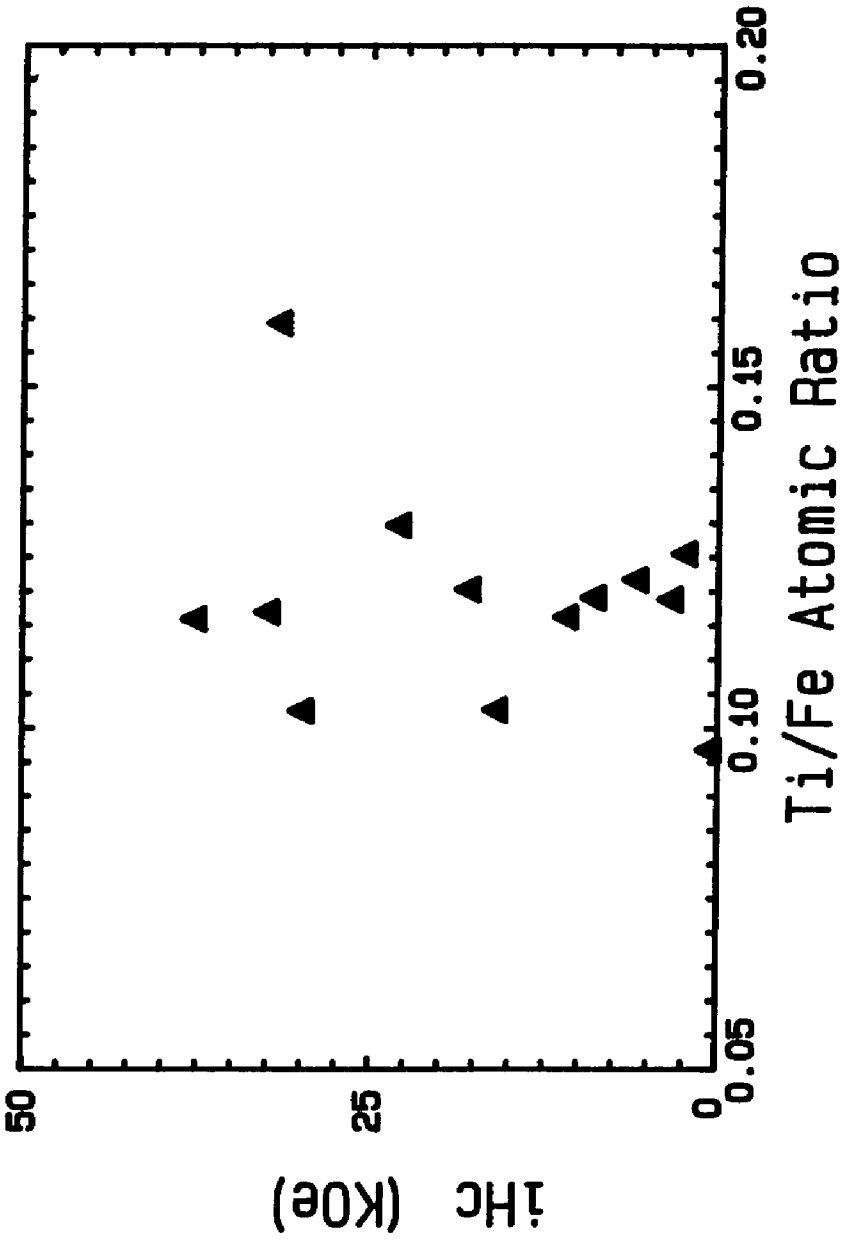

Fig. 4.8

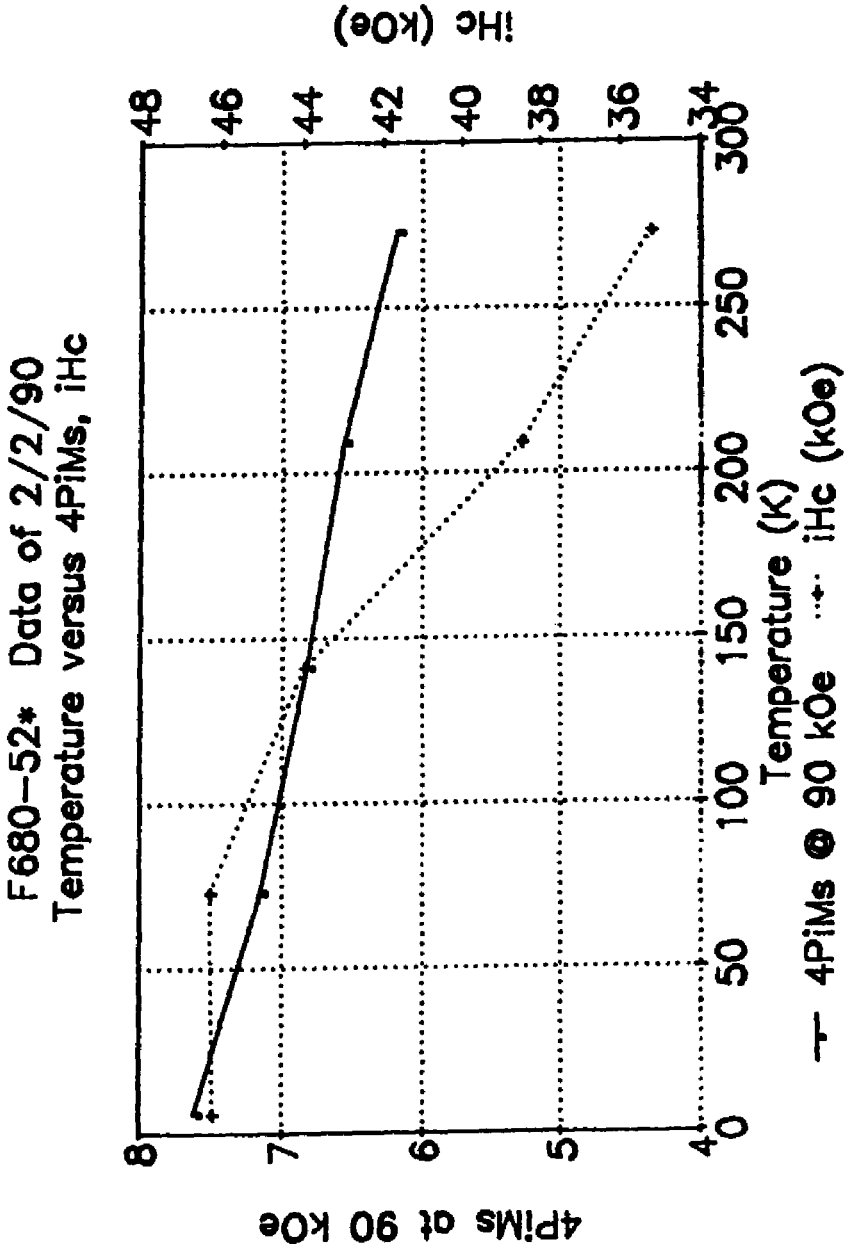
F680-52* Data of 2/2/90
Temperature versus 4PiMs, iHc
4PiMs @ 90 kOe
iHc (kOe)
Temperature (K)
— 4PiMs @ 90 kOe ··+·· iHc (kOe)
8
7
6
5
4
48
46
44
42
40
38
36
34
0
50
100
150
200
250
300

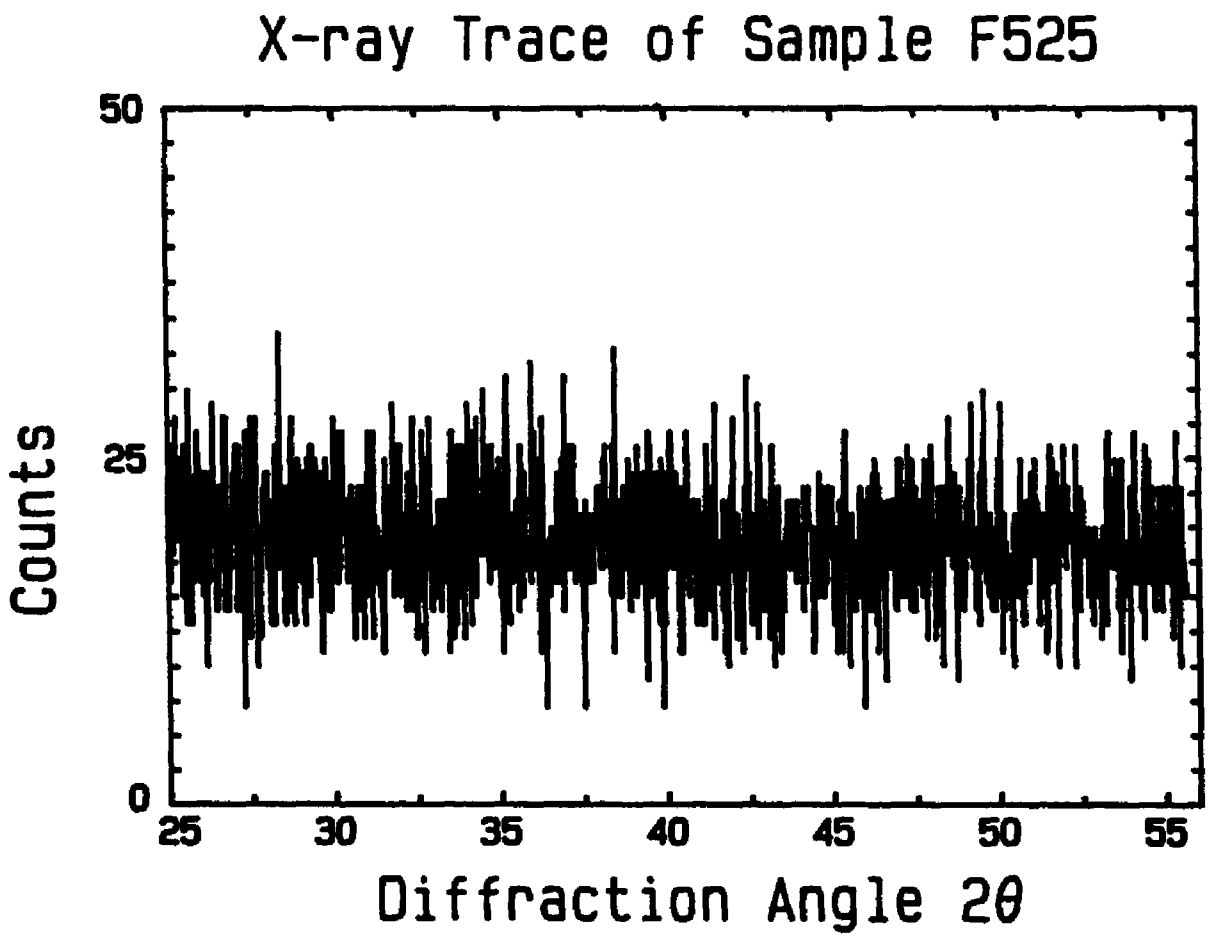
X-ray Trace of Sample F525
Counts
50
25
0
25
30
35
40
45
50
55
Diffraction Angle 2θ

Fig. 4.9

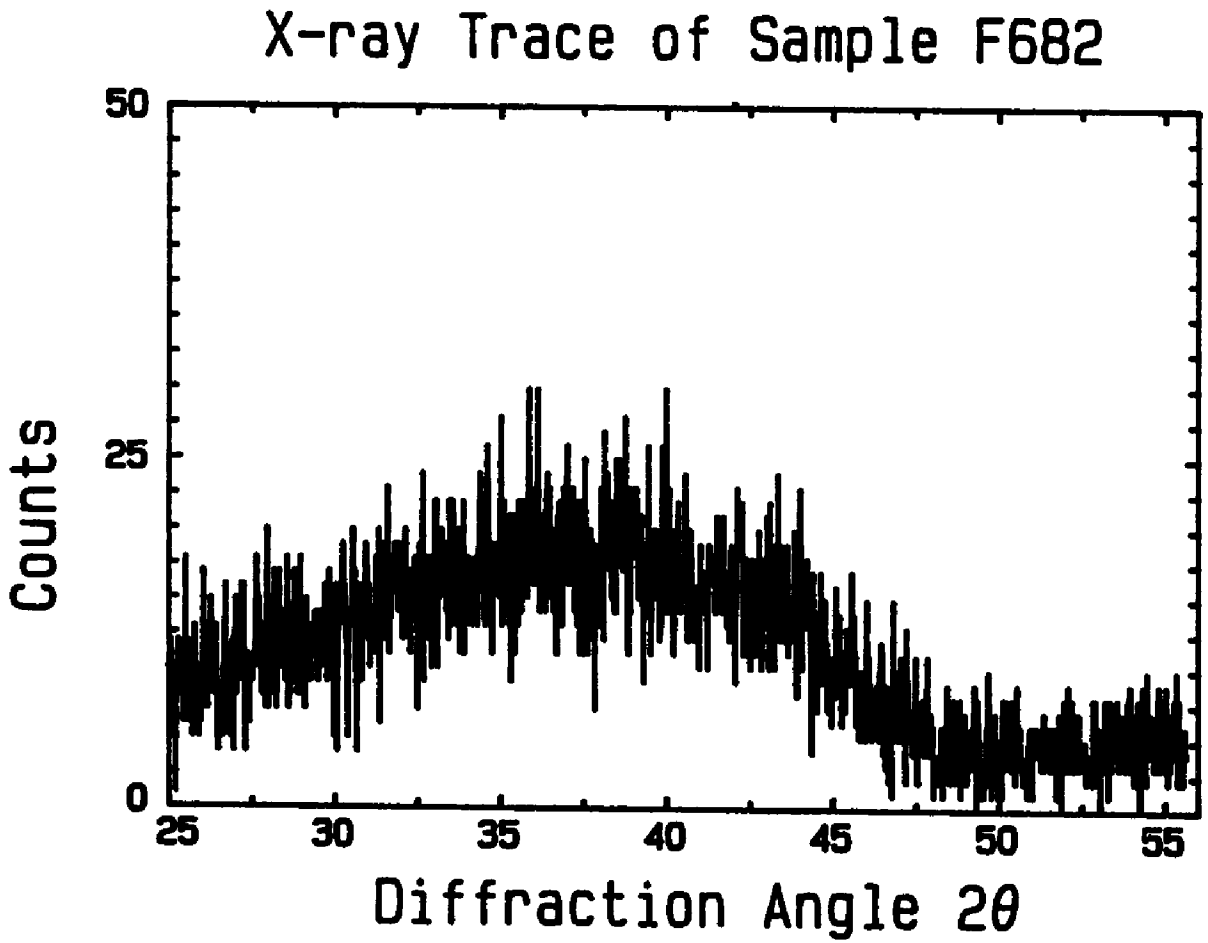
X-ray Trace of Sample F682
Counts
50
25
0
25
30
35
40
45
50
55
Diffraction Angle 2θ

Fig. 4.10

Fig. 4.11

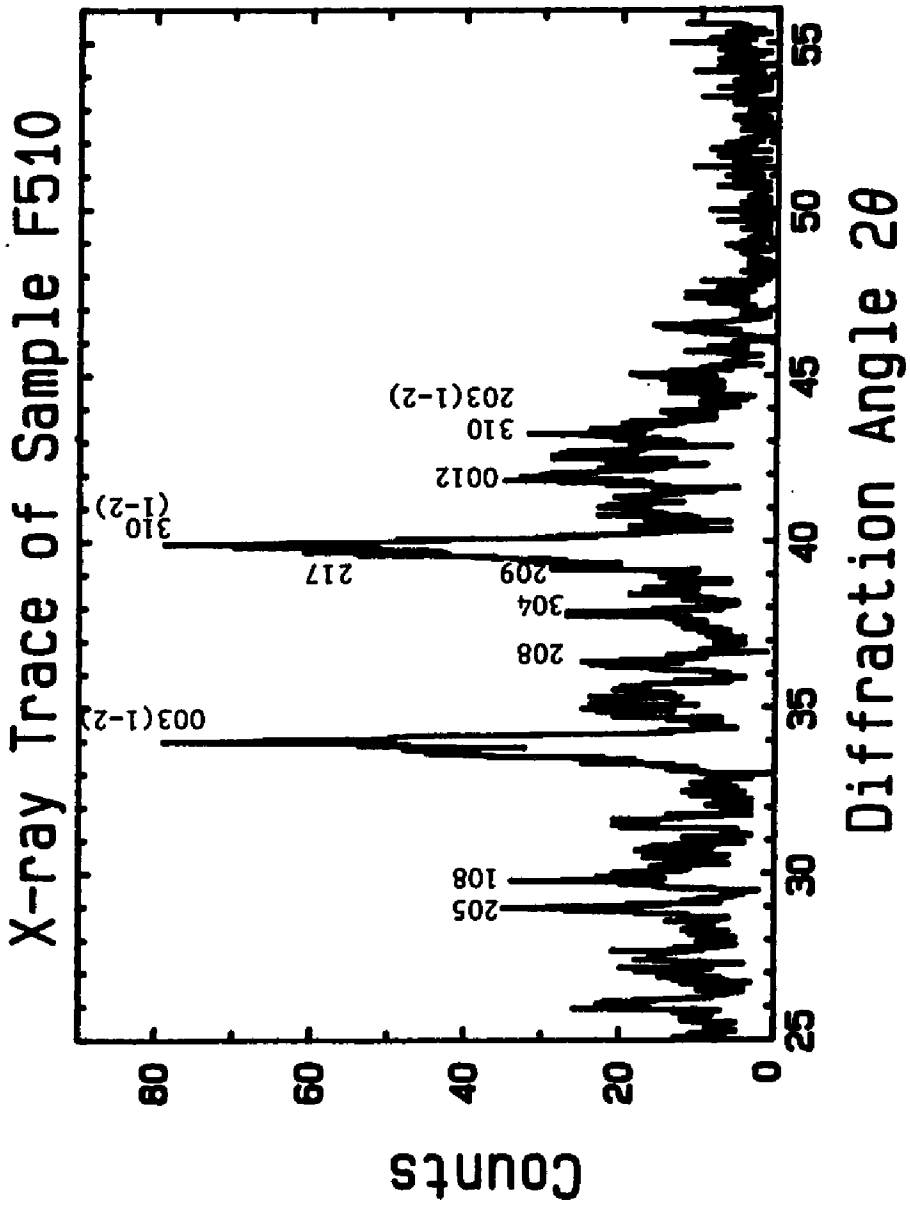
X-ray Trace of Sample F510
Counts
Diffraction Angle 2θ
0
20
40
60
80
25
30
35
40
45
50
55
108
205
003(1-2)
208
304
209
217
310
(1-2)
0012
310
203(1-2)

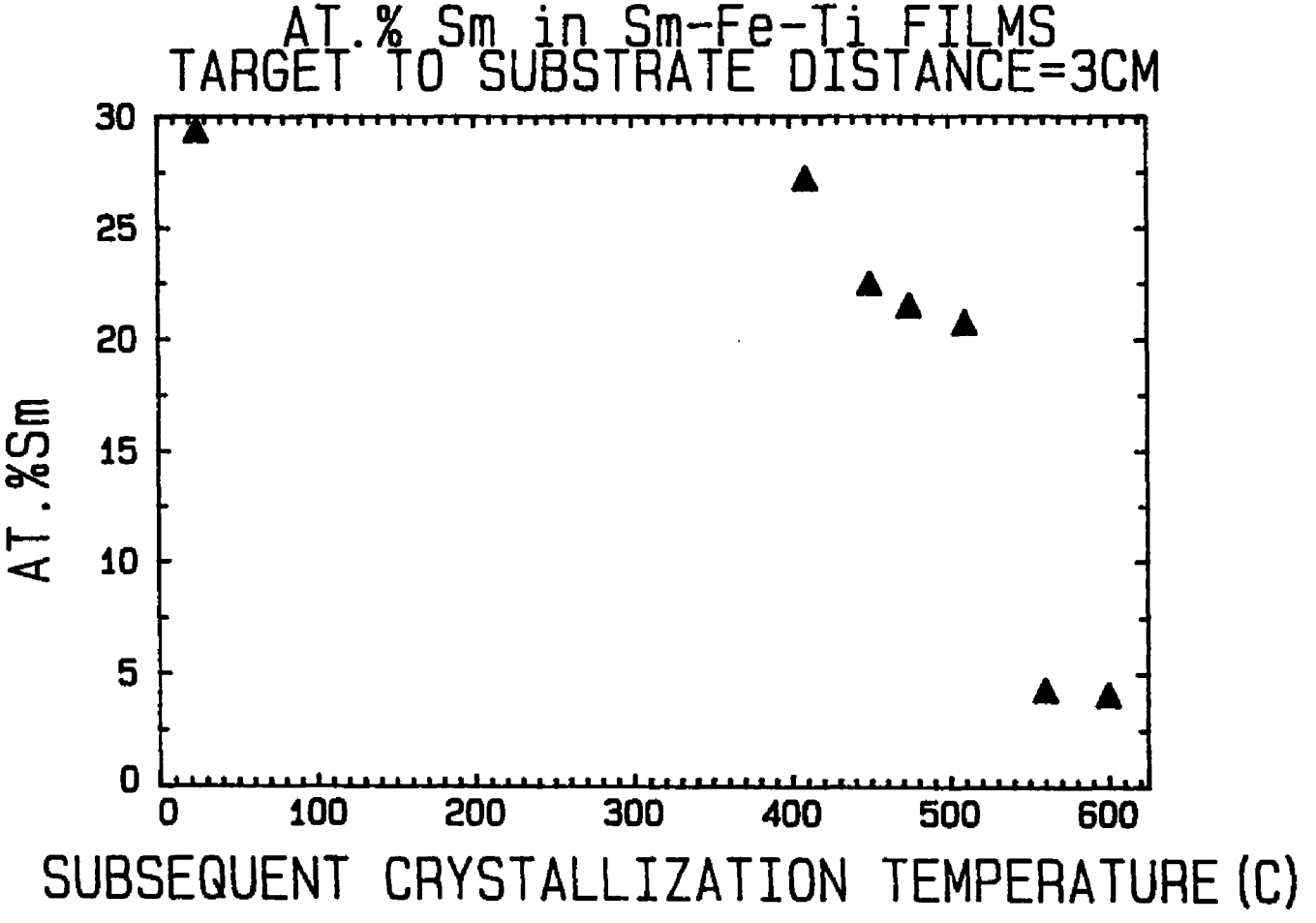
AT.% Sm in Sm-Fe-Ti FILMS
TARGET TO SUBSTRATE DISTANCE=3CM
AT.%Sm
30
25
20
15
10
5
0
0
100
200
300
400
500
600
SUBSEQUENT CRYSTALLIZATION TEMPERATURE (C)

Fig. 4.12

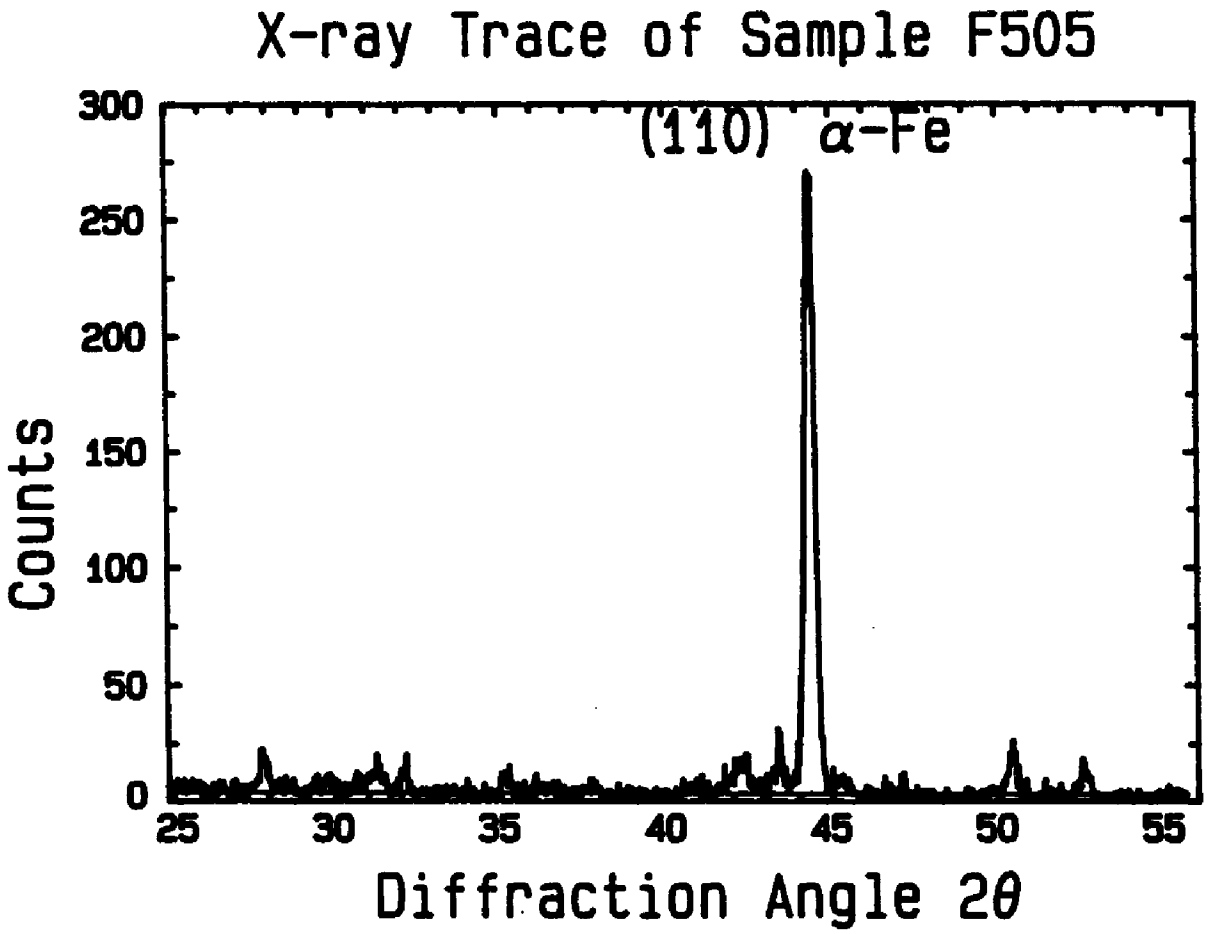
X-ray Trace of Sample F505
(110) α-Fe
Counts
300
250
200
150
100
50
0
25
30
35
40
45
50
55
Diffraction Angle 2θ

Fig. 4.13

Fig. 4.14

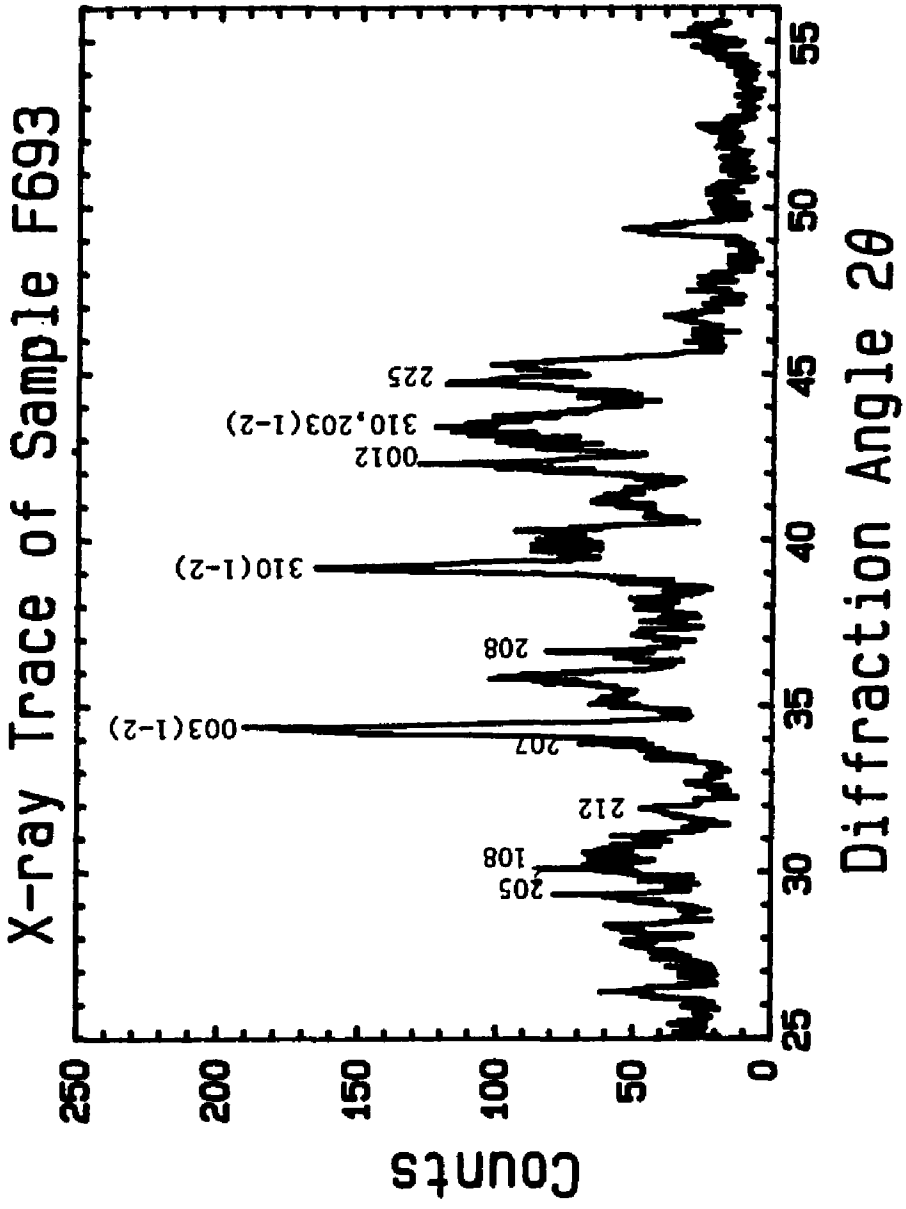
X-ray Trace of Sample F693
Counts
Diffraction Angle 2θ
250
200
150
100
50
0
25
30
35
40
45
50
55
205
108
212
207
003(1-2)
208
310(1-2)
0012
310,203(1-2)
225

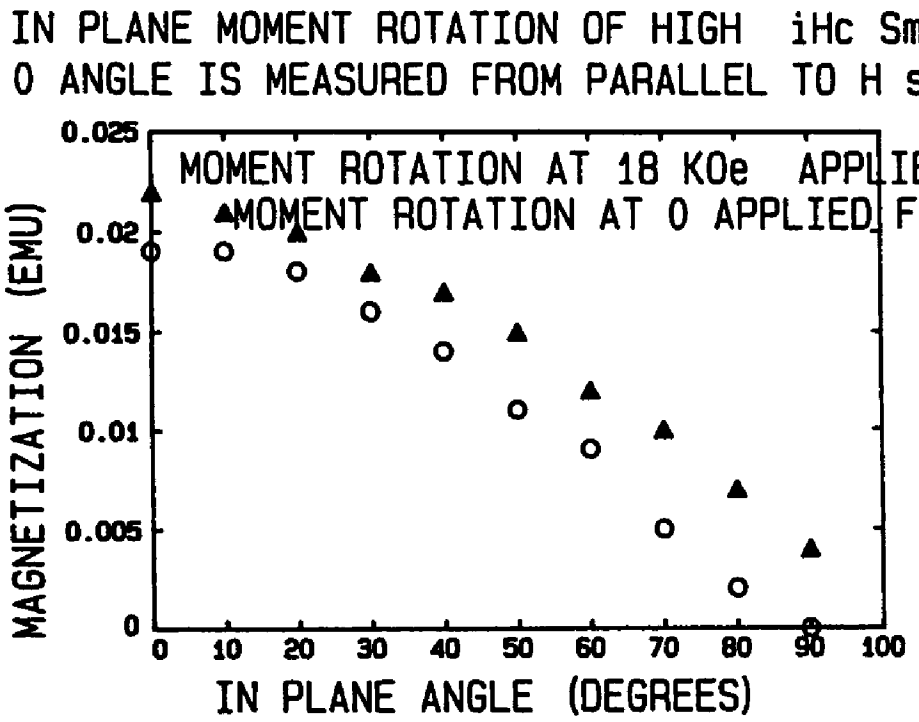
IN PLANE MOMENT ROTATION OF HIGH iHc Sm-Ti-Fe PHASE
0 ANGLE IS MEASURED FROM PARALLEL TO H sputter
MOMENT ROTATION AT 18 KOe APPLIED FIELD
MOMENT ROTATION AT 0 APPLIED FIELD
MAGNETIZATION (EMU)
0.025
0.02
0.015
0.01
0.005
0
0
10
20
30
40
50
60
70
80
90
100
IN PLANE ANGLE (DEGREES)

Fig. 4.15

Fig. 4.16

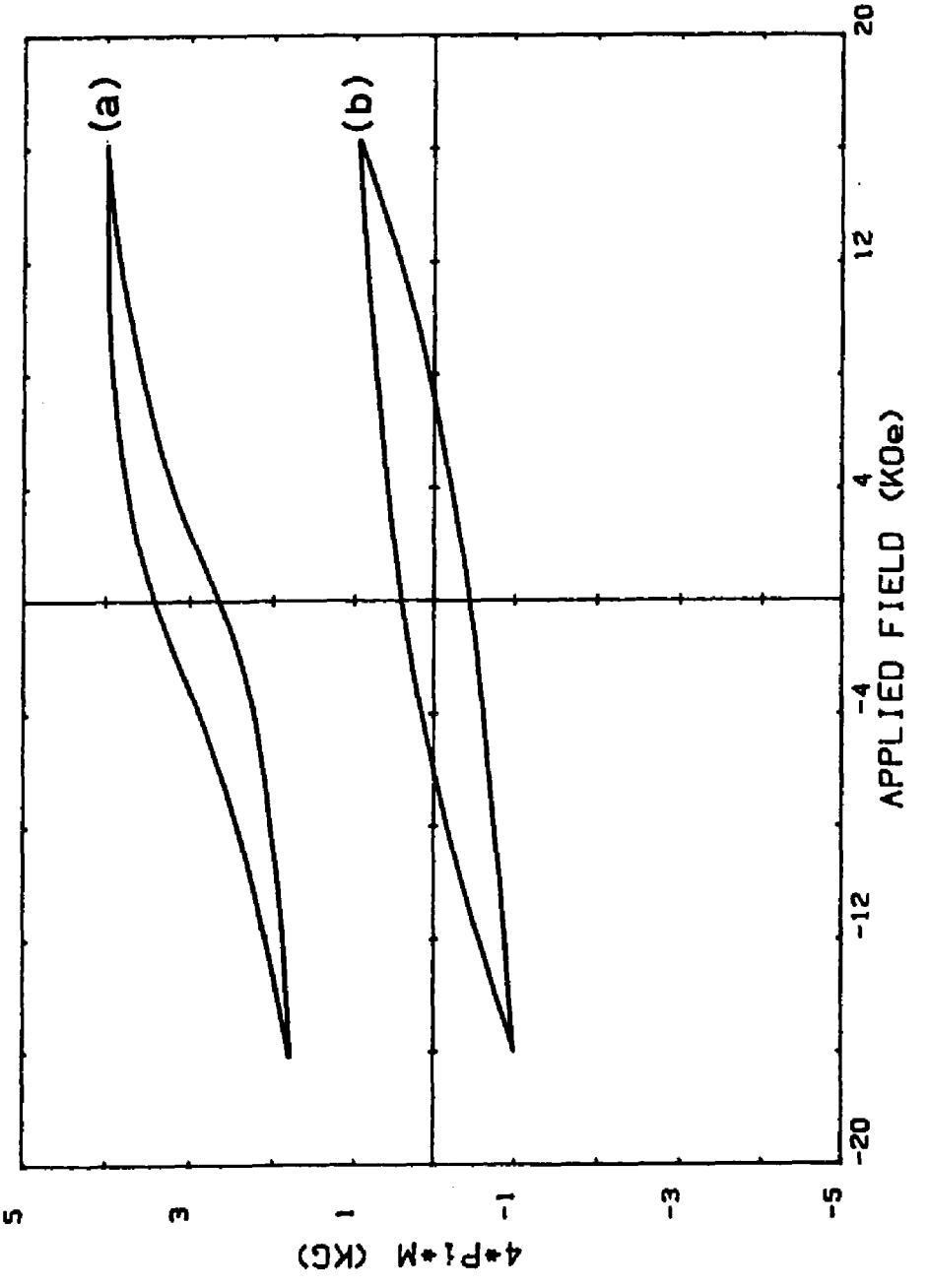

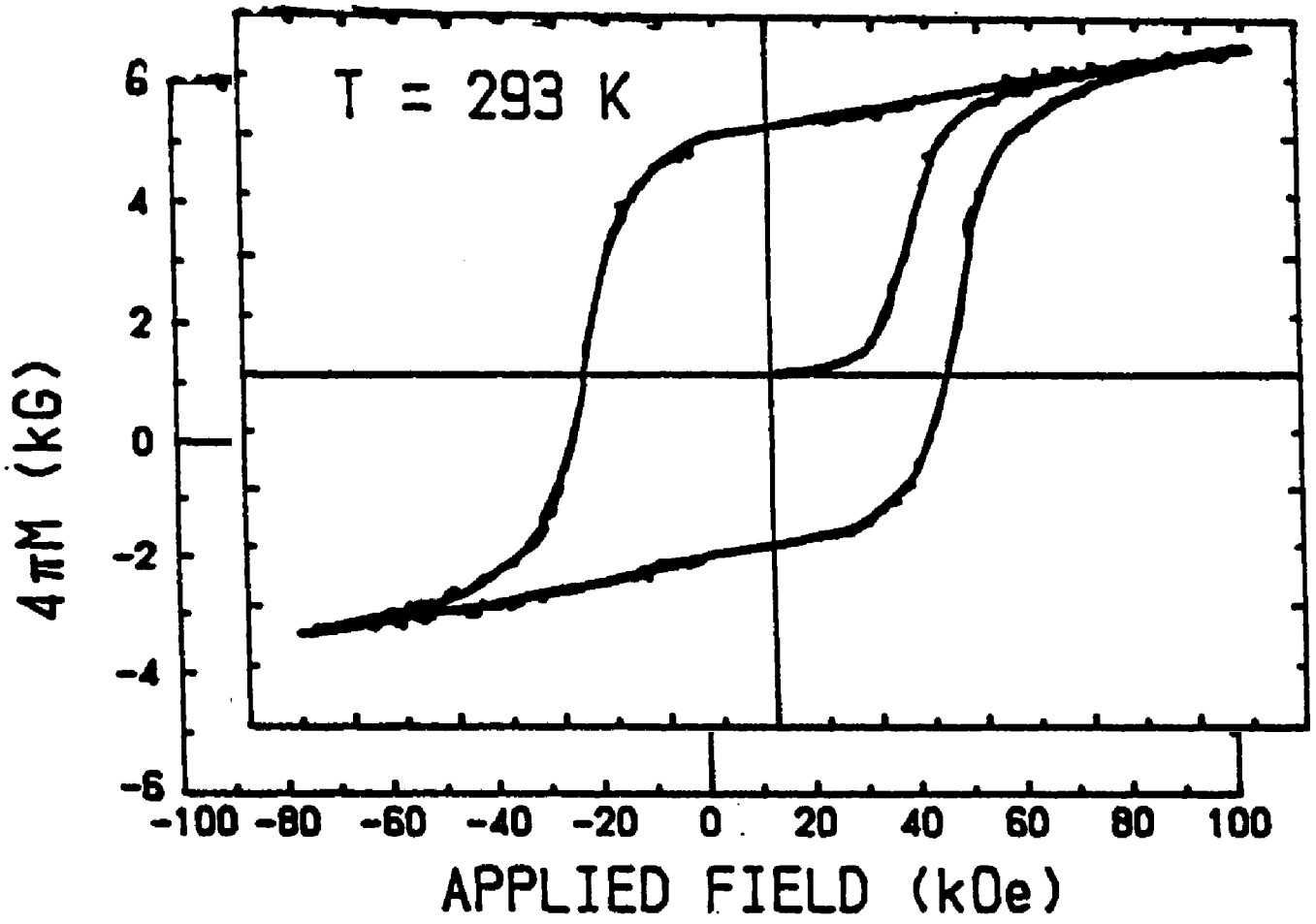
T = 293 K
4πM (kG)
6
4
2
0
-2
-4
-6
-100 -80 -60 -40 -20 0 20 40 60 80 100
APPLIED FIELD (kOe)

Fig. 4.17

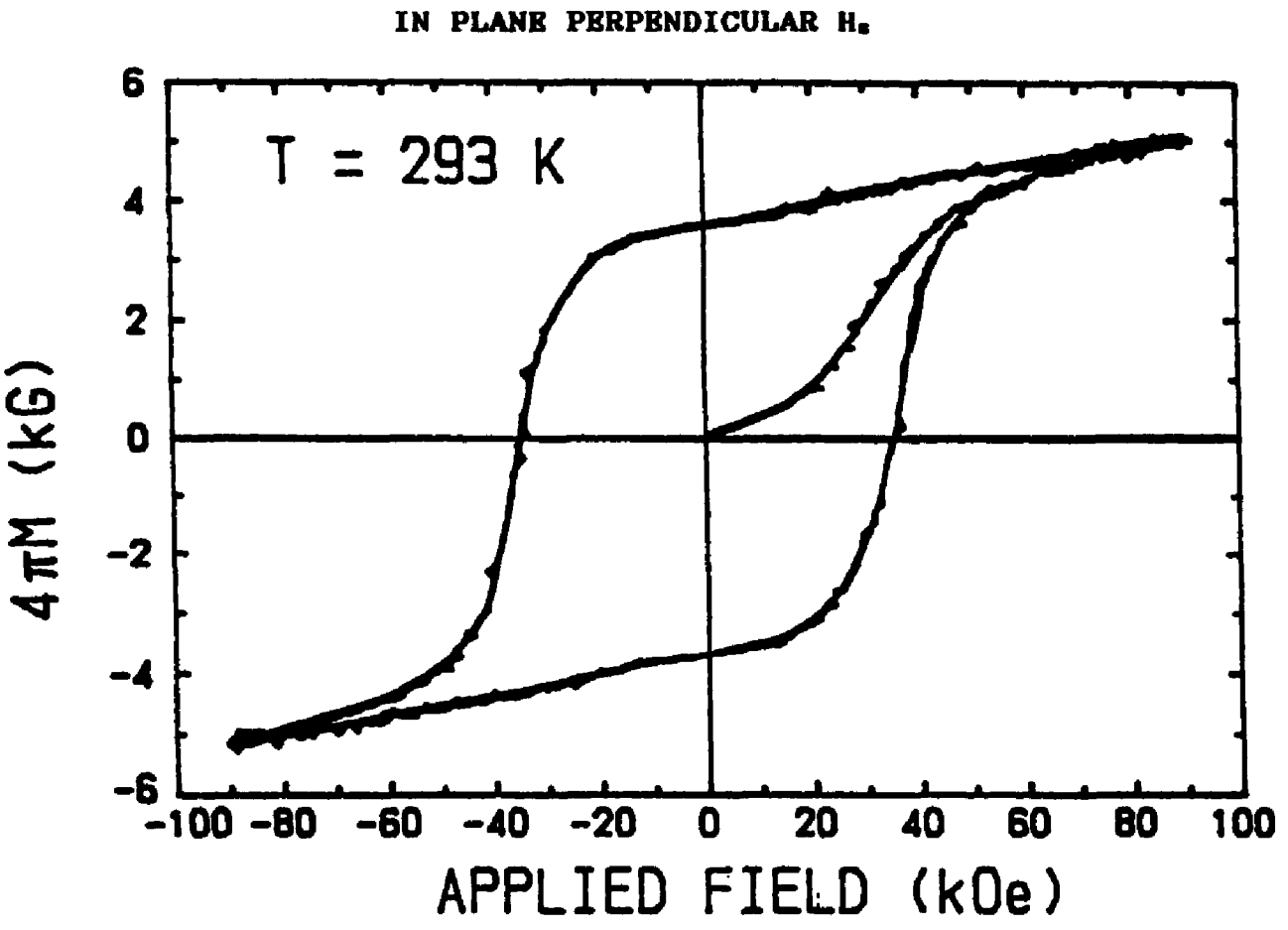
IN PLANE PERPENDICULAR H_e
T = 293 K
$4\pi M$ (kG)
6
4
2
0
-2
-4
-6
-100 -80 -60 -40 -20 0 20 40 60 80 100
APPLIED FIELD (kOe)

Fig. 4.18

Fig. 4.19

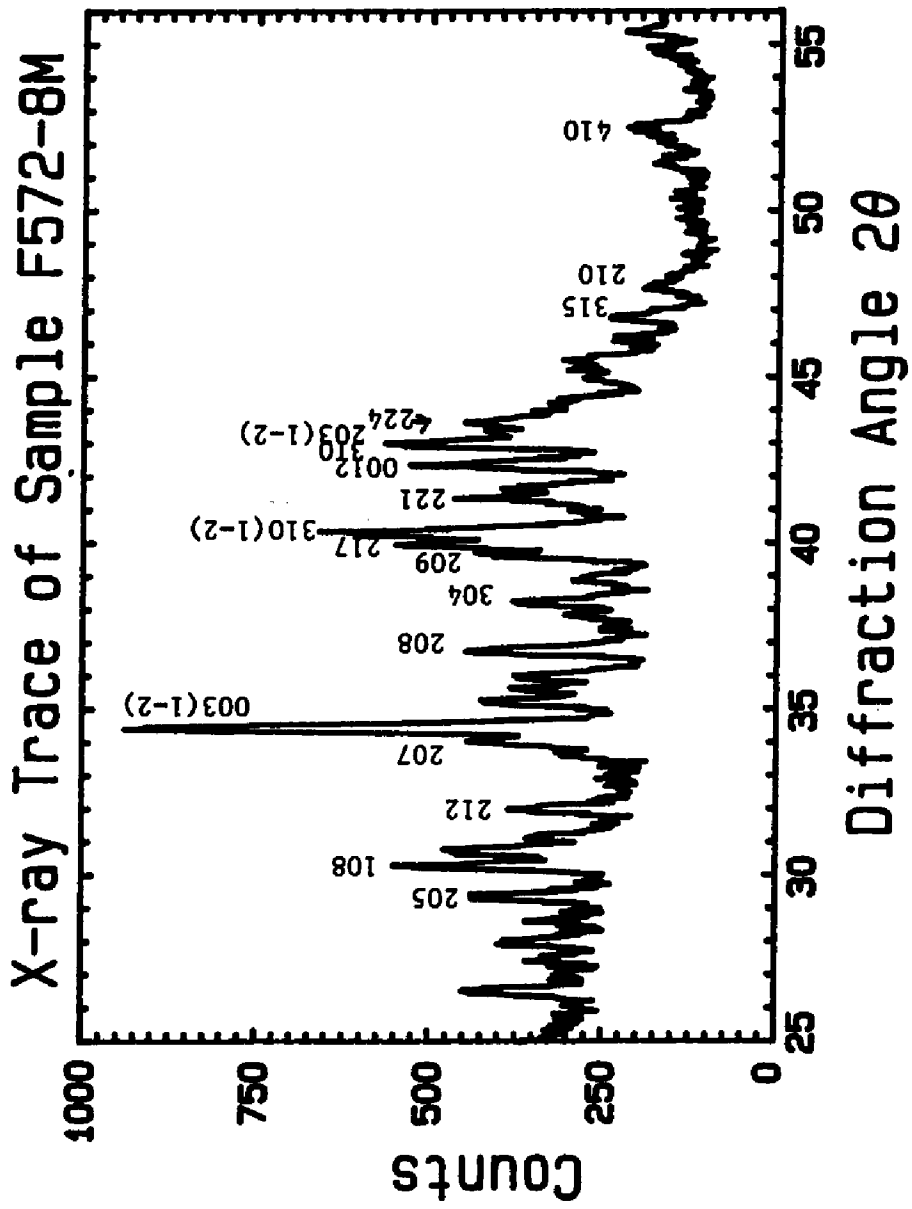
X-ray Trace of Sample F572-8M
Counts
1000
750
500
250
0
Diffraction Angle 2θ
25
30
35
40
45
50
55
410
315
210
224
203(1-2)
310
0012
221
310(1-2)
217
209
304
208
003(1-2)
207
212
108
205

Fig. 4.20

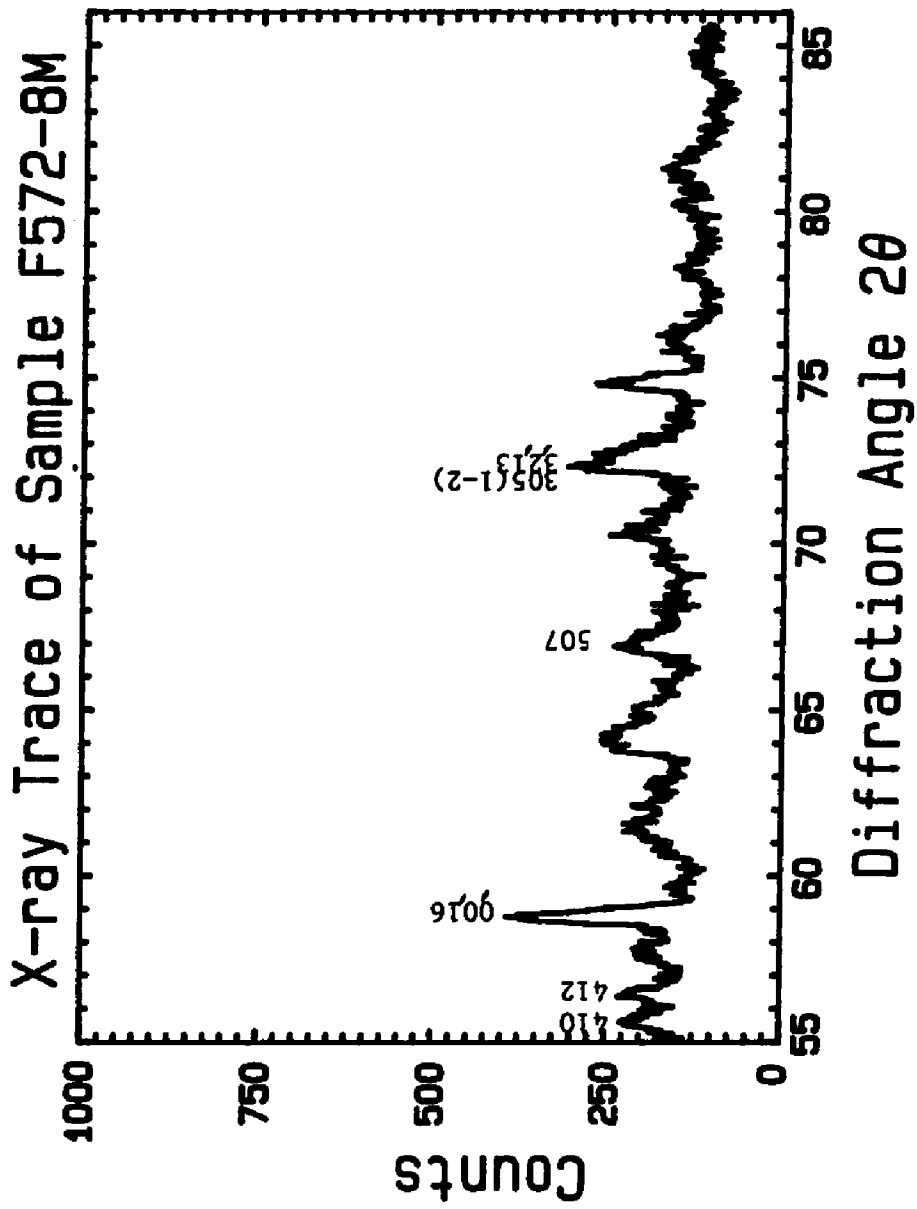
X-ray Trace of Sample F572-8M
Counts
1000
750
500
250
0
55
60
65
70
75
80
85
Diffraction Angle 2θ
410
412
9016
507
3053(1-2)
3213

Fig. 4.21

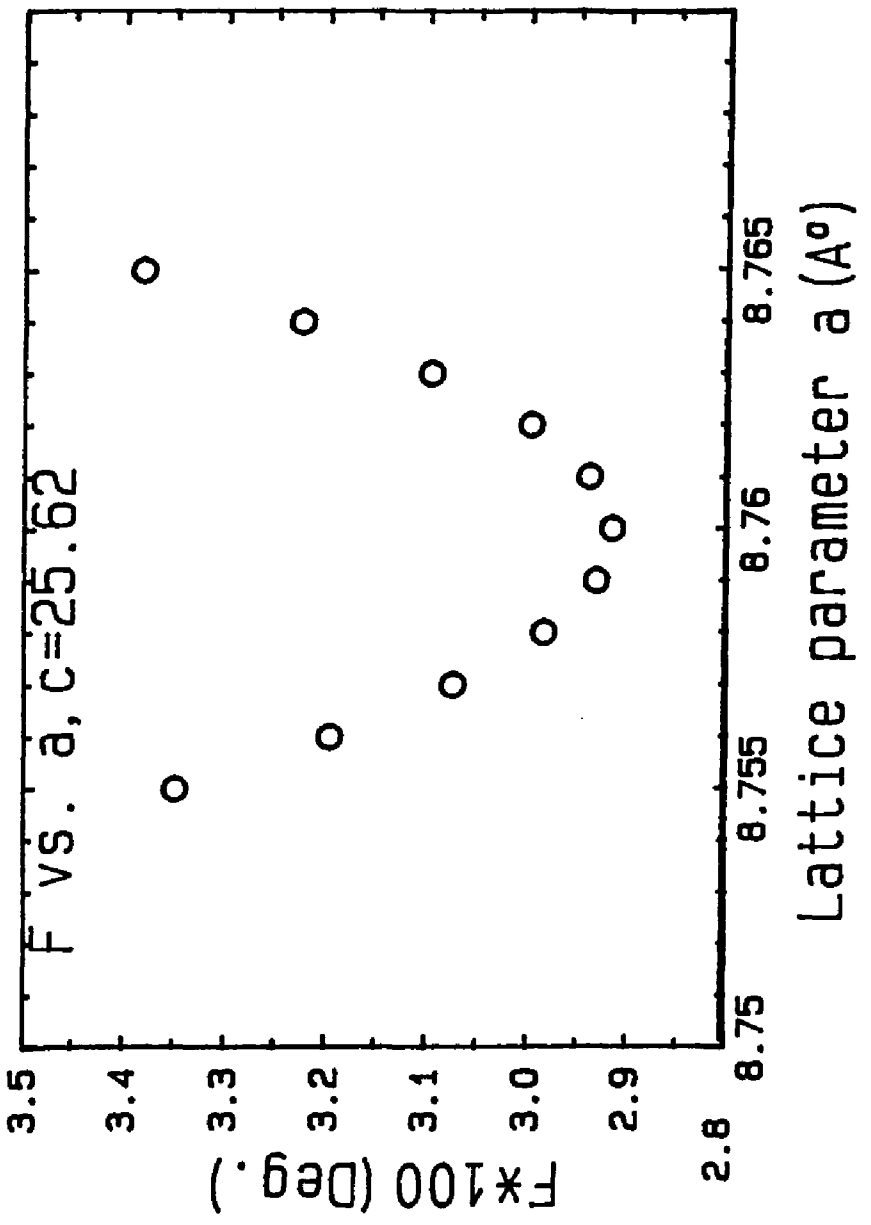
F vs. a, c=25.62
F*100 (Deg.)
Lattice parameter a (A°)
3.5
3.4
3.3
3.2
3.1
3.0
2.9
2.8
8.75
8.755
8.76
8.765

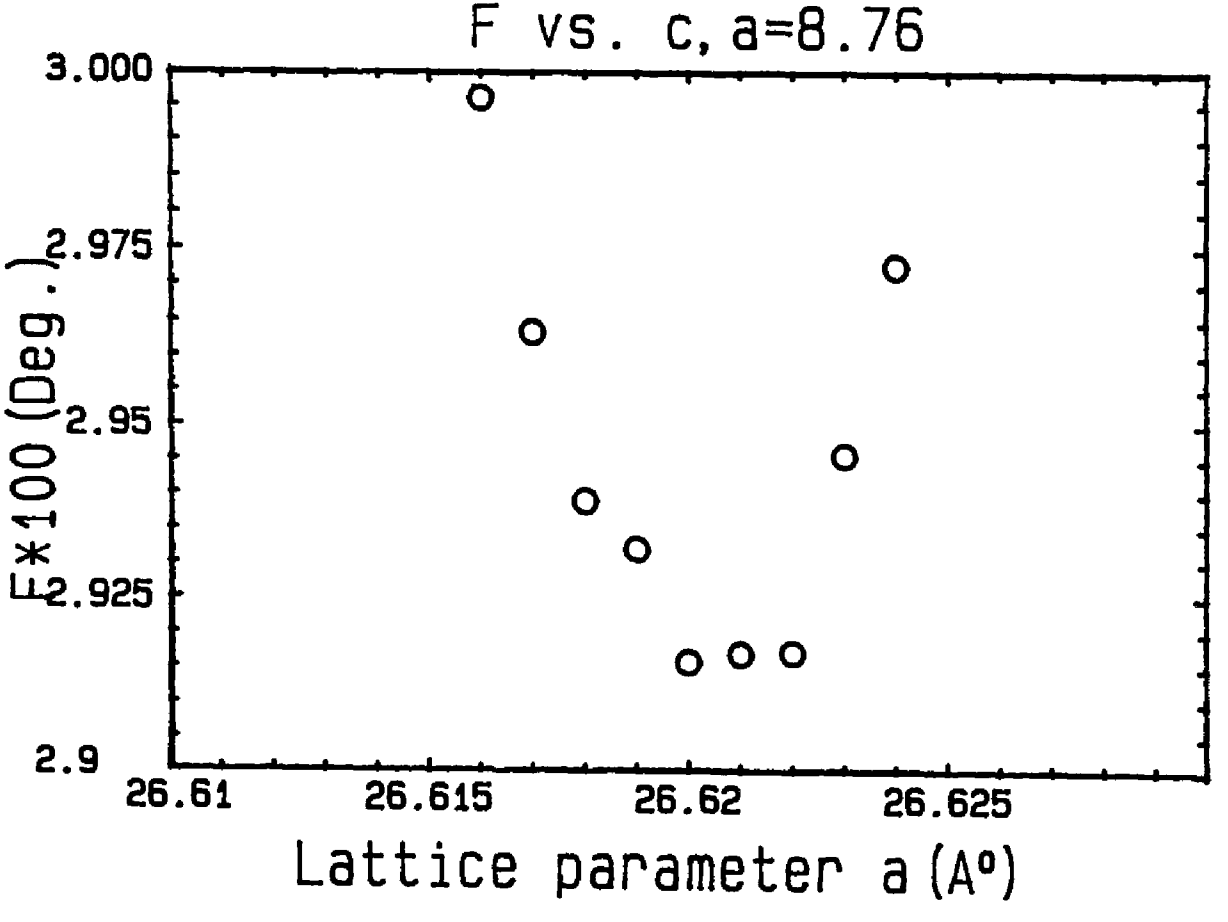
F vs. c, a=8.76
3.000
2.975
2.95
2.925
2.9
E*100 (Deg.)
26.61
26.615
26.62
26.625
Lattice parameter a (A°)

Fig. 4.22

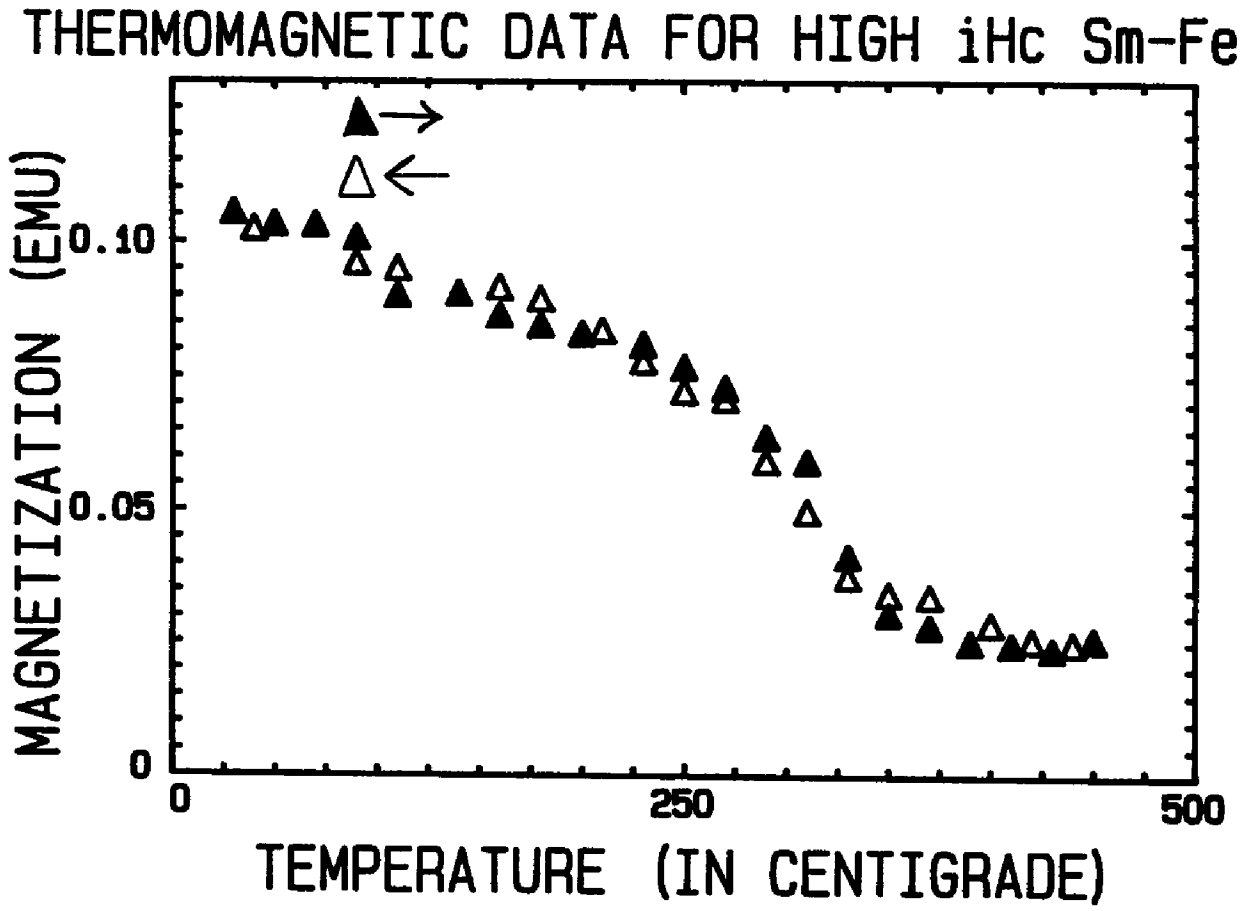
THERMOMAGNETIC DATA FOR HIGH iHc Sm-Fe-Ti
MAGNETIZATION (EMU)
0.10
0.05
0
0
250
500
TEMPERATURE (IN CENTIGRADE)

Fig. 4.23

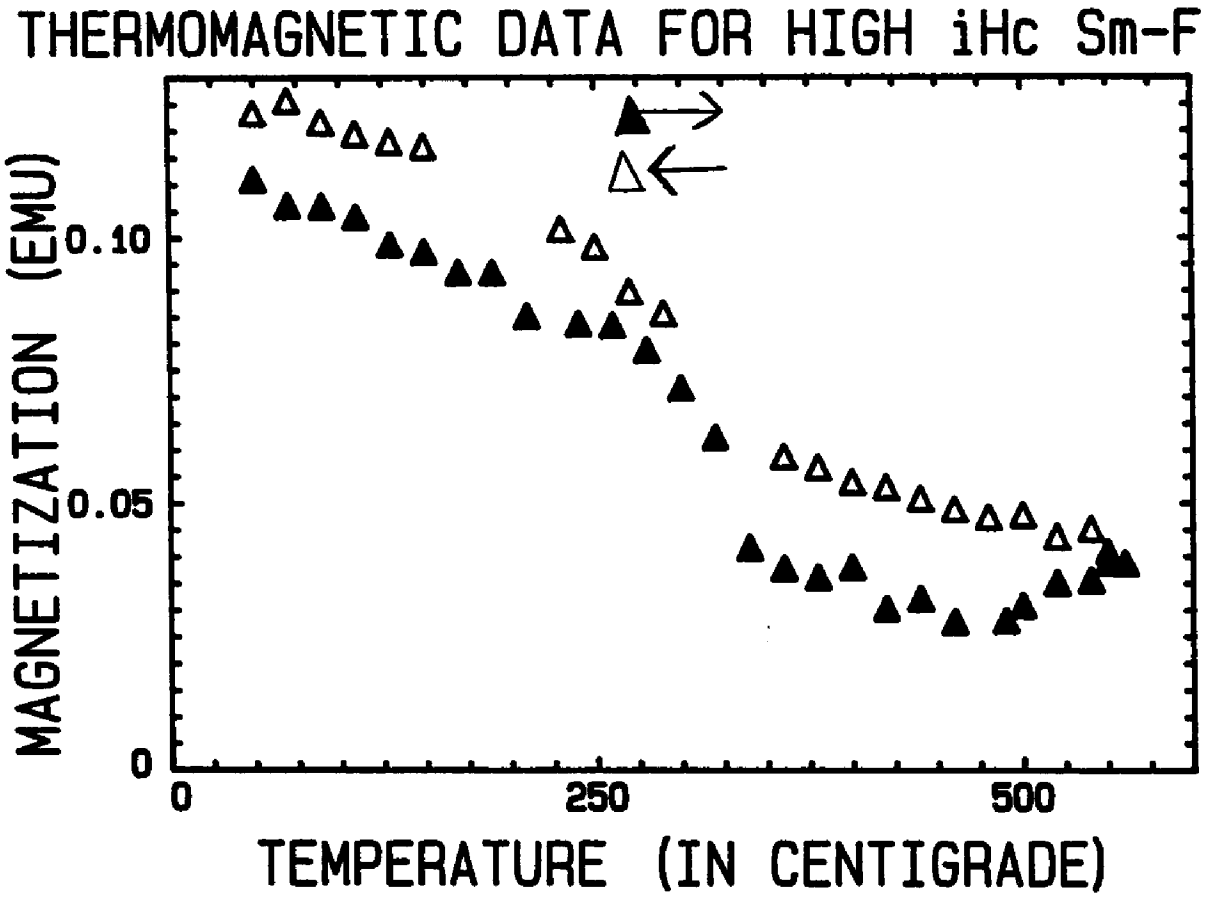
THERMOMAGNETIC DATA FOR HIGH iHc Sm-Fe-Ti
MAGNETIZATION (EMU)
0.10
0.05
0
0
250
500
TEMPERATURE (IN CENTIGRADE)

Fig. 4.24

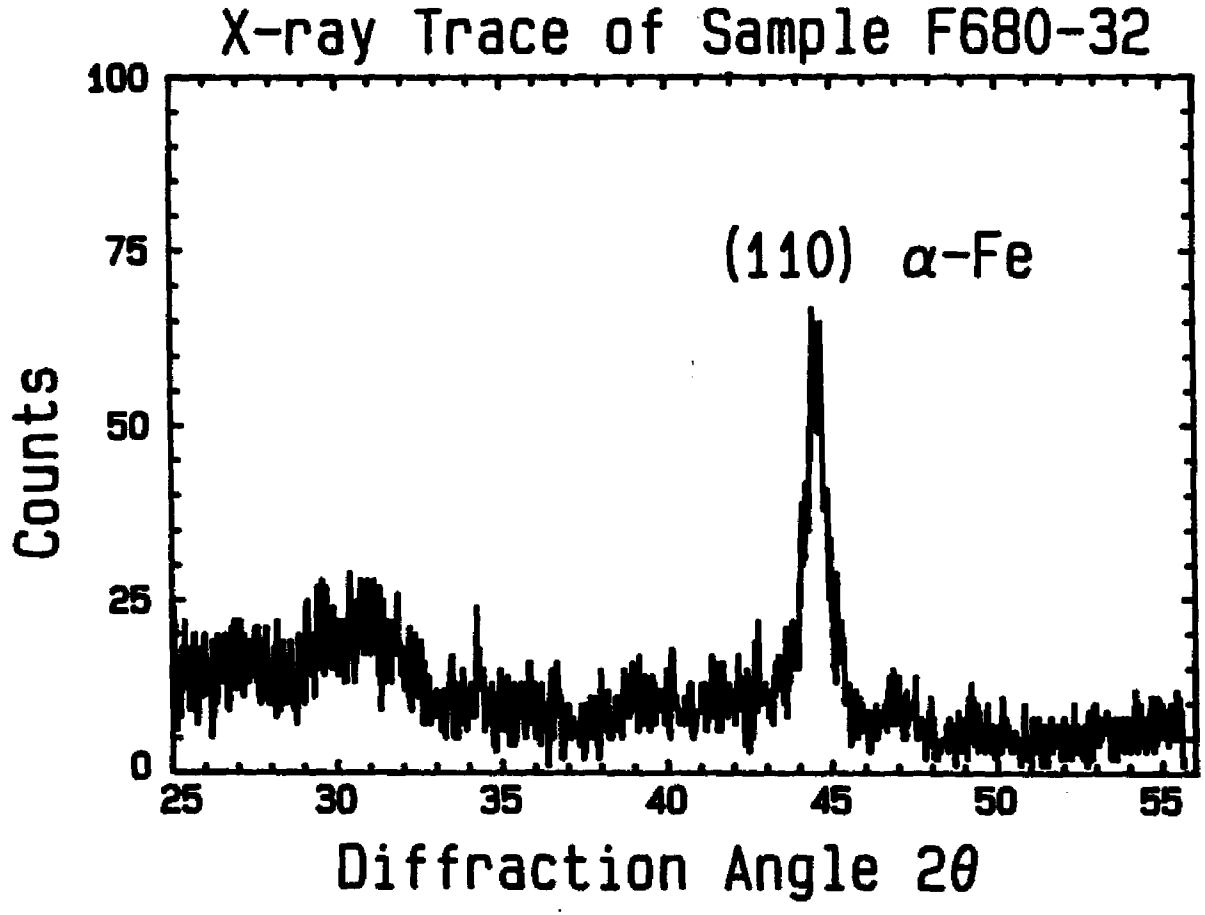
X-ray Trace of Sample F680-32
100
75
50
25
0
Counts
(110) α-Fe
25
30
35
40
45
50
55
Diffraction Angle 2θ

Fig. 4.25

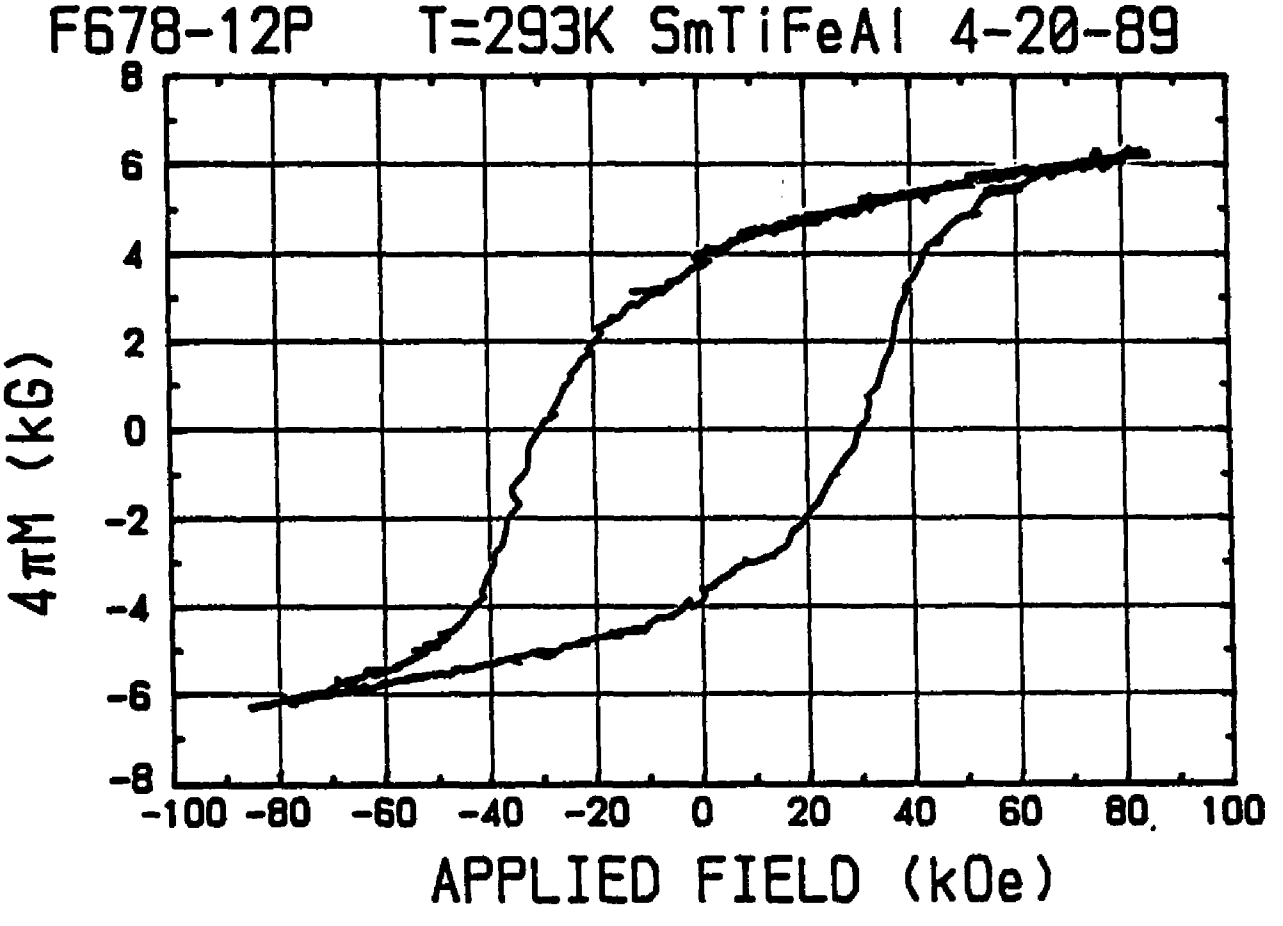
F678-12P T=293K SmTiFeAl 4-20-89
4πM (kG)
8
6
4
2
0
-2
-4
-6
-8
-100 -80 -60 -40 -20 0 20 40 60 80 100
APPLIED FIELD (kOe)

Fig. 4.26

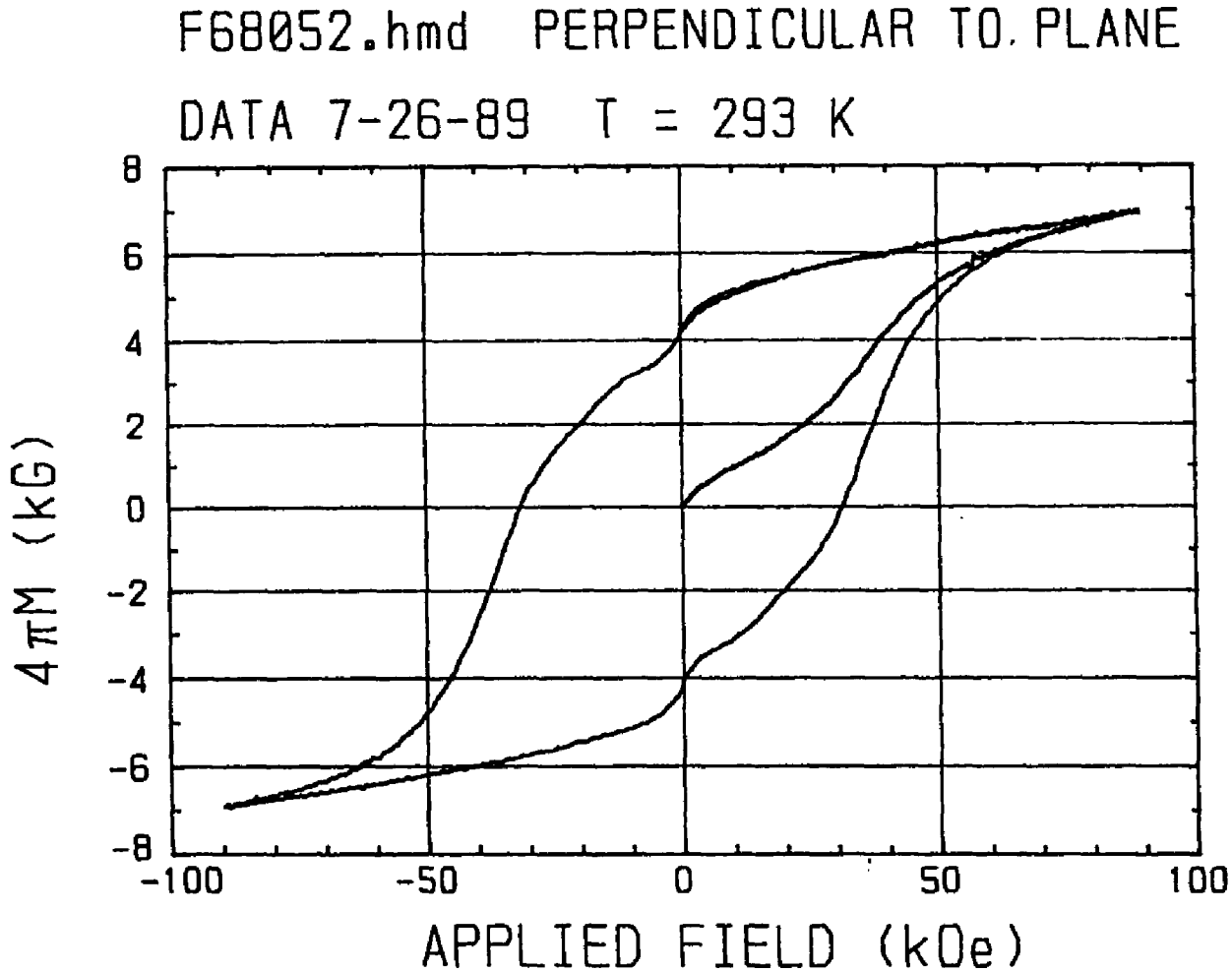
F68052.hmd PERPENDICULAR TO PLANE
DATA 7-26-89 T = 293 K
8
6
4
2
0
-2
-4
-6
-8
4πM (kG)
-100
-50
0
50
100
APPLIED FIELD (kOe)

Fig. 4.27

Fig. 4.28

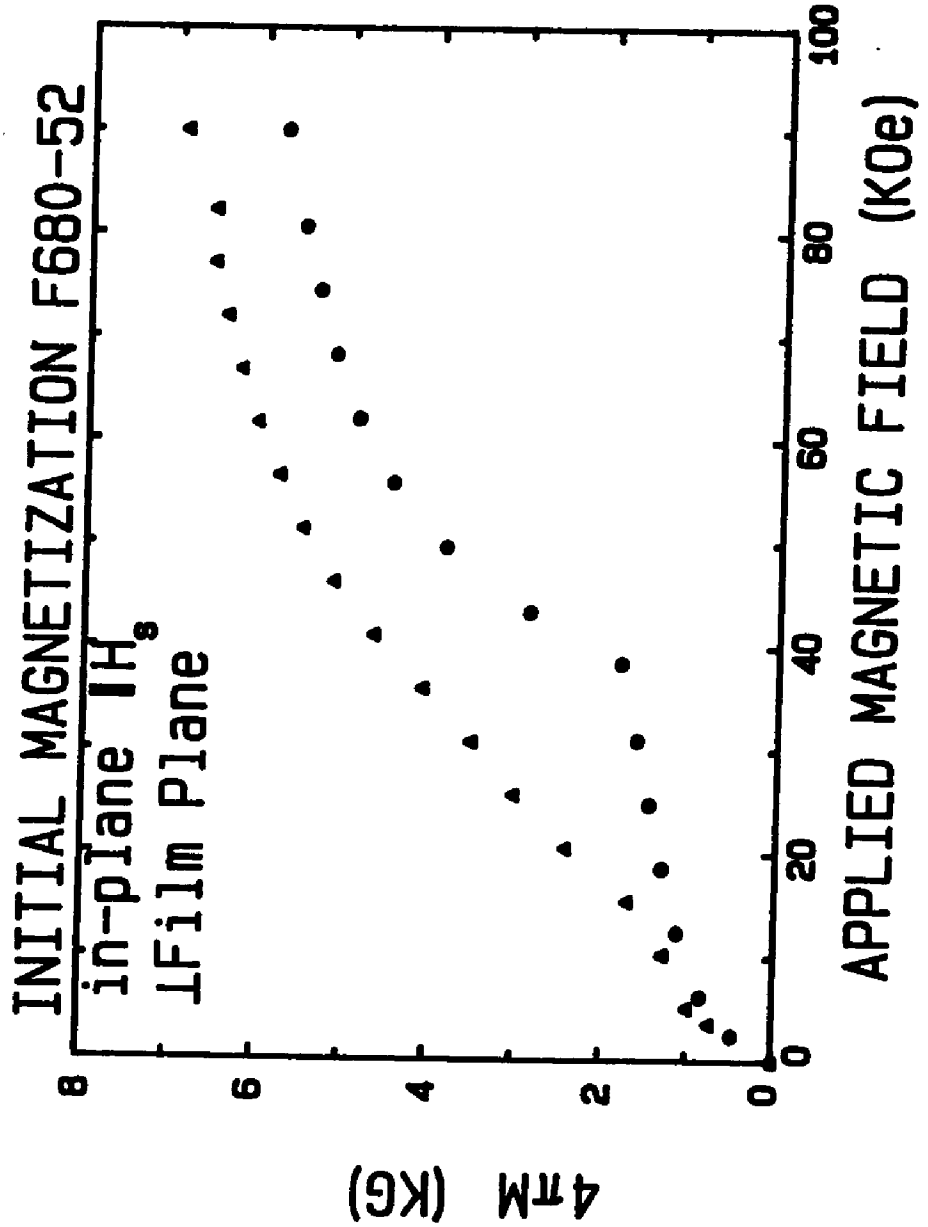
INITIAL MAGNETIZATION F680-52
in-plane H_s
⊥Film Plane
4πM (KG)
APPLIED MAGNETIC FIELD (KOe)
0
2
4
6
8
0
20
40
60
80
100

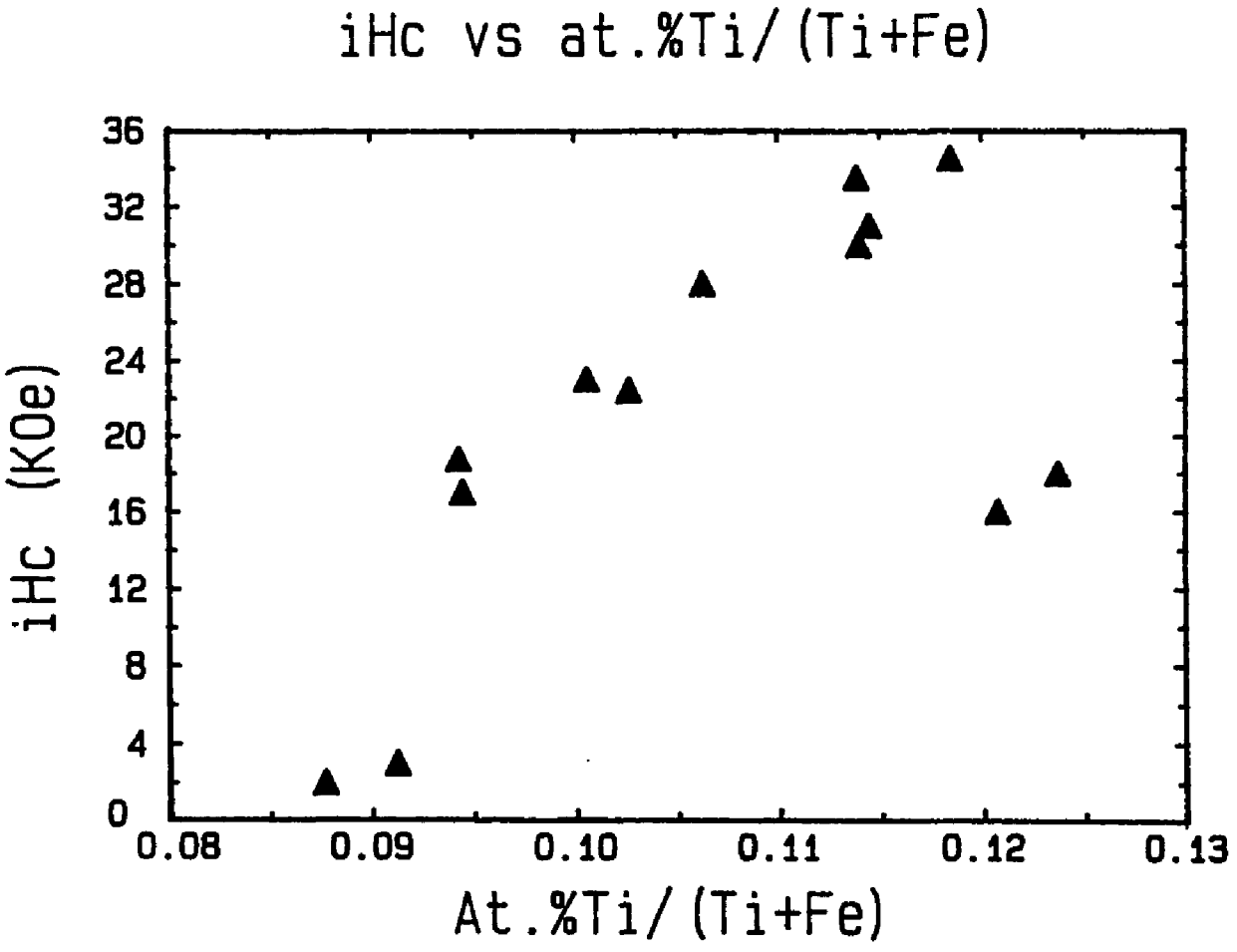
iHc vs at.%Ti/(Ti+Fe)
iHc (KOe)
36
32
28
24
20
16
12
8
4
0
0.08
0.09
0.10
0.11
0.12
0.13
At.%Ti/(Ti+Fe)

Fig. 4.29

Fig. 4.30

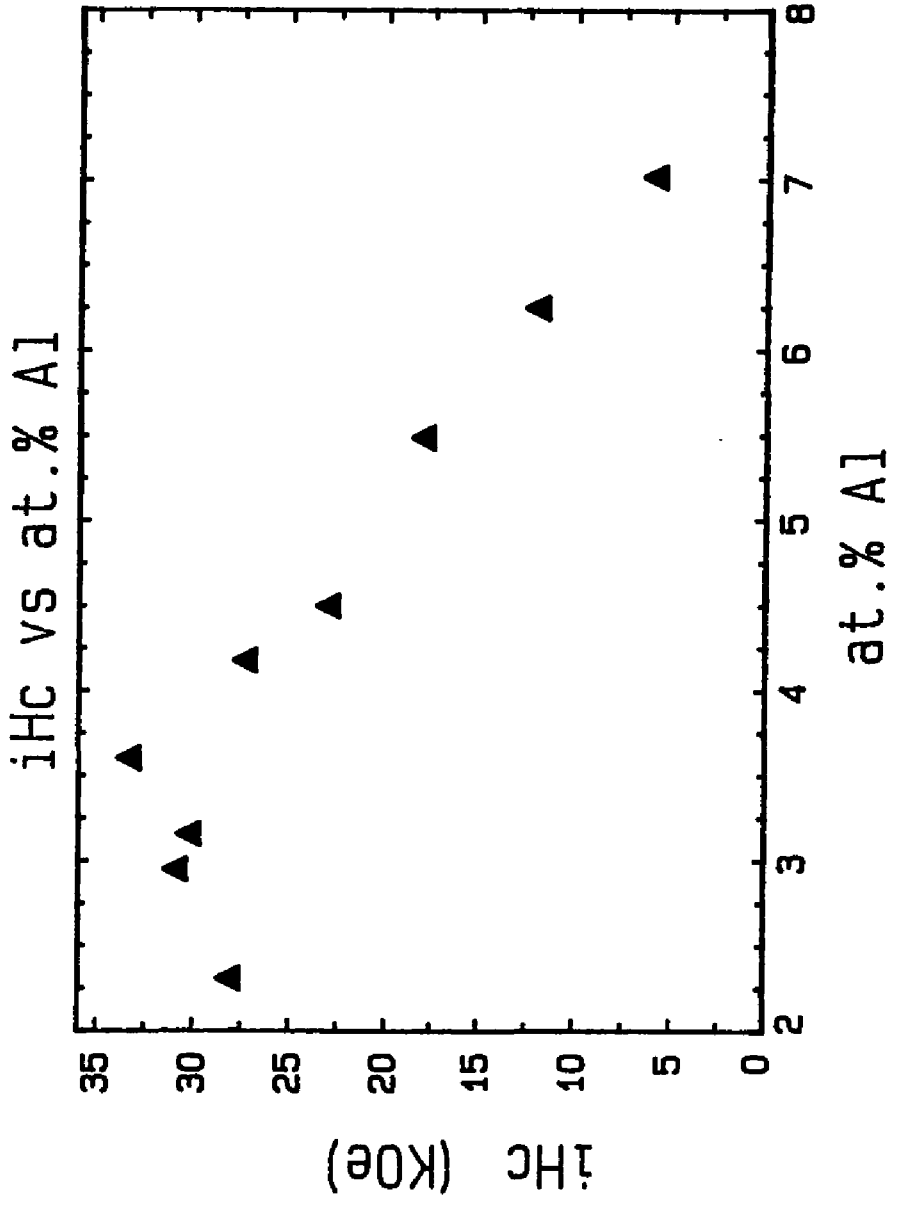

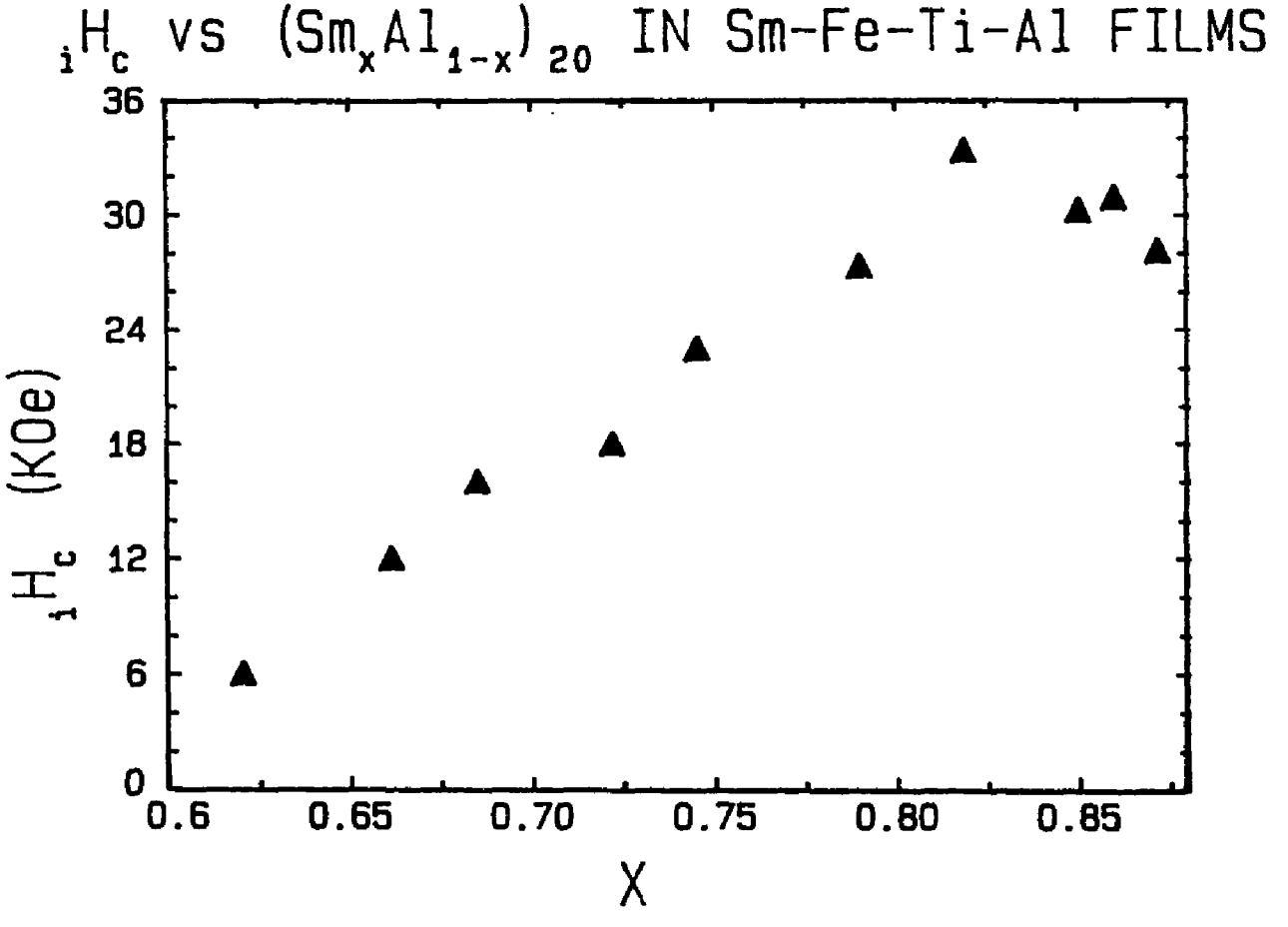
$_iH_c$ vs $(Sm_xAl_{1-x})_{20}$ IN Sm-Fe-Ti-Al FILMS
$_iH_c$ (KOe)
36
30
24
18
12
6
0
0.6
0.65
0.70
0.75
0.80
0.85
X

Fig. 4.31

Fig. 4.32

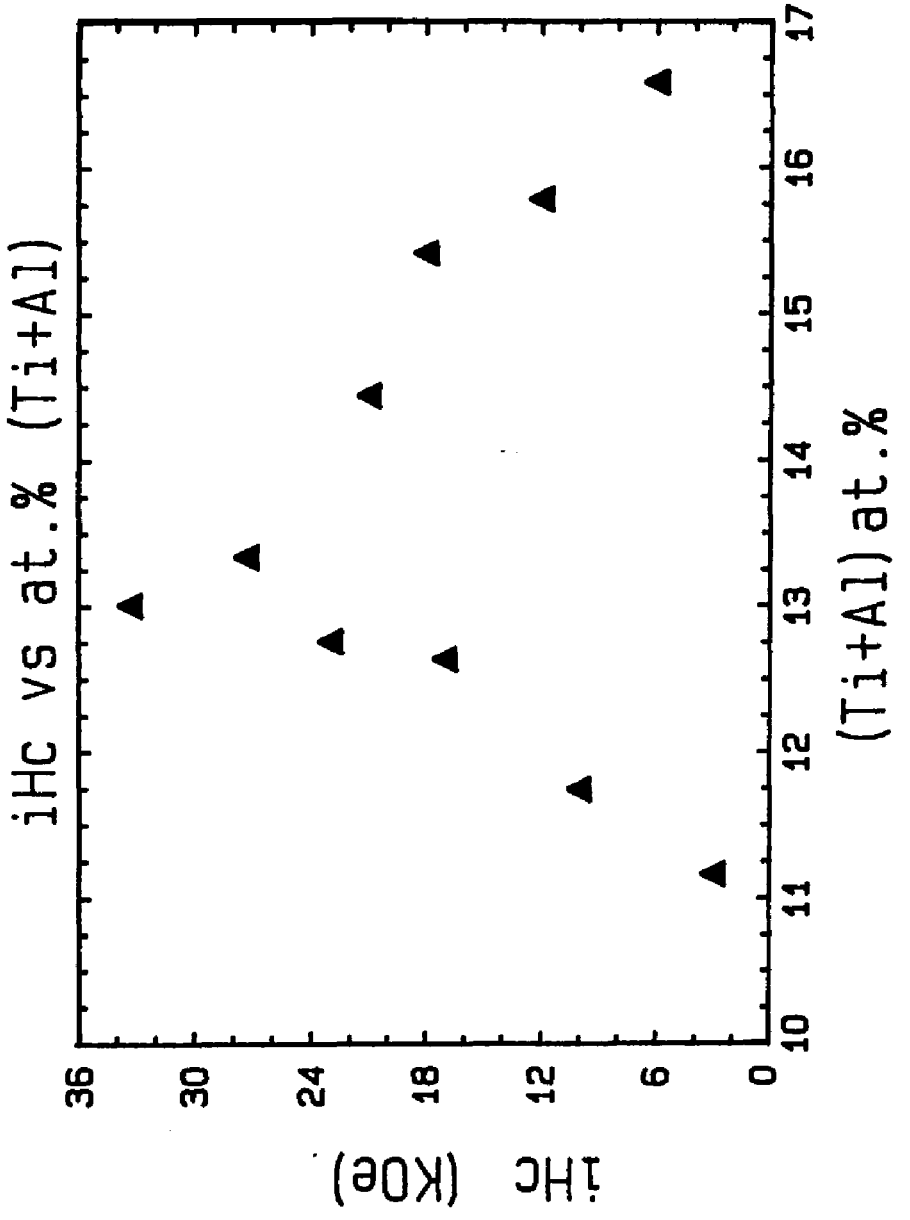
iHc vs at.% (Ti+Al)
iHc (KOe)
(Ti+Al) at.%
0
6
12
18
24
30
36
10
11
12
13
14
15
16
17

Fig. 4.33

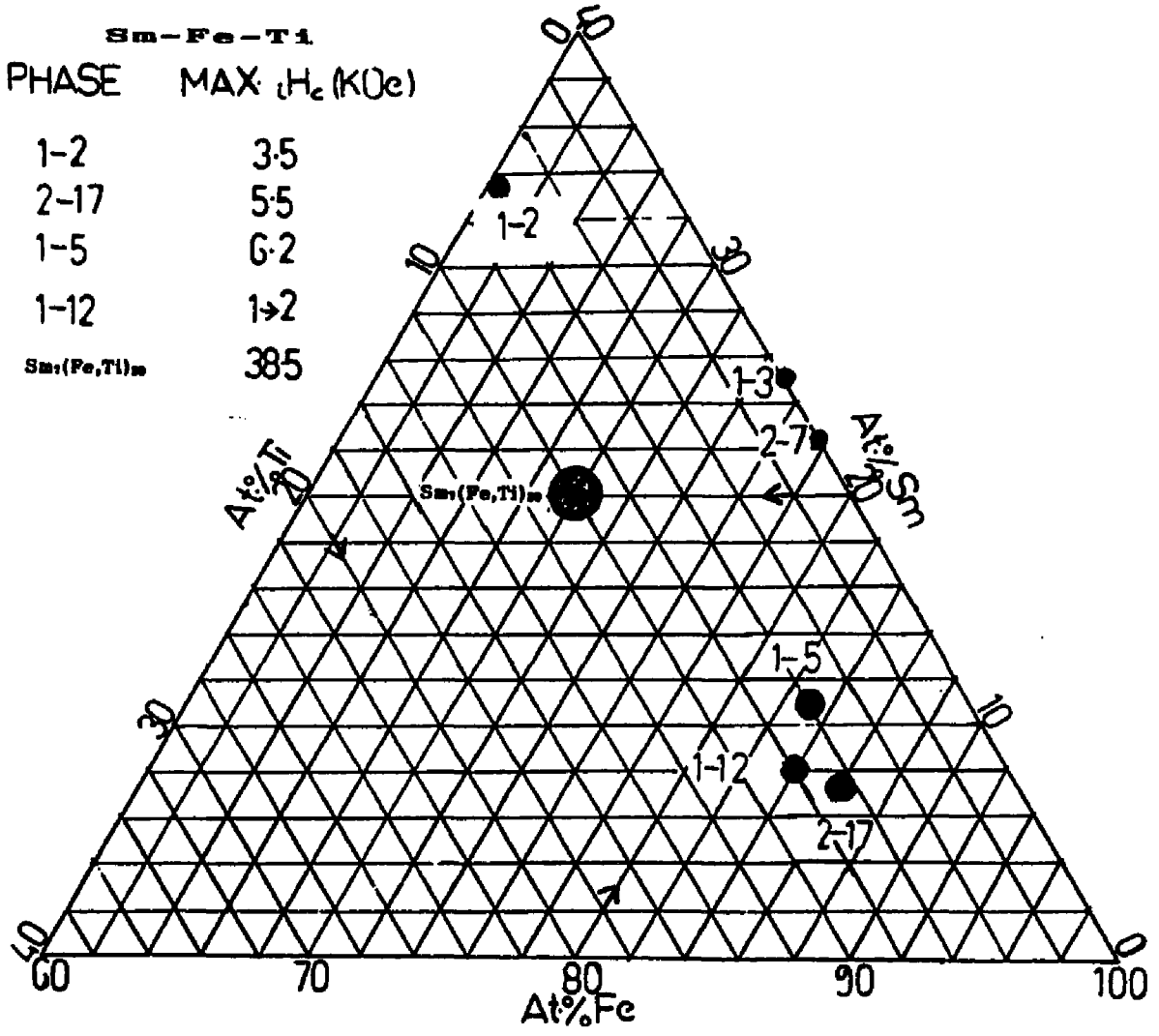
Sm-Fe-Ti
PHASE MAX. iHc (KOe)
1-2 3·5
2-17 5·5
1-5 6·2
1-12 1→2
Sm₂(Fe,Ti)₂₃ 3·5
1-2
1-3
2-7
1-5
1-12
2-17
Sm₂(Fe,Ti)₂₃
At%Ti
At%Sm
At%Fe
50
40
30
20
10
0
60
70
80
90
100

Fig. 4.34

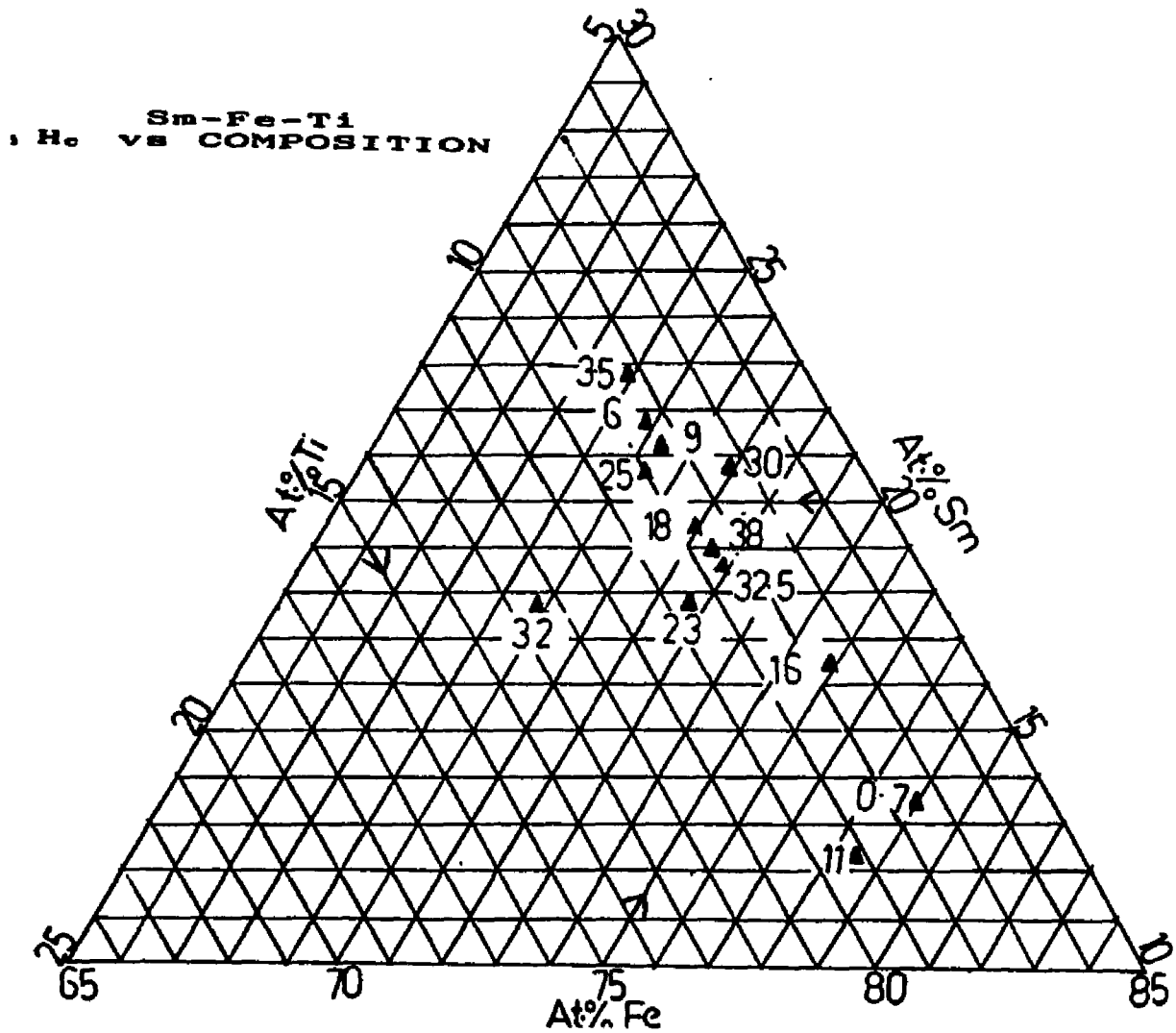
Sm-Fe-Ti
$_i H_c$ vs COMPOSITION
At% Ti
At% Sm
At% Fe
65
70
75
80
85
25
20
15
10
5
35
6
9
30
25
18
38
32.5
32
23
16
0·7
11
7

Fig. 4.35

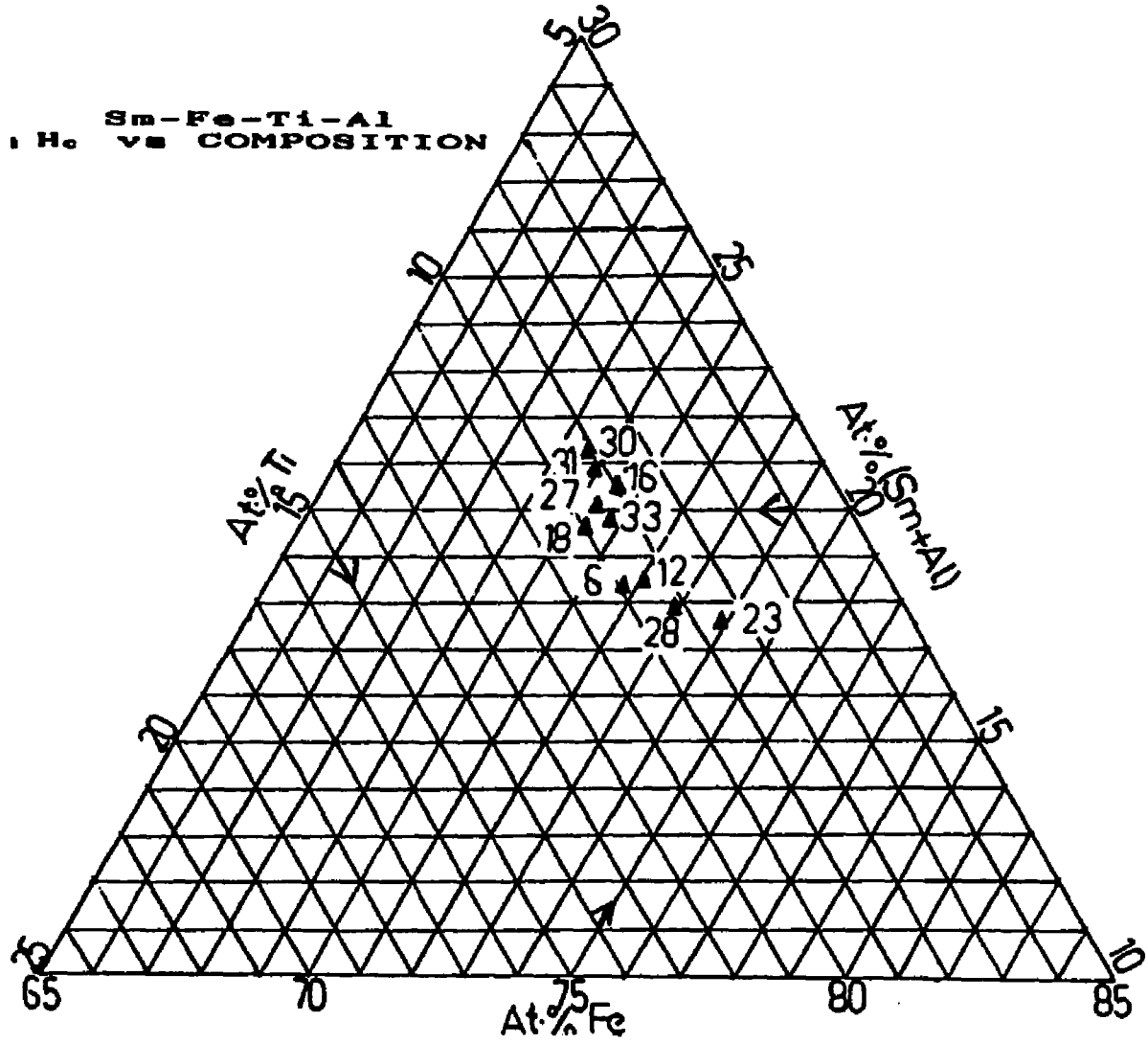
Sm-Fe-Ti-Al
i Hc vs COMPOSITION
At.% Ti
At.% (Sm+Al)
At.% Fe
30
25
20
15
10
5
65
70
75
80
85
31
30
27
16
33
18
6
12
28
23

Fig. 4.36

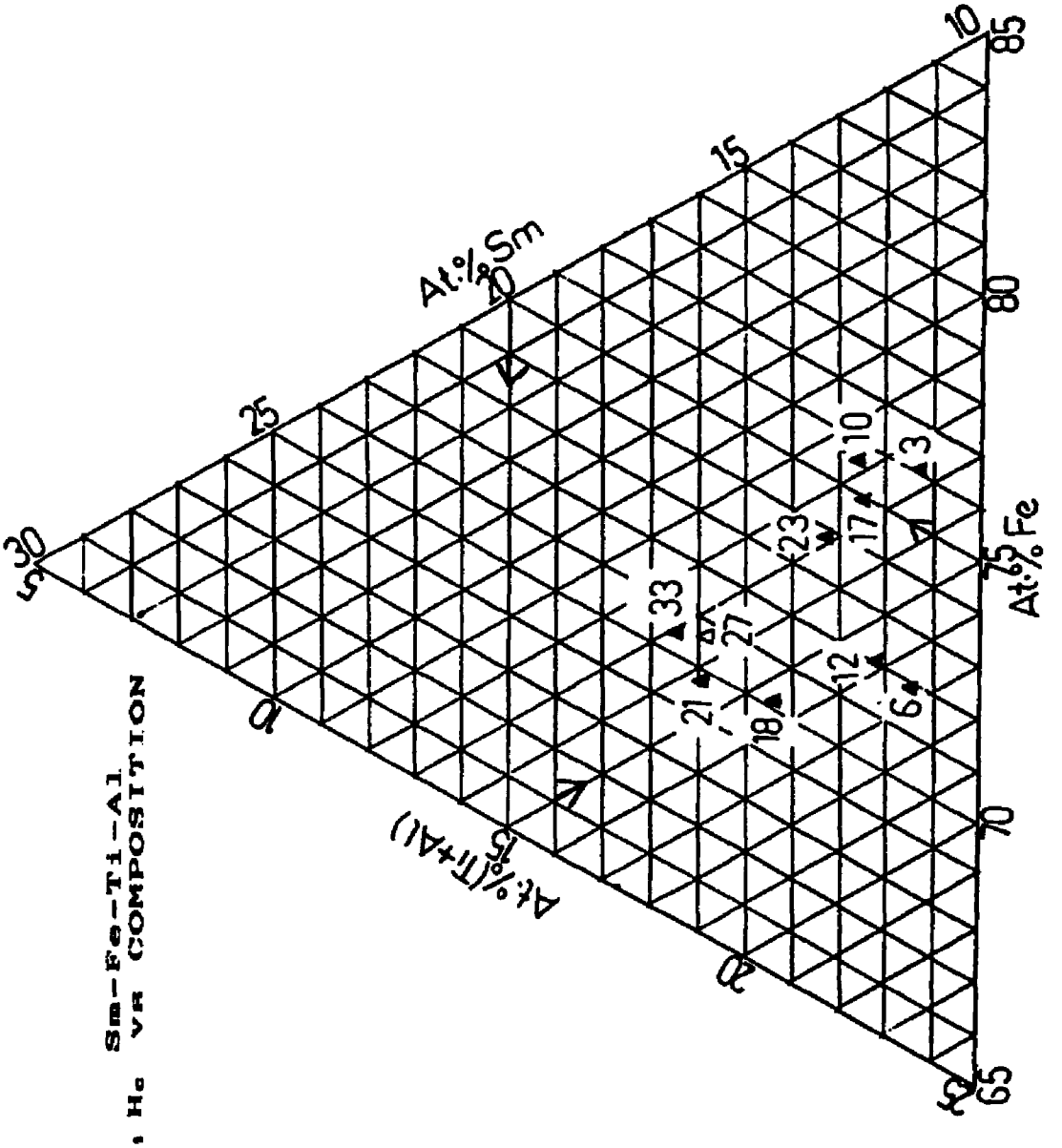
Sm-Fe-Ti-Al
$_i$H$_c$ vs COMPOSITION
At.% Sm
At.% Fe
At.% (Ti+Al)
P
Q
R
33
27
21
18
23
17
12
10
6
3

Fig. 4.37

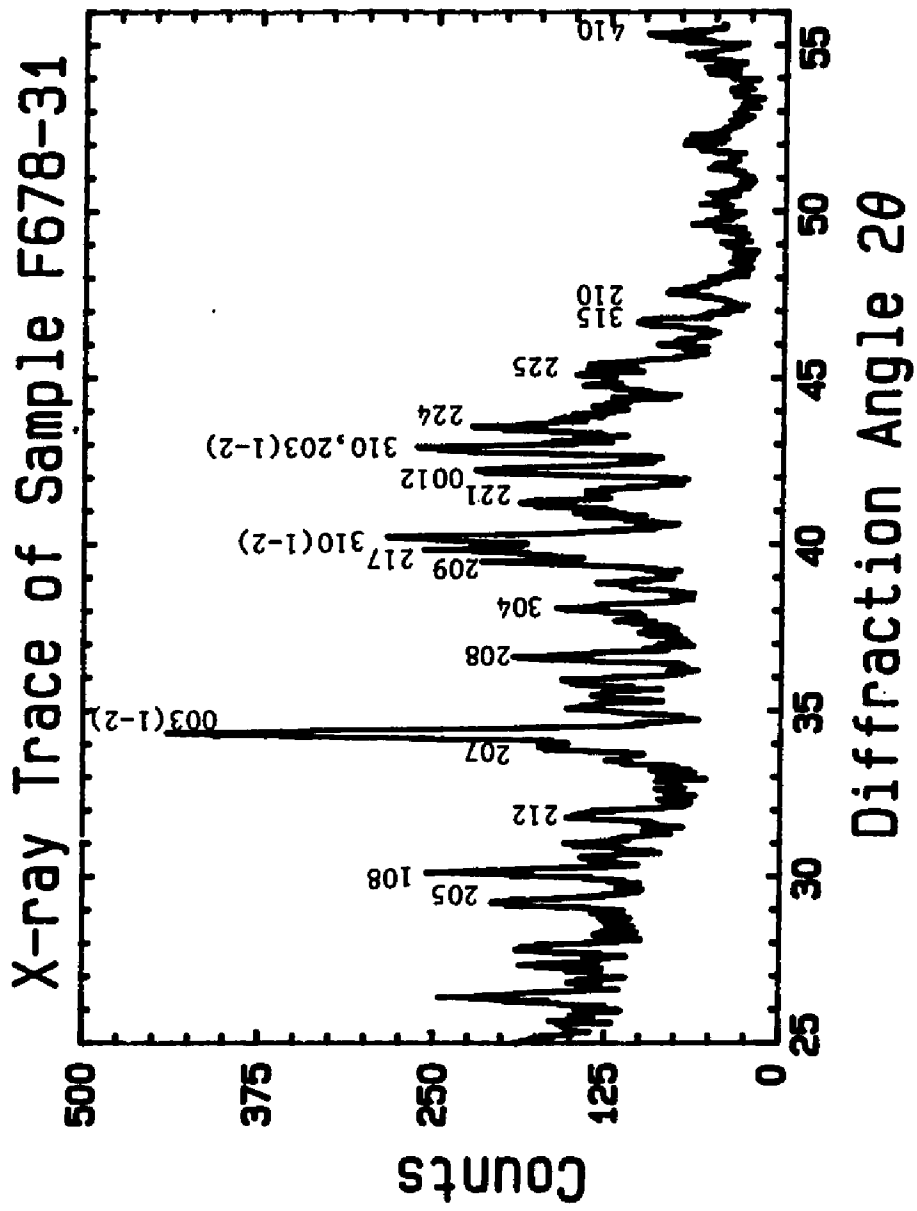
X-ray Trace of Sample F678-31
Counts
Diffraction Angle 2θ
500
375
250
125
0
25
30
35
40
45
50
55
410
315
210
225
224
310,203(1-2)
221
0012
217
310(1-2)
209
304
208
003(1-2)
207
212
205
108

Fig. 4.38

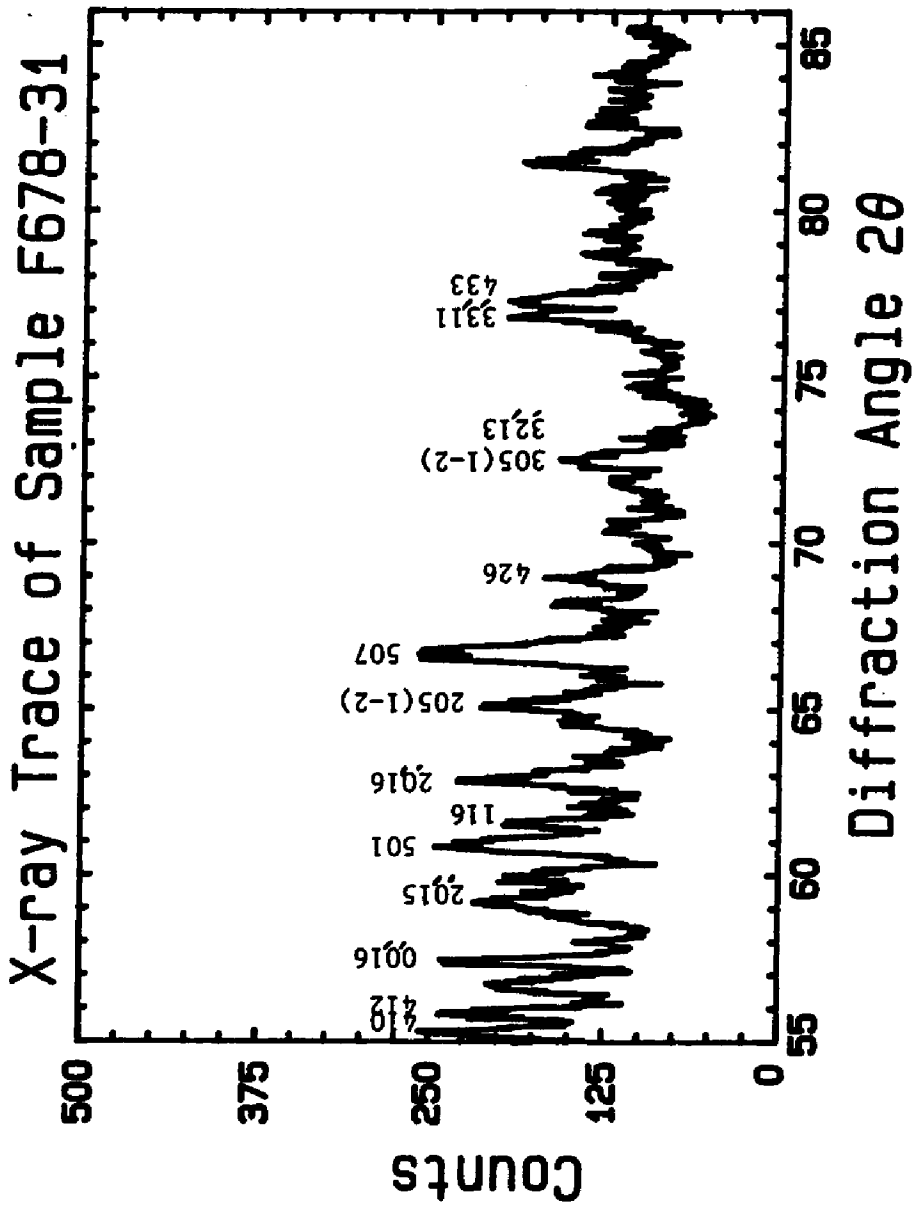
X-ray Trace of Sample F678-31
Counts
500
375
250
125
0
Diffraction Angle 2θ
55
60
65
70
75
80
85
410
412
00l6
20l5
501
116
20l6
205(1-2)
507
426
305(1-2)
32l3
33l1
433

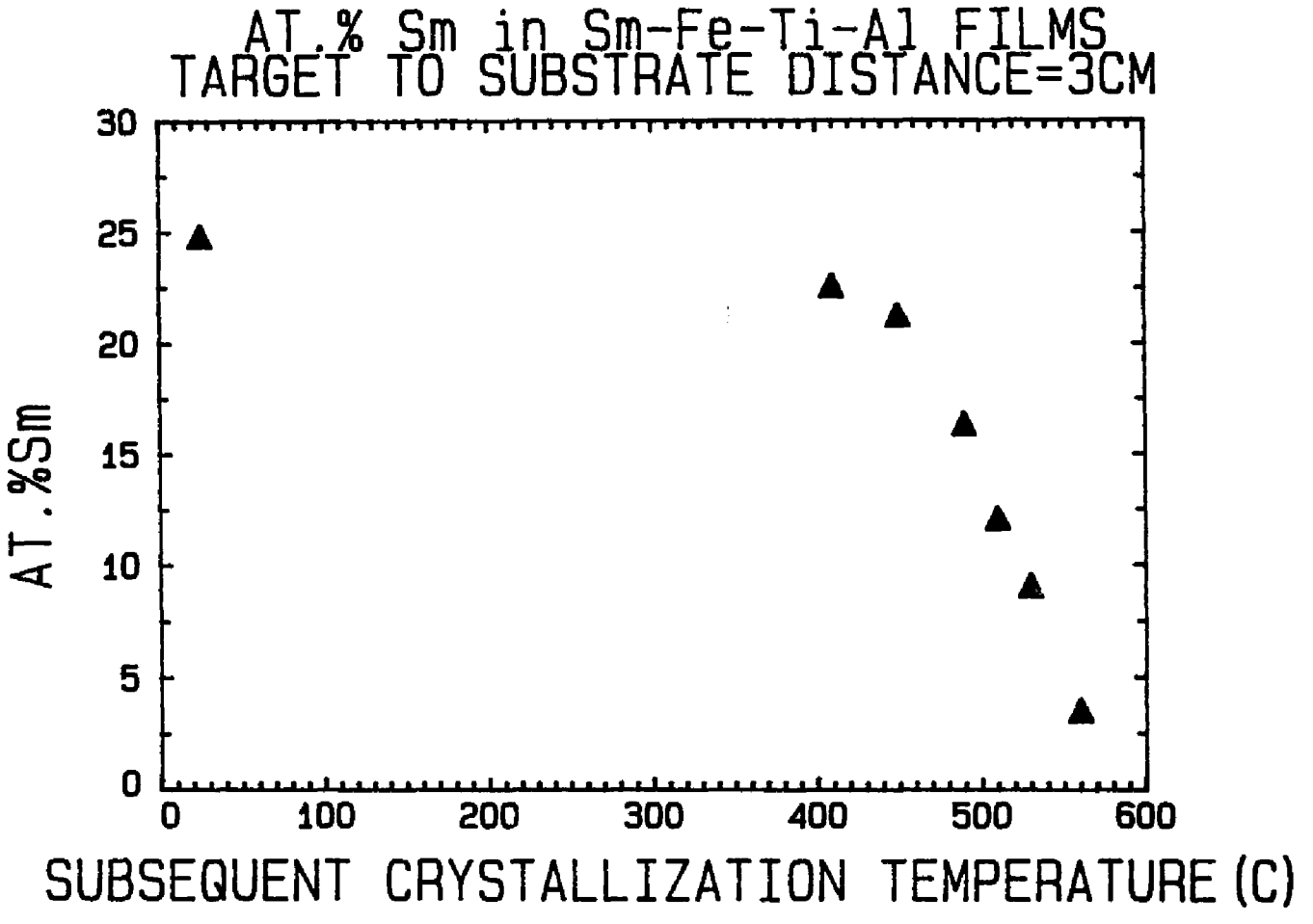
AT.% Sm in Sm-Fe-Ti-Al FILMS
TARGET TO SUBSTRATE DISTANCE=3CM
AT.%Sm
30
25
20
15
10
5
0
0
100
200
300
400
500
600
SUBSEQUENT CRYSTALLIZATION TEMPERATURE (C)

Fig. 4.39

Fig. 4.40

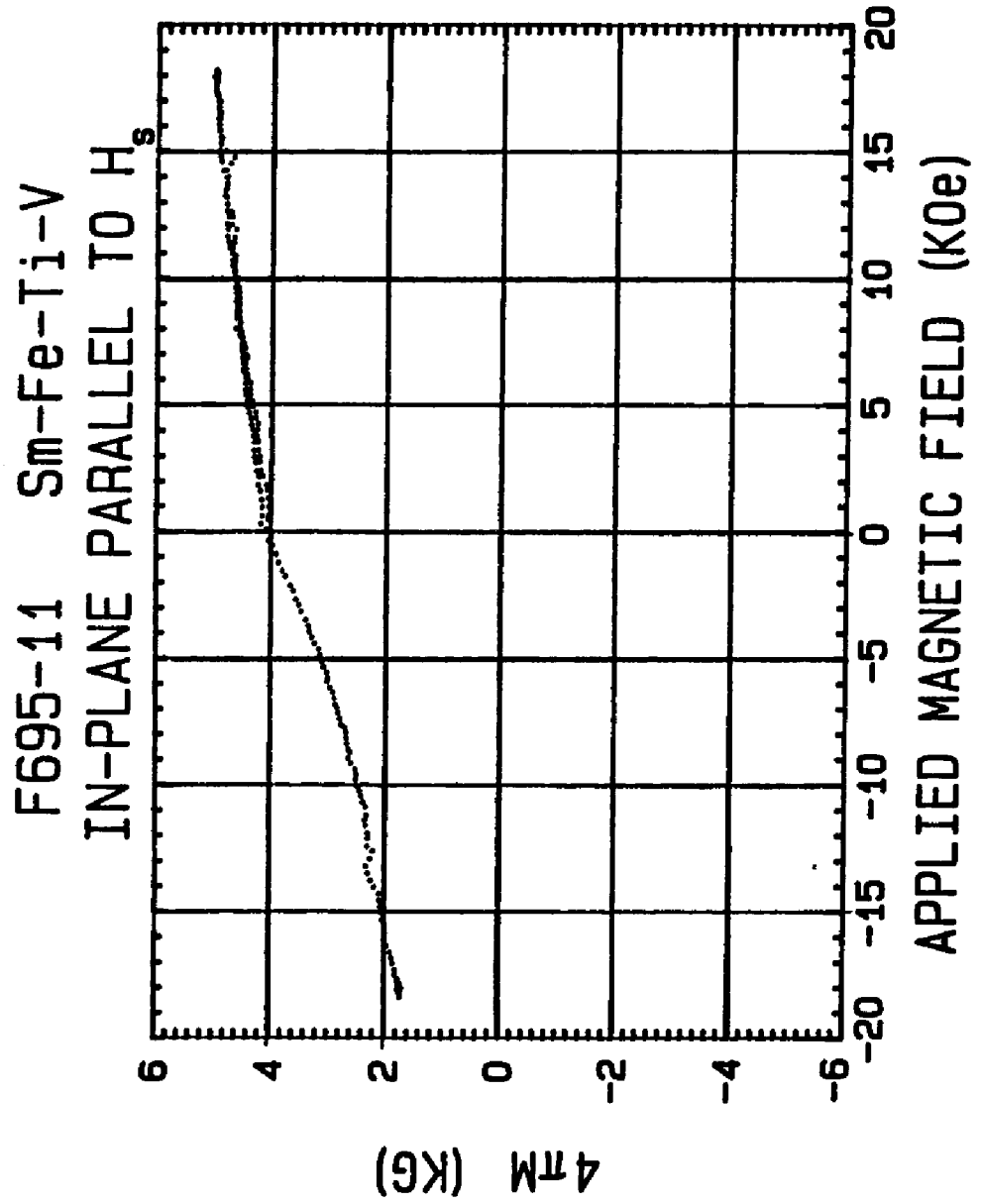
F695-11 Sm-Fe-Ti-V
IN-PLANE PARALLEL TO H_s
$4\pi M$ (KG)
APPLIED MAGNETIC FIELD (KOe)
6
4
2
0
-2
-4
-6
20
15
10
5
0
-5
-10
-15
-20

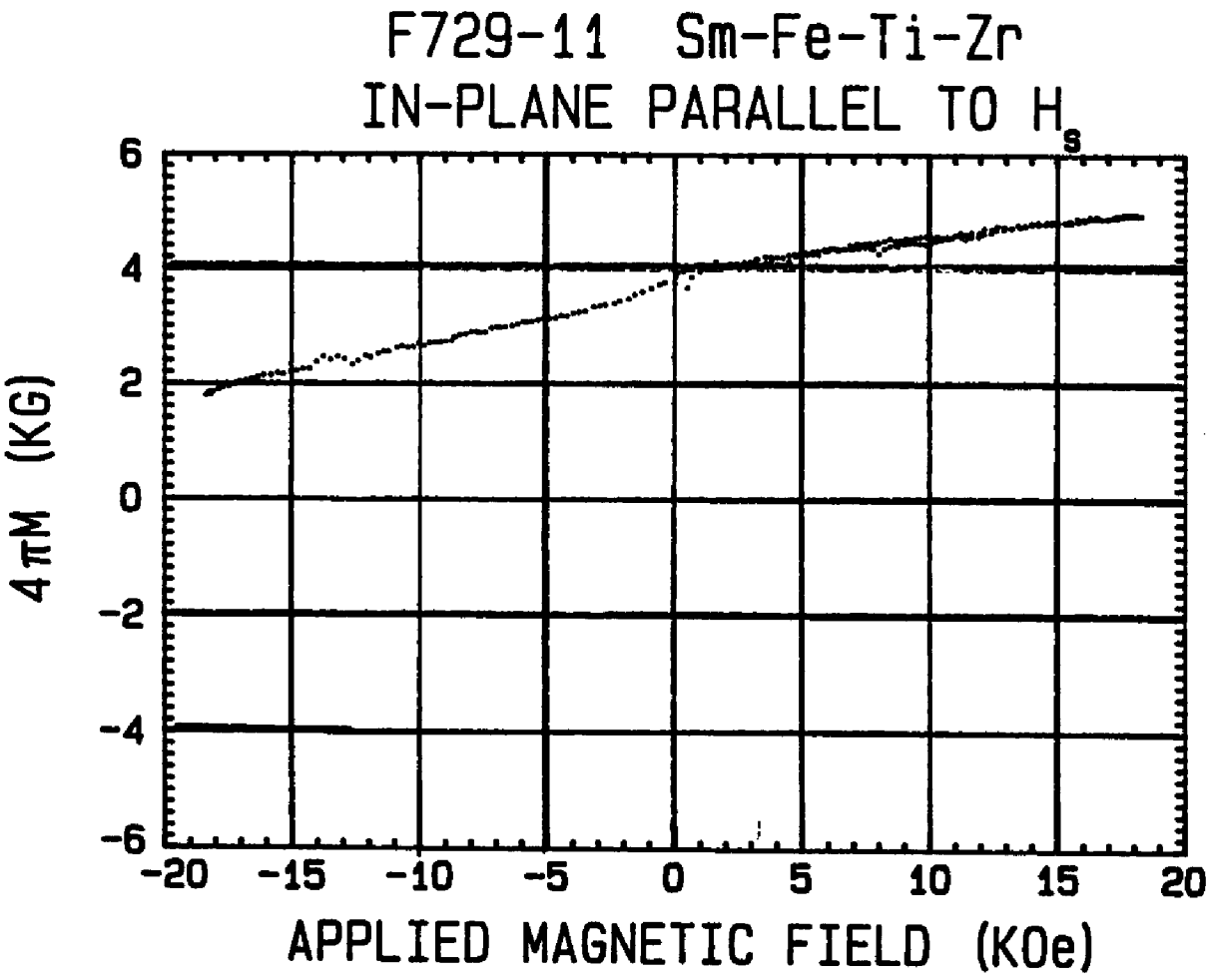
F729-11 Sm-Fe-Ti-Zr
IN-PLANE PARALLEL TO H
s
4πM (KG)
6
4
2
0
-2
-4
-6
-20
-15
-10
-5
0
5
10
15
20
APPLIED MAGNETIC FIELD (KOe)

Fig. 4.41

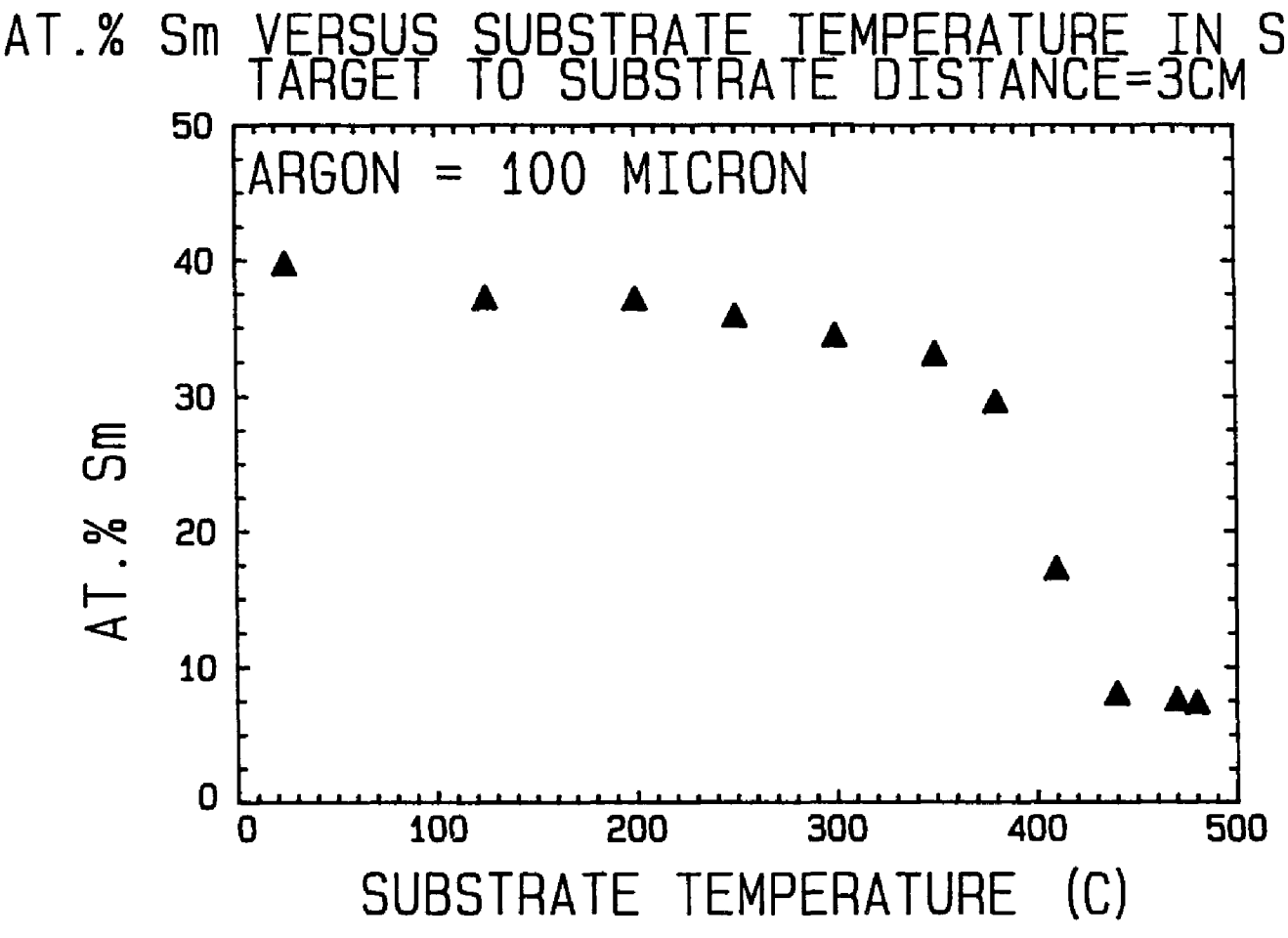
AT.% Sm VERSUS SUBSTRATE TEMPERATURE IN Sm-Fe-Ti FILMS
TARGET TO SUBSTRATE DISTANCE=3CM
ARGON = 100 MICRON
AT.% Sm
SUBSTRATE TEMPERATURE (C)
0
10
20
30
40
50
0
100
200
300
400
500

Fig. 5.1

DEPOSITION RATE VERSUS SUBSTRATE TEMPERATURE

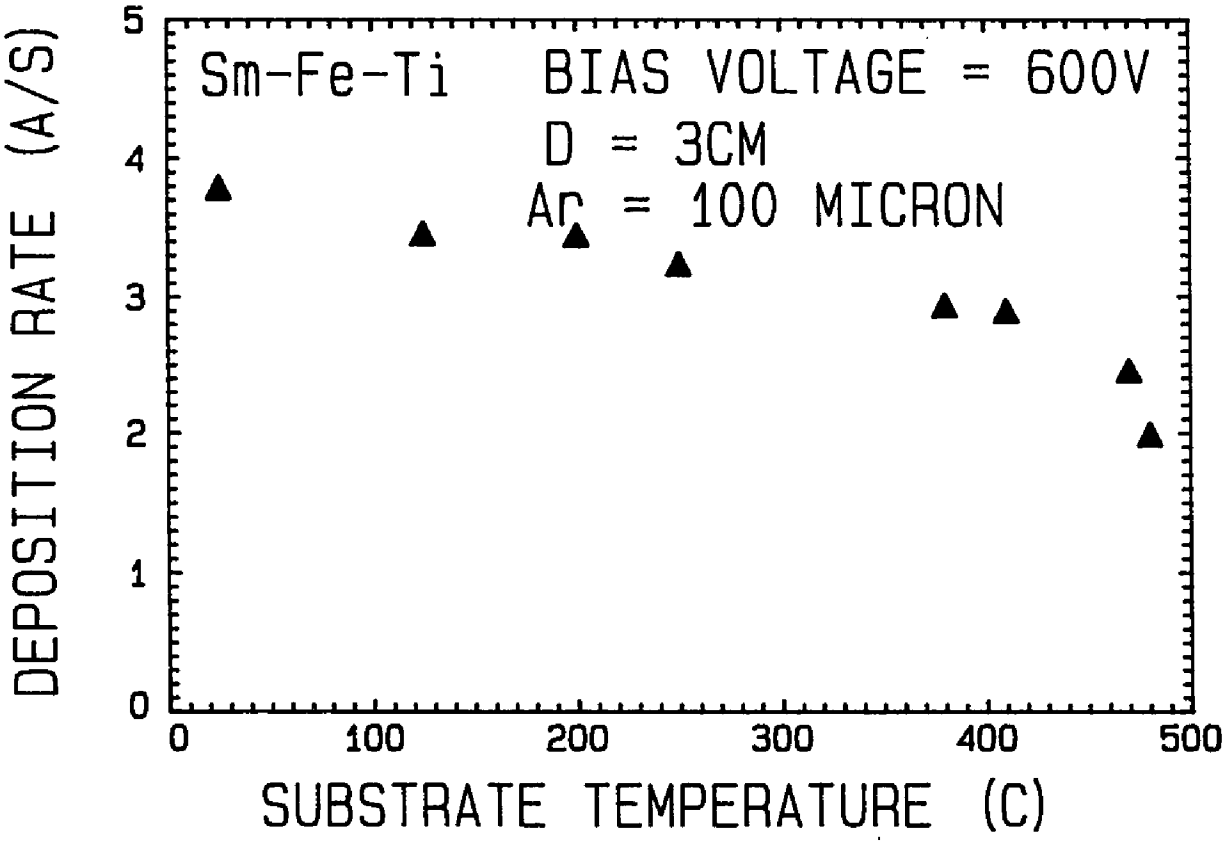

Fig. 5.2

DEPOSITION RATE VERSUS TARGET TO SUBSTRATE DISTANCE

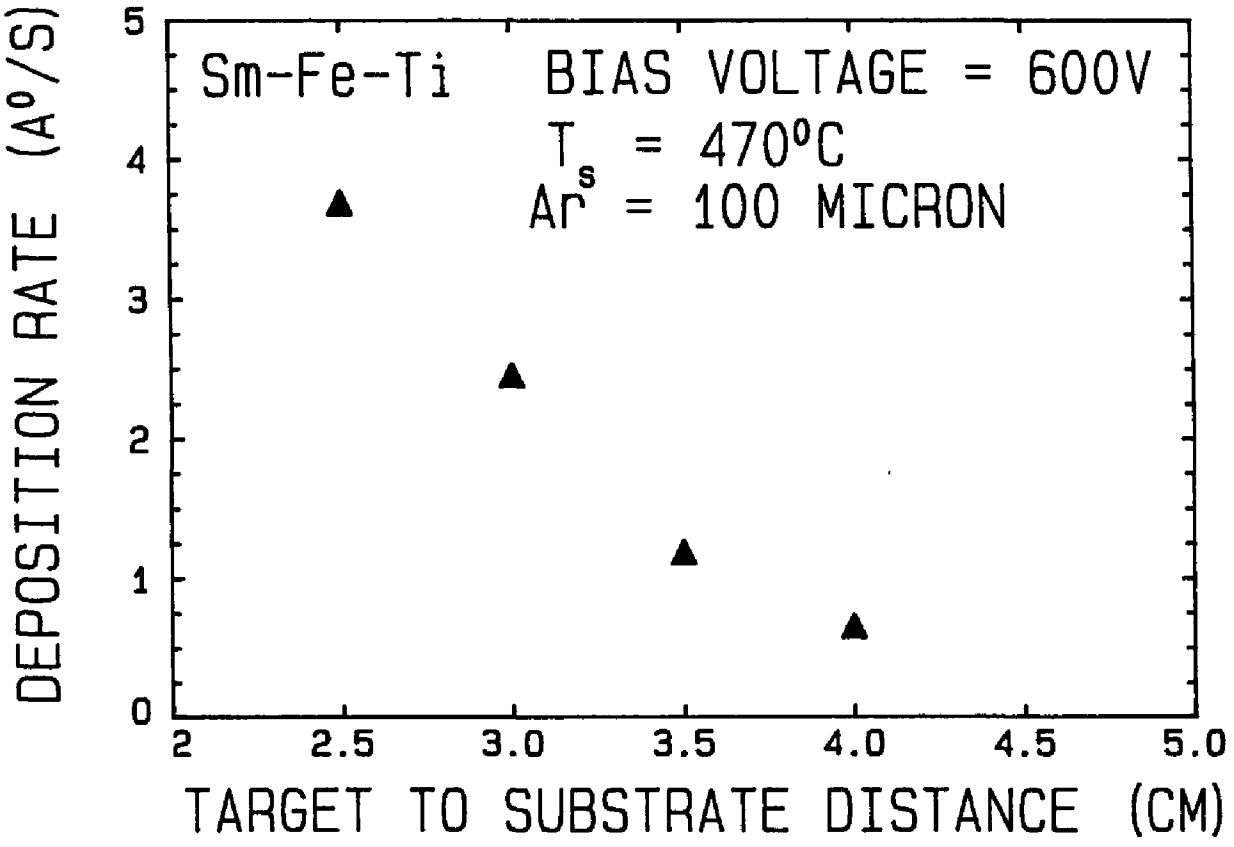

Fig. 5.3

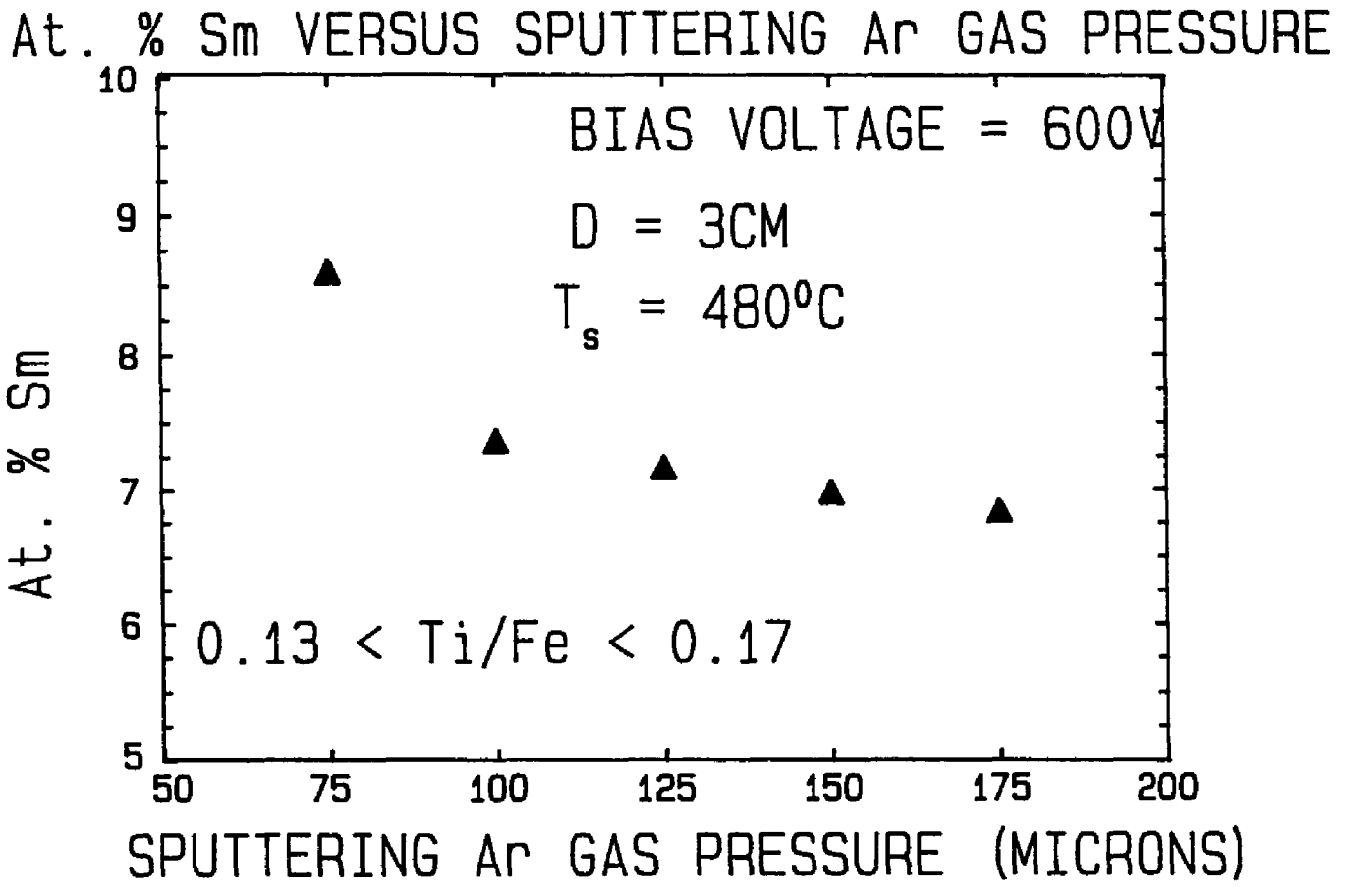
At. % Sm VERSUS SPUTTERING Ar GAS PRESSURE
BIAS VOLTAGE = 600V
D = 3CM
T_s = 480°C
0.13 < Ti/Fe < 0.17
At. % Sm
10
9
8
7
6
5
50
75
100
125
150
175
200
SPUTTERING Ar GAS PRESSURE (MICRONS)

Fig. 5.4

At. % Sm VERSUS TARGET TO SUBSTRATE DISTANCE

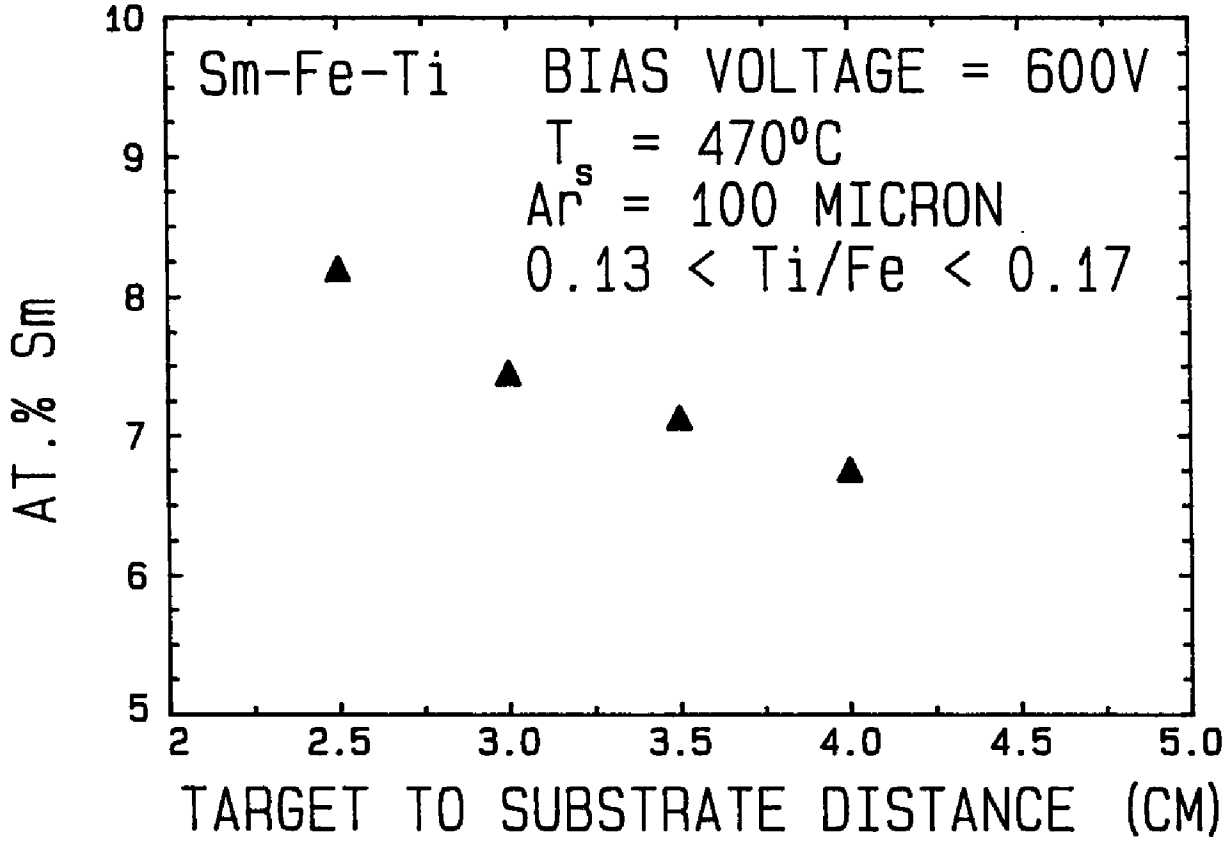

Fig. 5.5

Fig. 5.6

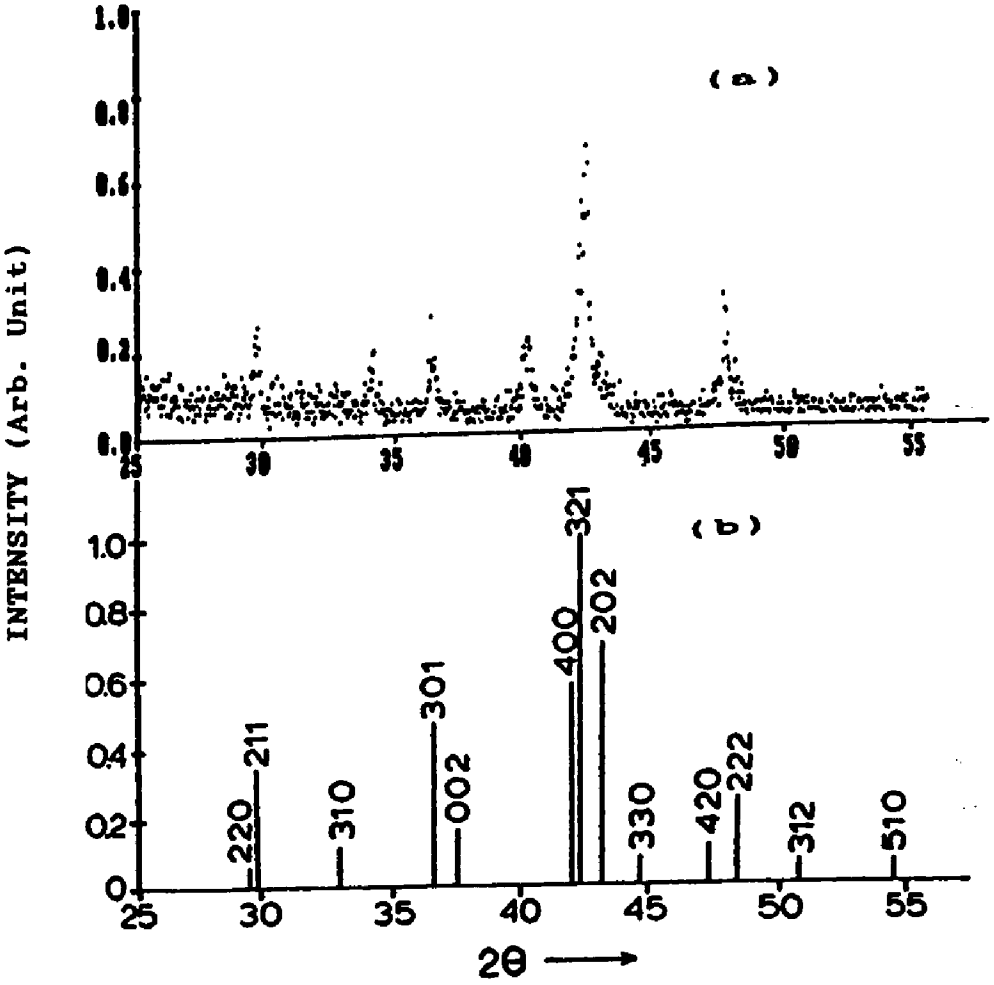
INTENSITY (Arb. Unit)
(a)
(b)
1.0
0.8
0.6
0.4
0.2
0
25
30
35
40
45
50
55
2θ
220
211
310
301
002
400
321
202
330
420
222
312
510

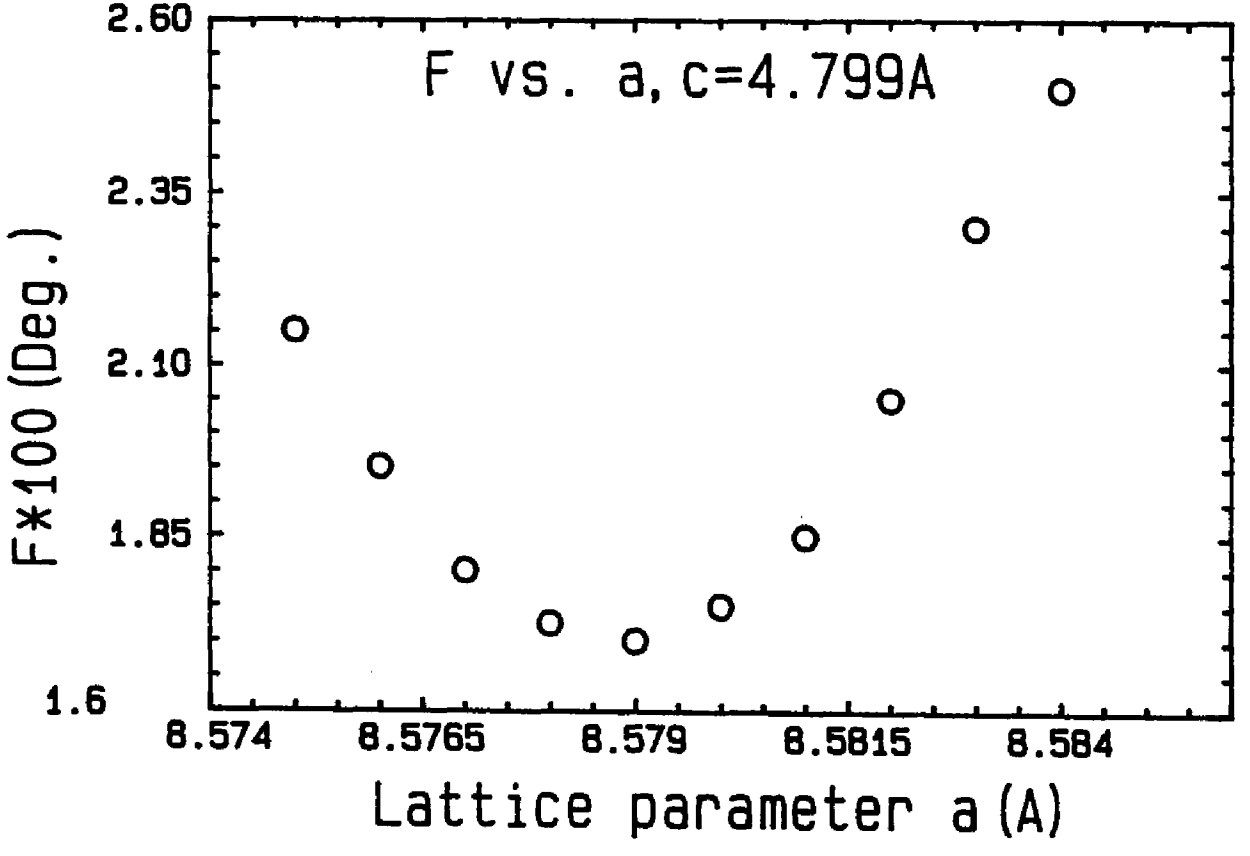
F vs. a, c=4.799A
F*100 (Deg.)
2.60
2.35
2.10
1.85
1.6
8.574
8.5765
8.579
8.5815
8.584
Lattice parameter a (A)

Fig. 5.7

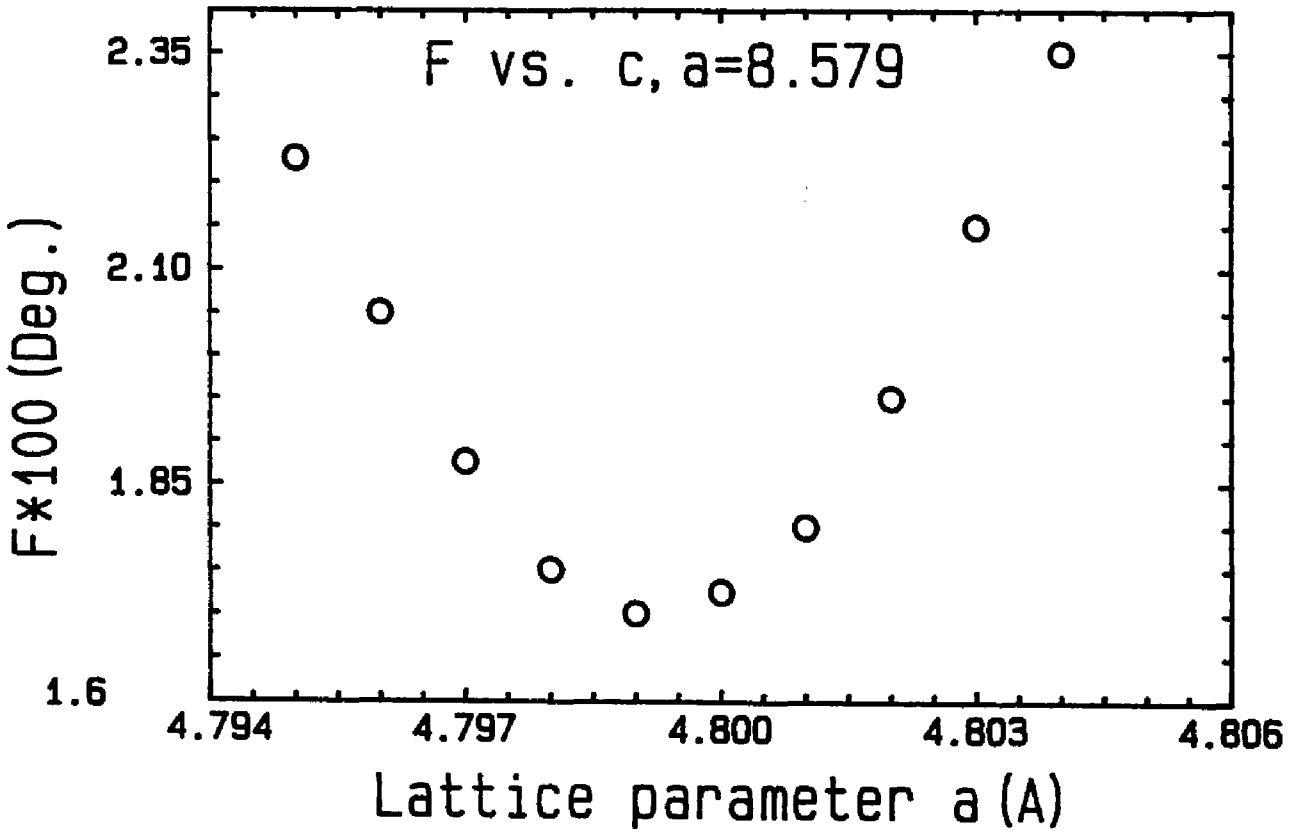
F vs. c, a=8.579
F*100 (Deg.)
2.35
2.10
1.85
1.6
4.794
4.797
4.800
4.803
4.806
Lattice parameter a (A)

Fig. 5.8

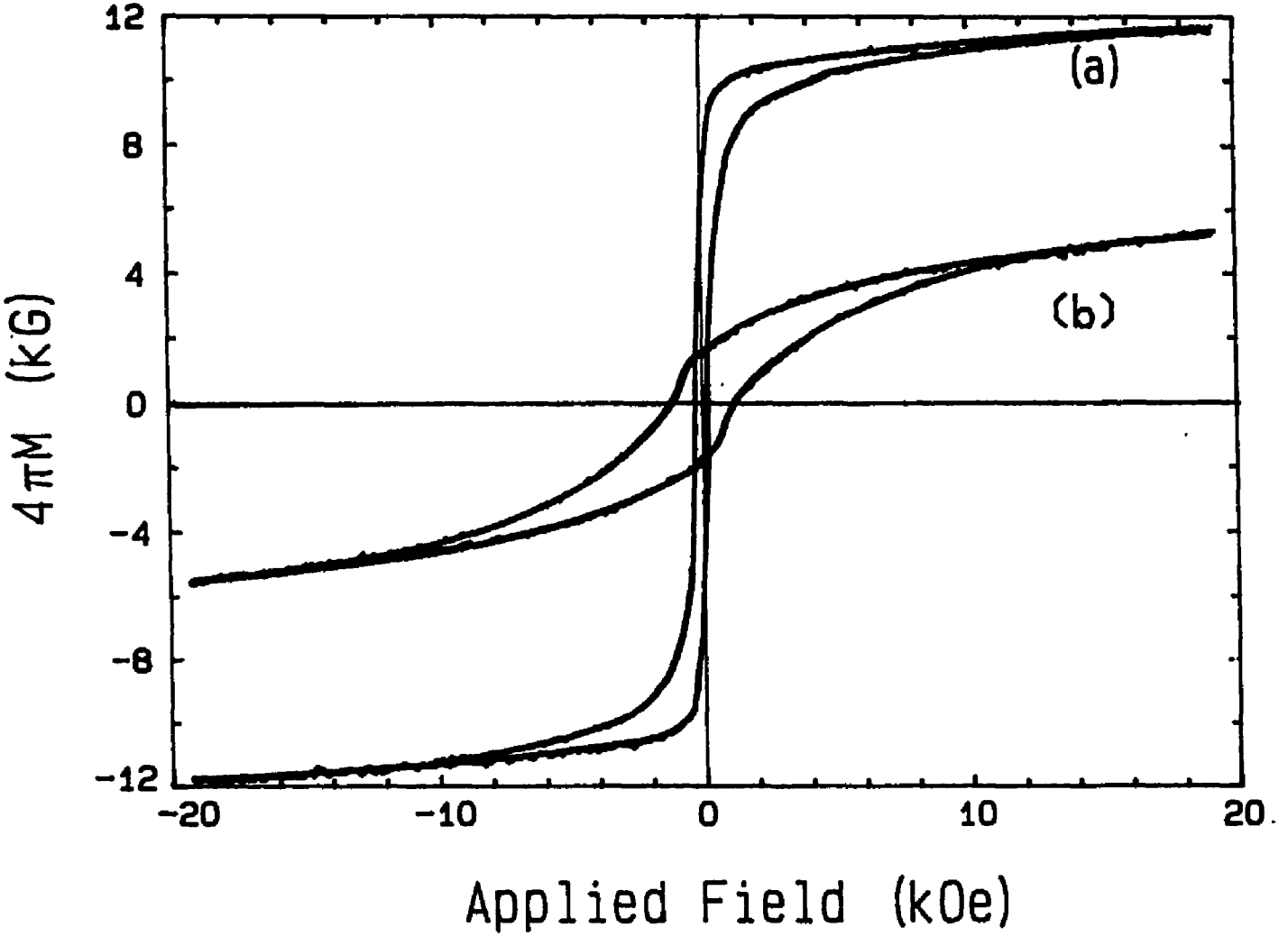

Fig. 5.9

Fig. 5.10

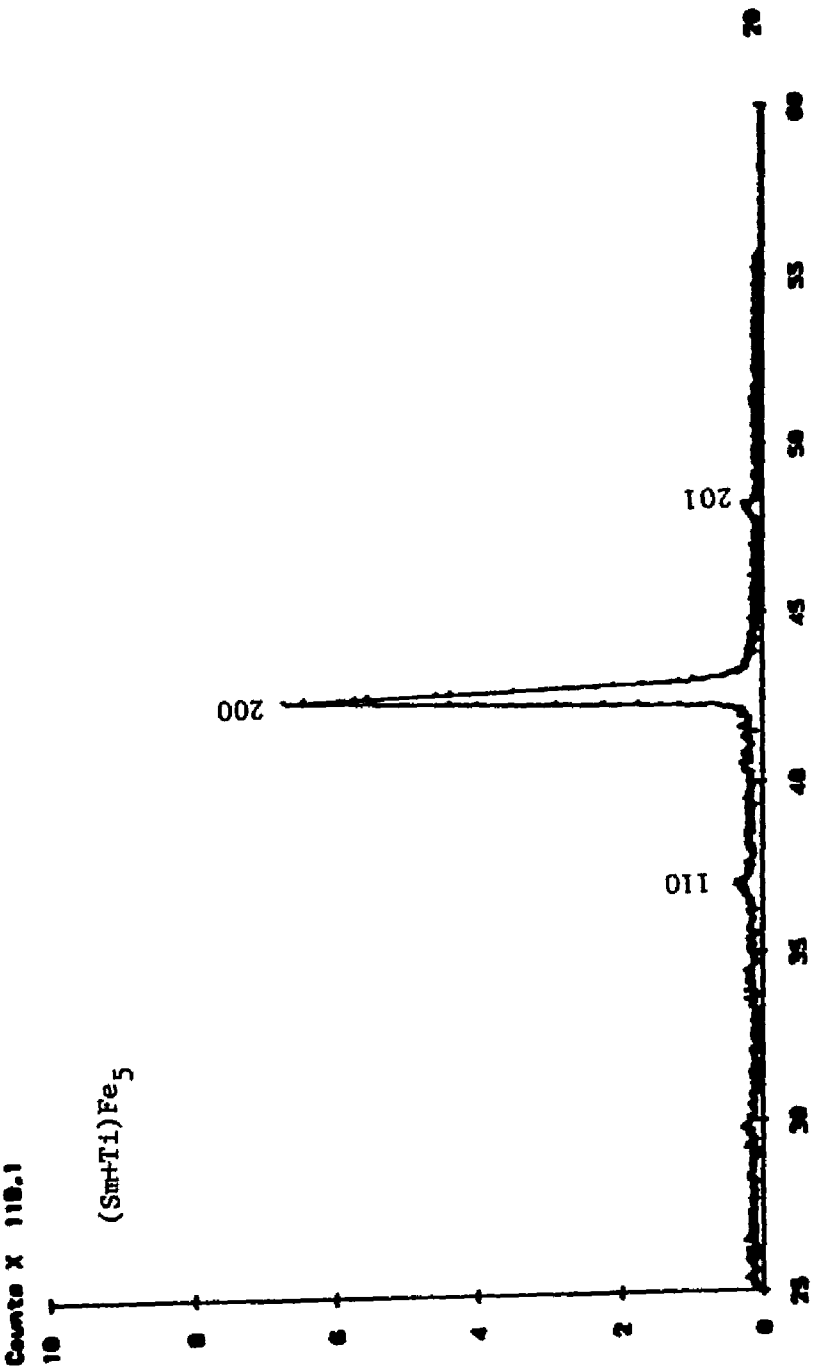

Fig. 5.11

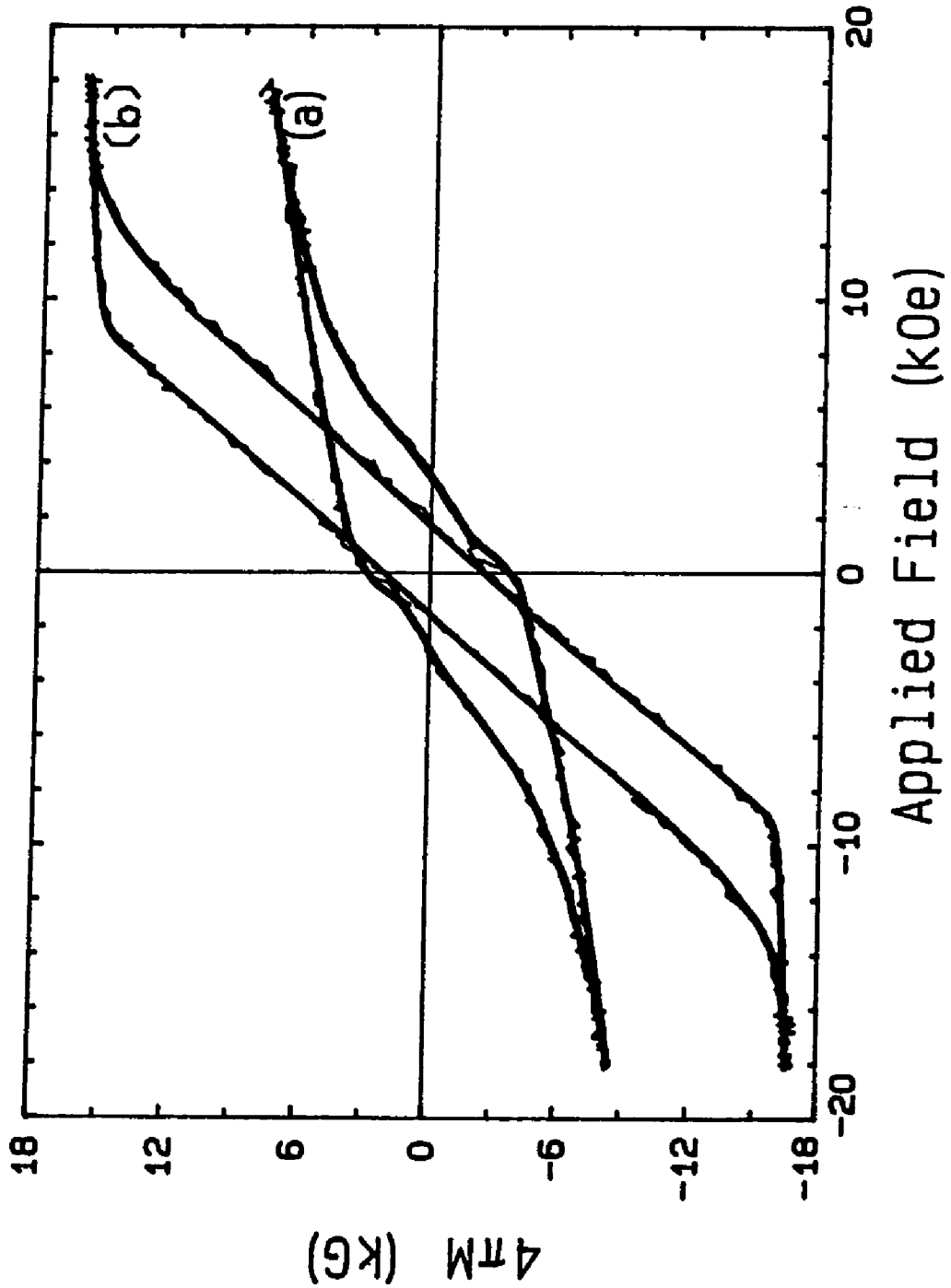

Fig. 5.12

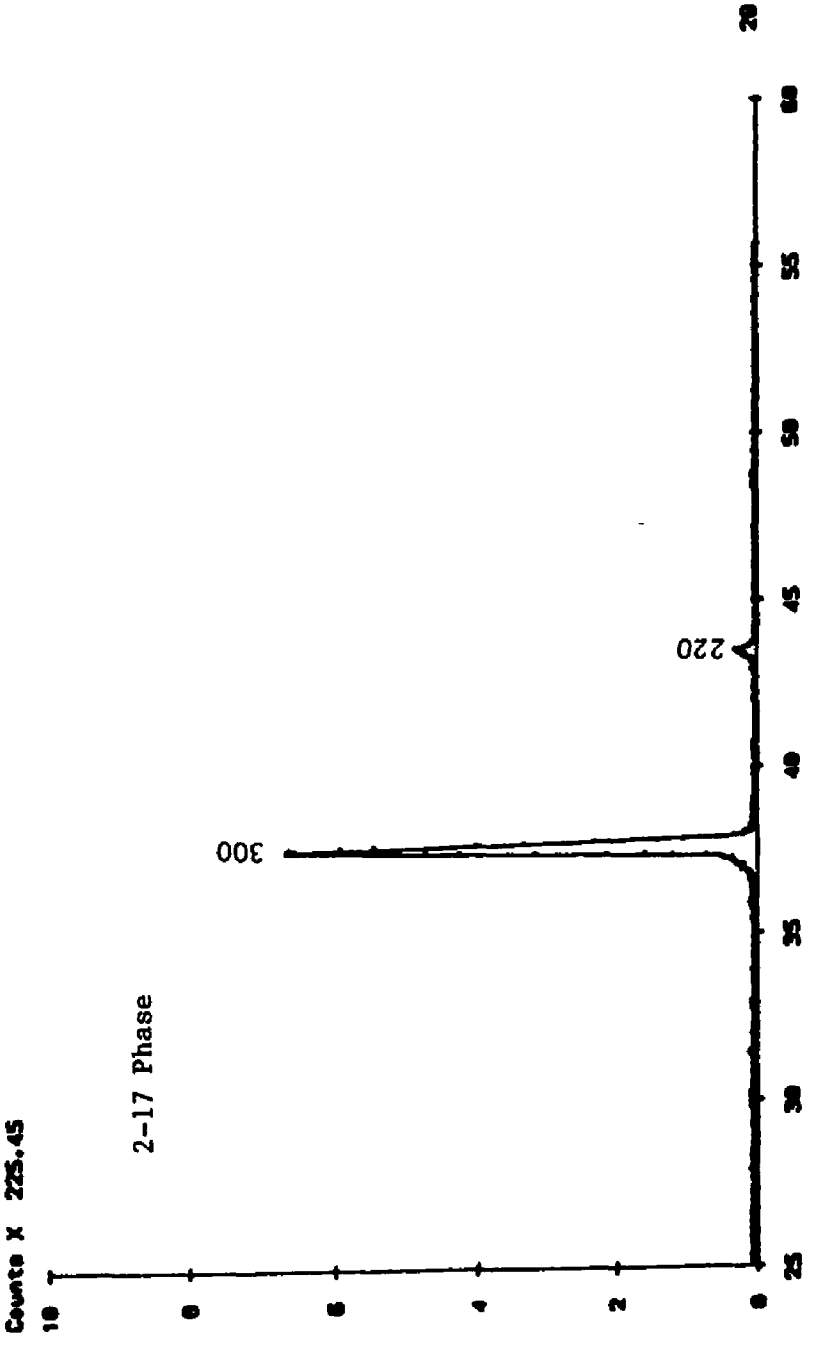
2θ
25
30
35
40
45
50
55
60
300
220
2-17 Phase
Counts X 225.45
0
2
4
6
8
10

Fig. 5.13

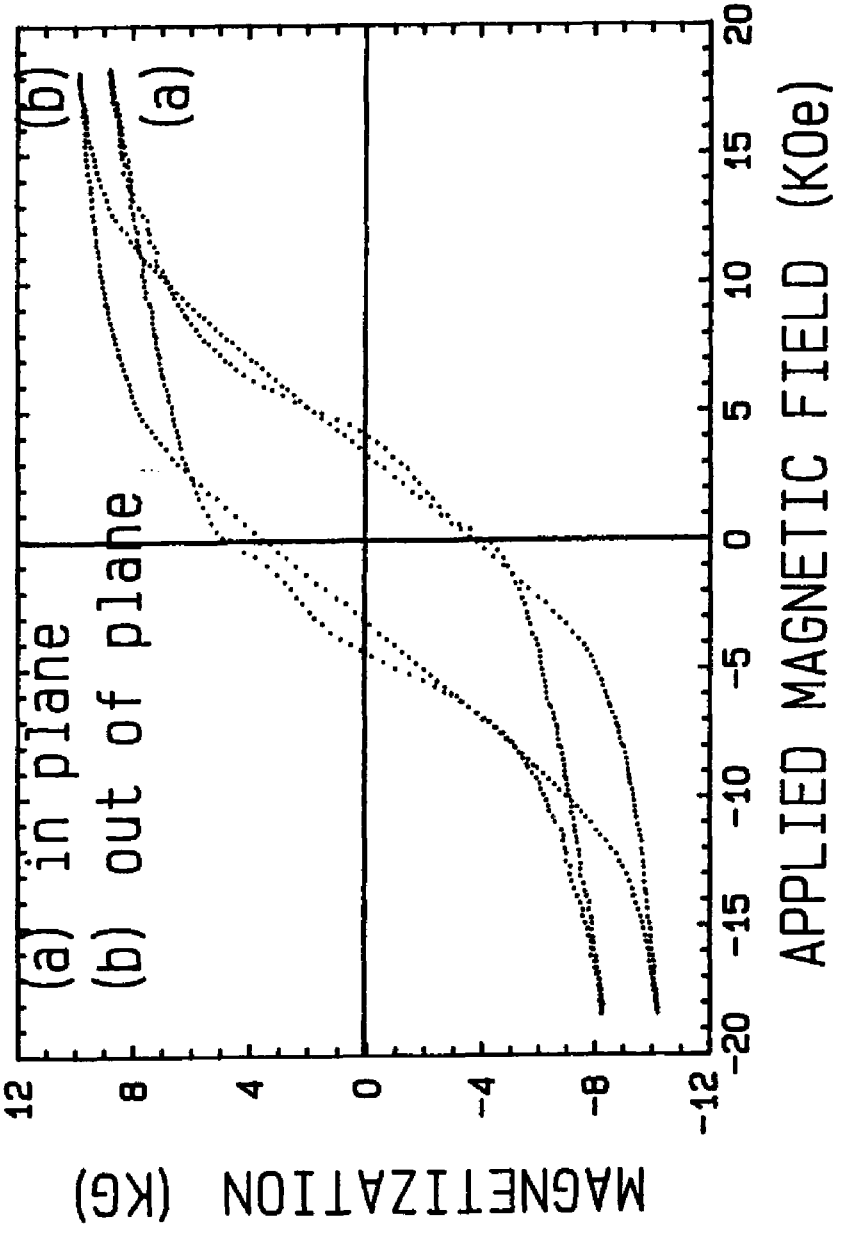
(a) in plane
(b) out of plane
(b)
(a)
MAGNETIZATION (KG)
APPLIED MAGNETIC FIELD (KOe)
12
8
4
0
-4
-8
-12
20
15
10
5
0
-5
-10
-15
-20

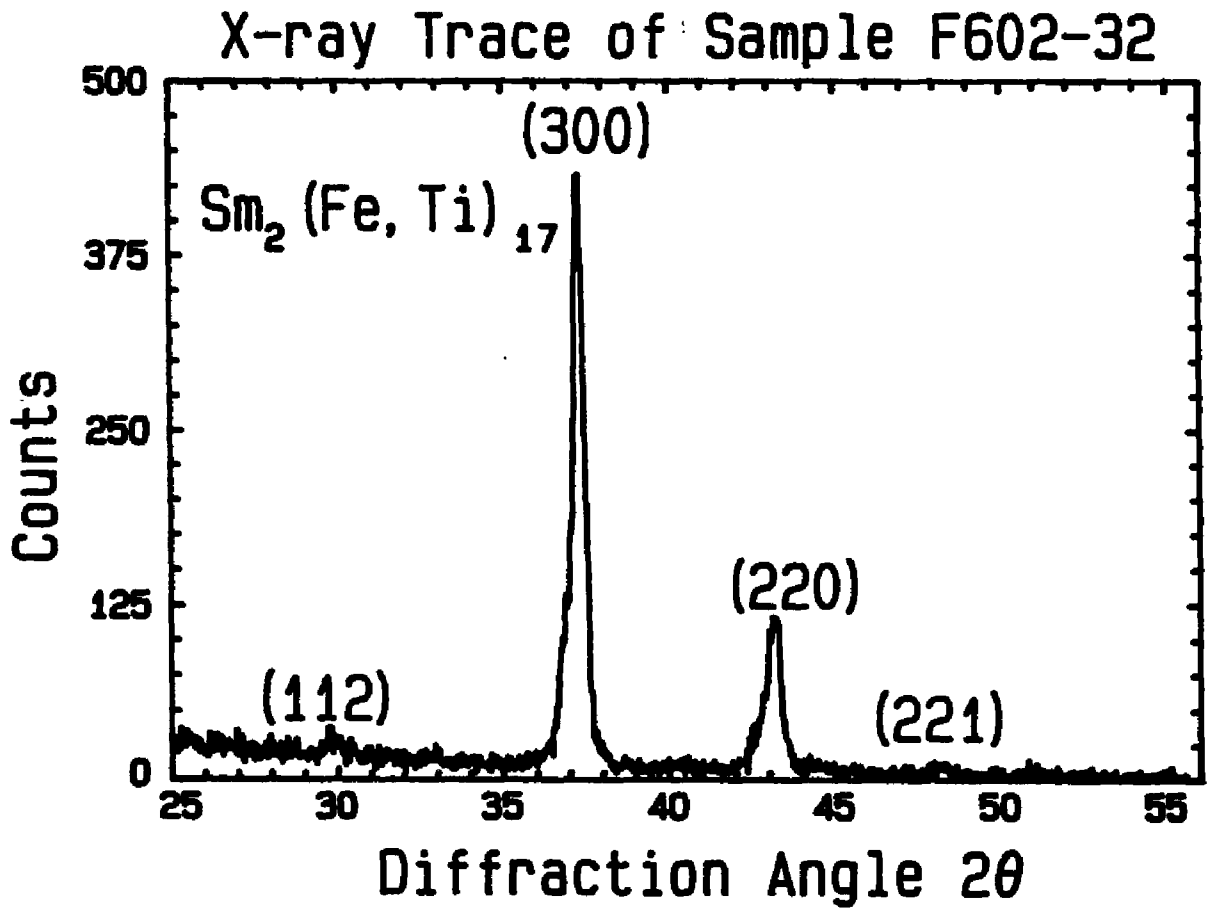
X-ray Trace of Sample F602-32
500
375
250
125
0
Counts
(300)
Sm2 (Fe, Ti) 17
(220)
(112)
(221)
25
30
35
40
45
50
55
Diffraction Angle 2θ

Fig. 5.14

Fig. 5.15

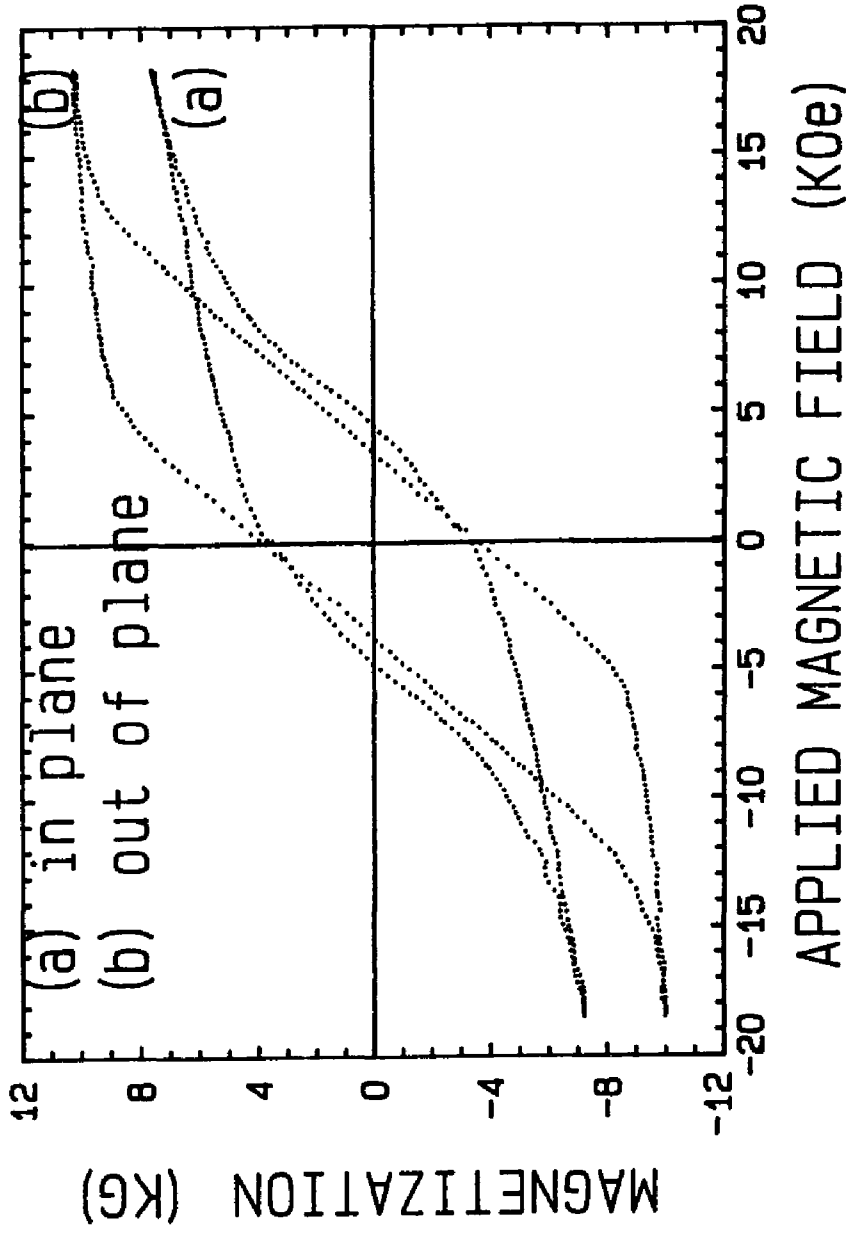
(a) in plane
(b) out of plane
(a)
(b)
MAGNETIZATION (KG)
APPLIED MAGNETIC FIELD (KOe)
12
8
4
0
-4
-8
-12
20
15
10
5
0
-5
-10
-15
-20

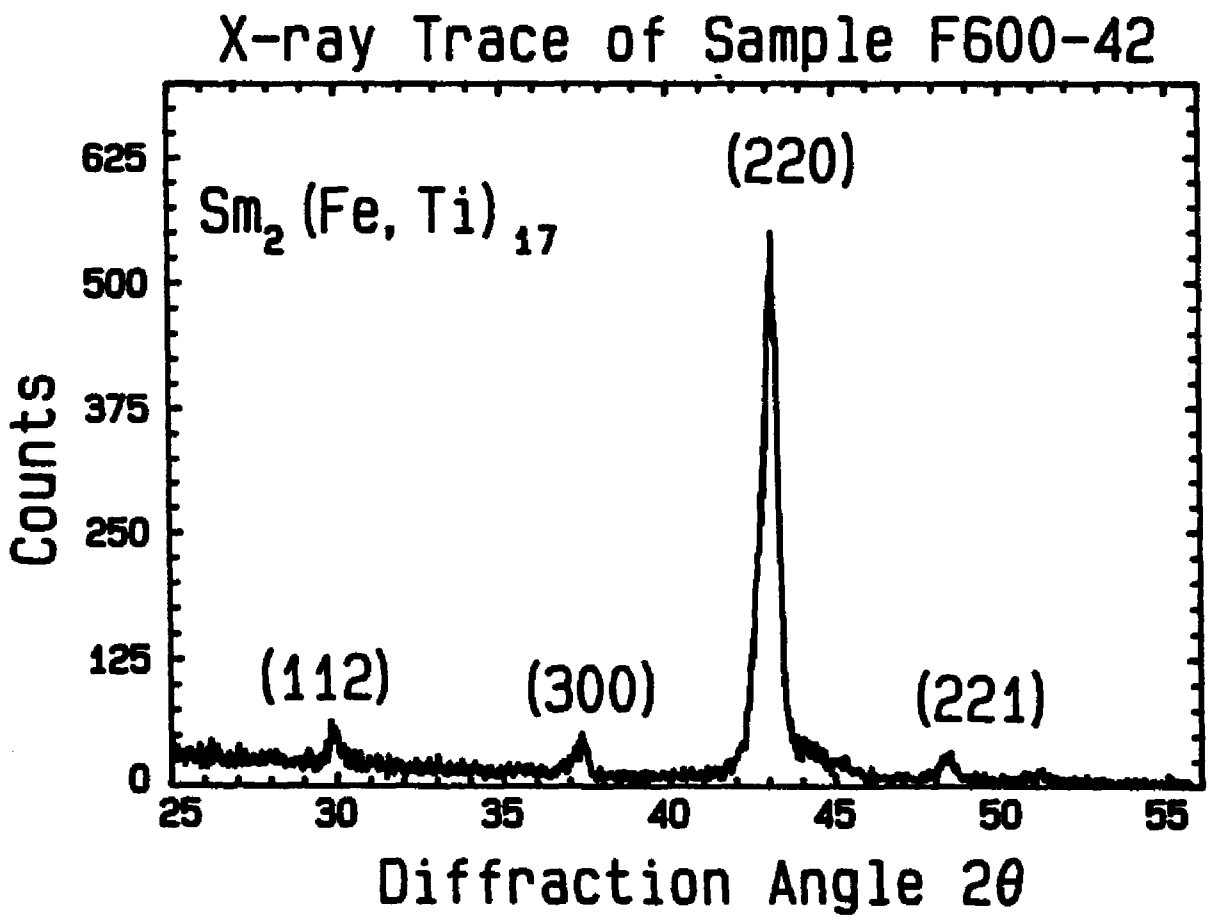
X-ray Trace of Sample F600-42
Sm2 (Fe, Ti) 17
(220)
(112)
(300)
(221)
Counts
625
500
375
250
125
0
25
30
35
40
45
50
55
Diffraction Angle 2θ

Fig. 5.16

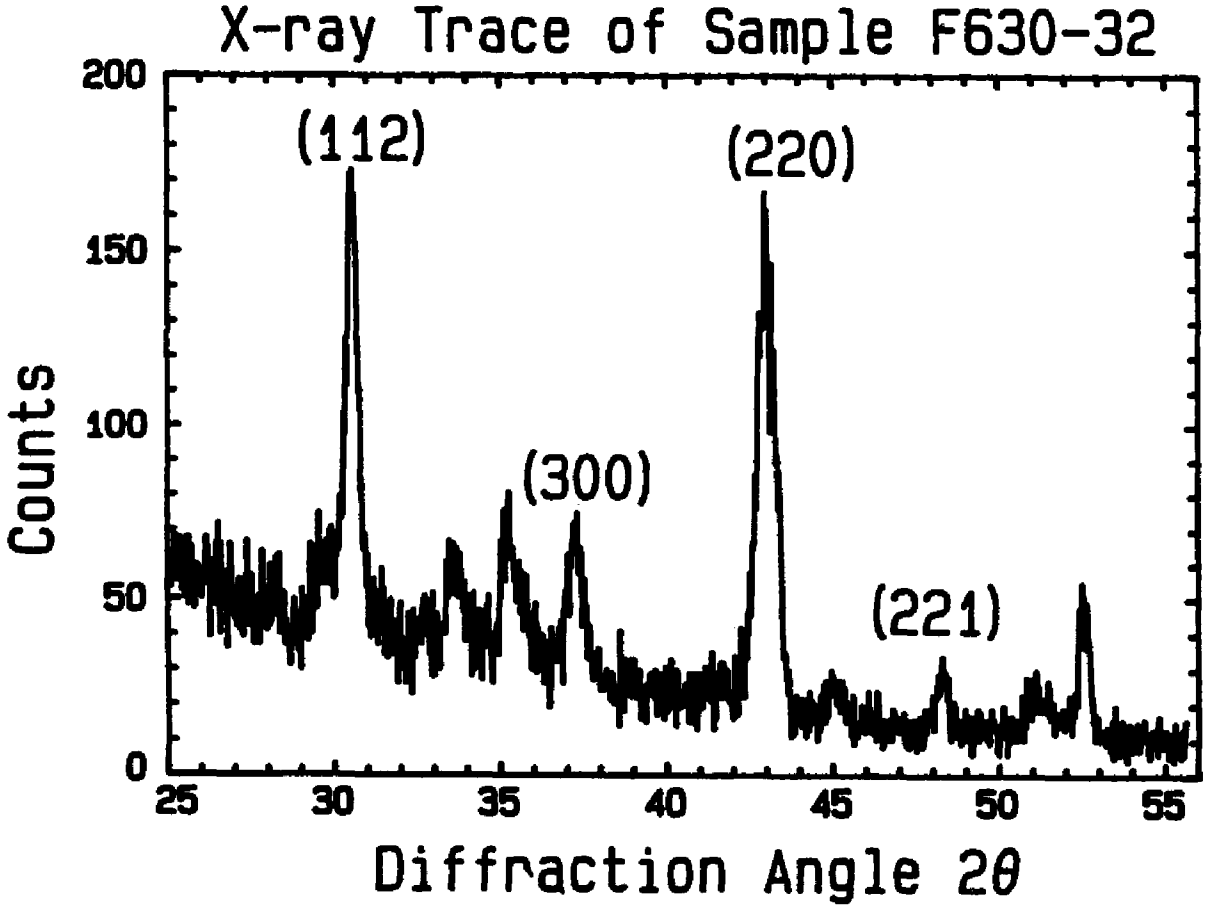
X-ray Trace of Sample F630-32
200
150
100
50
0
Counts
(112)
(220)
(300)
(221)
25
30
35
40
45
50
55
Diffraction Angle 2θ

Fig. 5.17

REFERENCES

1. D.E. Speliotis and J.J. Becker, J. Appl. Phys. 41, 1055 (1970).

2. M. Merches, S.G. Sankar, and W.E. Wallace, J. Appl. Phys. 49, 2055 (1978).

3. R.S. Perkins, S. Strassler, and A. Menth, AIP Conf. Proc. 29, 610 (1975).

4. M.V. Satyanarayana, W.E. Wallace, and R.S. Craige, J. Appl. Phys. 50, 2324 (1979).

5. F.J. Cadieu, T.D. Cheung, L. Wickramasekara, and R.G. Pirich, J. Appl. Phys. 53, 8338 (1982).

6. K.H.J. Buschow, J. Less Common Metals 25, 131 (1971).

7. F.J. Cadieu, T.D. Cheung, L. Wickramasekara, and S.H. Aly, J. Appl. Phys. 55, 2611 (1984).

8. F.J. Cadieu, T.D. Cheung, and L. Wickramasekara, J. Appl. Phys. 57, 4161 (1985).

9. L. Wickramasekara, T.D. Cheung, and F.J. Cadieu, J. Magn.& Magn. Mat. 54-57, 1679 (1986).

10. N. Kamprath, L. Wickramasekara, H. Hegde, N.C. Liu, J.K.D. Jayanetti, and F.J. Cadieu, J. Appl. Phys. 63, 3696 (1988).

11. N. Kamprath, N.C. Liu, H. Hegde, and F.J. Cadieu, J. Appl. Phys. 64, 5720 (1988).

12. N.C. Liu, N. Kamprath, L. Wickramasekara, and F.J. Cadieu, J. Appl. Phys. 63, 3589 (1988).

13. K.H.J. Buschow, Chapter 4, Ferromagnetic materials, Vol. 1, North Holland (1980).

14. W.B. Pearson, A Hand Book of Lattice Spacing and Structures of Metals and Alloys, Pergamon Press, Oxford (1958).

15. W.B. Pearson, The crystal Chemistry of Lattice Spacing and Physics of Metals and Alloys, Willey Interscience, N.Y. (1973).

16. K.H.J. Buschow and A.S. Vandergoot, J. Less. Common Metals 14, 323 (1968).

17. R.J. Gambino, P. Chaudhari, and J.J. Cuomo, AIP Proceedings, No. 12, part I Mag. and Mag. Mate.-1974, p. 578.

18. S. Mader, J. Vac. Sci. and Tech. 2, 35 (1965).

19. P. Chaudhari, J.J. Cuomo, and R.J. Gambino, Appl. Phys. Letters 22, 337 (1973).

20. P. Chaudhari, J.J. Cuomo, and R.J. Gambino, IBM J. of Res. & Dev. 11, 66 (1973).

21. H.J. Garrett and W.G.D. Frederick, AIP Conf. Proceedings, No. 10, Part I Mag. Materials-1972, p. 582.

22. M.A. Ruderman, C. Kittel, Phy Rev 96, 99 (1954), T. Kasuya, Prog. Theor. Phys. 16, 45 (1956), K. Yasida, Phy Rev 106, 893 (1957).

23. M.B. Stearn, Phy Rev 129, 1136 (1963) 147, 439 (1966), Phy Rev B4, 4069 and 4081 (1971); 8, 4383 (1973).

24. W.E. Wallace, Rare Earth Intermetallic, Academic Press, N.Y. (1973).

25. E.C. Stoner, Proc. Royal Soc. A, 165, 372 (1938).

26. J.J. Becker, J. Appl. Phys. 41, 1055 (1970).

27. E.A. Nesbitt, J.H. Wernick, and E. Corenzwit, J. Appl. Phys. 30, 365 (1974).

28. K.J. Stranat, G. Hoffer, W. Ostertag, and J.C. Olson, J. Appl. Phys. 37, 1252 (1966).

29. W.E. Wallace, Prog. Rare Earth Sci. Technol. 3 (1968).

30. K.H.J. Buschow, Rep. Prog. Phys. 40, 1179 (1977).

31. K.H.J. Buschow, in Ferromagnetic materials, editted by E.P. Wohlfarth, North-Holland, Amsterdam (1980), Vol. 1. p.197.

32. I.A. Campbell, J. Phys. F: etal Phys. 2L, 47 (1972).

33. J. Becker, J. Appl. Phys. 41, 1055 (1970).

34. A.S. Ermolenko, IEEE Trans. Magn. MAG-12, 992 (1976).

35. G. Hoffer and K. Strnat, IEEE Trans. Magn. MAG-2, 487 (1966).

36. E.C. Stoner and E.P. Wohlfarth, Proc. R. Soc. London, Ser. 240, 599 (1948).

37. W.F. Brown, Jr., Magnetosatatic principles in Ferromagnetism, North-Holland, Interscience, New York (1962).

38. J.D. Livingston, AIP Conf. Proc. 10, 643 (1973).

39. J.J. Becker, J. Appl. Phys. 39, 1270 (1968).

40. J.J. Becker, J. Appl. Phys. 42, 1537 (1971).

41. J.J. Becker, IEEE Trans. Magn. MAG-7, 644 (1971).

42. J.J. Becker, IEEE Trans. Magn. MAG-8, 520 (1972).

43. J.J. Becker, IEEE Trans. Magn. MAG-9, 161 (1973).

44. J.J. Becker, J. Appl. Phys. 41, 1055 (1970).

45. J.D. Livingston, AIP Conf. Proc. 10, 643 (1973).

46. R.A. Mc Currie and G.P. Carswell, Philos. Mag. 28, 611 (1973).

47. J.L. Vossen, Thin Film Processes Ch. 1, Academic Press (1978).

48. B. Chapman, Glow Discharge Processes, Wiley Interscience Publishers (1980).

49. J.S. Logan et al., J. Vac. Sci. Tech. Vol. 14, 1 (1977).

50. F.J. Cadieu and N. Chencinski, J. Low Temp. Phys. 28, 535 (1977).

51. F.J. Cadieu, L.F. Cooley, and D.H. Douglass, Jr., Rev. Sci. Instr. 42, 587 (1971).

52. Austin M. Garath, Phys. Rev. 36, 248 (1930).

53. Report Air Force Materials Laboratory Contract No. F33615-73-c-5012, Batelle Pacific Northwest (1974).

54. M. Gronau, H. Goeke, and S. Methfessel, Proc. 4th Int. Conf. on Rapidly Quenched Metals (Sendai 1981).

55. F.J. Cadieu, T.D. Cheung, L. Wickramasekara, N. Kamprath, H. Hegde, and N.C. Liu, J. Appl. Phys. 62, 3866 (1987).

56. J.D. Livingston and M.D. Mc Connel, J. Appl. Phys. 43, 4756 (1972).

57. T.D. Cheung, L. Wickramasekara, and F.J. Cadieu, J. Appl. Phys. 57, 3598 (1985).

58. L. Bergel and F.J. Cadieu, X-ray Spectrum. 9, 19 (1980).

59. B.D. Cullity, Elements of X-ray Diffraction, 2nd edition, Addison Wiley (1978).

60. D. Mcneely and H. Oesterreicher, J. Less Common Metals 44, 183 (1976).

61. T.D. Cheung, L. Wickramasekara, and F.J. Cadieu, J. Magn. & Magn. Mat. 54-57, 1641 (1986).

62. F.J. Cadieu, J. Vac. Sci. Technol. A6, 1668 (1988).

63. N. Kamprath, X.R. Qian, H. Hegde, and F.J. Cadieu, paper CD-1 to be published in J. Appl. Phys.

64. Y. Xingbo, T. Miyasaki, T. Izumi, H. Saito, Migaku Takahashi, and M. Takahahi, IEEE Trans. on Magnetic MAG-23, 3104 (1987).

65. K. Schniztke, L. Schultz, J. Wecker, and M. Katter, Apply. Phys. Lett. 56, 587 (1990).